PREFACE

Hong Duc University Journal of Science is the press agency established under the Operating Licence No.14/ MIC - OL, dated on January 1st, 2009 by the Ministry of Information and Communications and under the International Standard Serial Number - ISSN 1859 - 2759, issued by Center of Information Science and Technology - Science and Technology Ministry. Since 2014, the Journal of Science has been allowed to increase publishing periodically to 6 volumes a year with language published in both English and Vietnamese.

Hong Duc University Journal of Science in English is the press reflecting educational and training activities; publishing works, scientific studies of staff, faculties, students, scientists inside and outside the school; propagating and disseminating the policy guidelines and policies of the Party and the State on education and training; introducing, exchanging research results, the application of science and technology in the country and internationally.

Editorial Board would like to receive the enthusiastic collaboration of numerous faculty members, research scholars, scientists inside and outside the school to Hong Duc University Journal of Science so that we could bring readers the better results, useful information and scientific value.

BOARD OF EDITORS

HONG DUC UNIVERSITY
JOURNAL OF SCIENCE
E3 - Volume 8. 2017

TABLE OF CONTENTS

PRELIMINARY STUDY ON GeTe-SbTe AND Sm-B TOPOLOGICAL INSULATORS

Nguyen Le Thi, Nguyen Manh An, Le Viet Bau, Le Thi Giang, Nguyen Hoang Ha, Luu Duc Hoan, Do Bang

Abstract: *The process of developing the field of materials science is often driven by the discovery of new advanced materials. Especially, the material characteristics and uniformity of quantum mechanics are considered the most important. Of which, the topological insulator material with electrical insulation in the bulk but high conductivity on the surface has been extensively investigated as a new research direction in recent years due to its interesting properties that can be applied in spintronic applications. In this work, we investigate structural and electrical property of topological insulator materials of $[(GeTe)_2(Sb_2Te_3)_1]_n$ (GTST) multilayers which were fabricated on the Si wafers using a helicon-wave sputtering system and SmB_6 single crystals grown by the Aluminum-flux method;*

1. Introduction

The material class of topological insulators (TIs) has been discovered a few years ago and displays amazing properties. Inside its bulk exhibits a finite electronic bandgap (Figure 1a) and is, therefore, insulating. On the other hand, its surface states are gapless and metallic. These unusual properties are attributed to the intrinsic spin-orbit coupling which causes the quantum Hall effect and modifies the electronic structure significantly (Figure 1b).

Nguyen Manh An
President of Hong Duc University
Email: Nguyenmanhan@hdu.edu.vn (✉)

Nguyen Le Thi, Le Viet Bau, Le Thi Giang, Nguyen Hoang Ha
Faculty of Engineering and Technology, Hong Duc University
Email: Nguyenlethi@hdu.edu.vn (✉)
      Levietbau@hdu.edu.vn (✉)
      Legiang74@hdu.edu.vn (✉)
      Nguyenhoangha@hdu.edu.vn (✉)

Luu Duc Hoan
Hau Loc Continuing Education Center
Email: Hoanttgdtxhl@gmail.com (✉)

Do Bang
Institue of Materials Science
Vietnam Academy of Science and Technology
Email: Dobang.tti@gmail.com (✉)
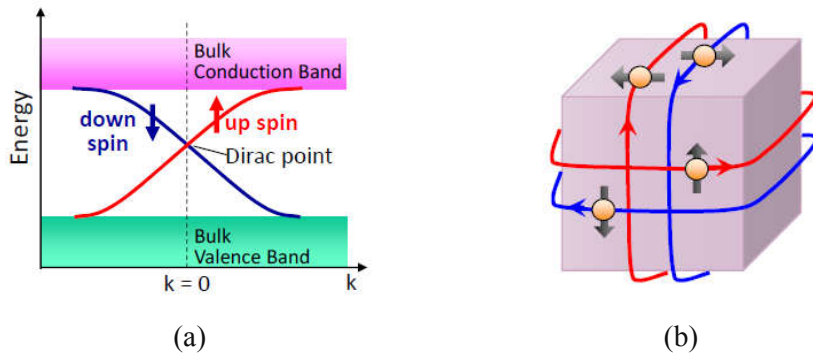
Figure 1. *(a) Schematic bulk and surface band structures; (b) Schematic real-space picture the 2D helica surface state of a TI*

In ordinary materials, backscattering, in which electrons take collisions with crystal defects, effectively degrades the current flow and increases the resistance. However, on the surface of TIs, such backscattering processes are completely suppressed, so charge transport is in dissipation less or low dissipation states. In 2008, the first TI material as experimentally identified was $Bi_{1-x}Sb_x$ with the Sb concentration range of 0.09 to 0.23 [1]. However, it was found out that this material is not very suitable for detailed studies of the topological surface state due to its complicated surface-state-structure [2,3]. Then several theoretical band calculations to elucidate the parity eigenvalues were done [4,5] and came up with a prediction that Bi_2Se_3, Bi_2Te_3, and Sb_2Te_3 would have a simple surface band structure (Figure 2).
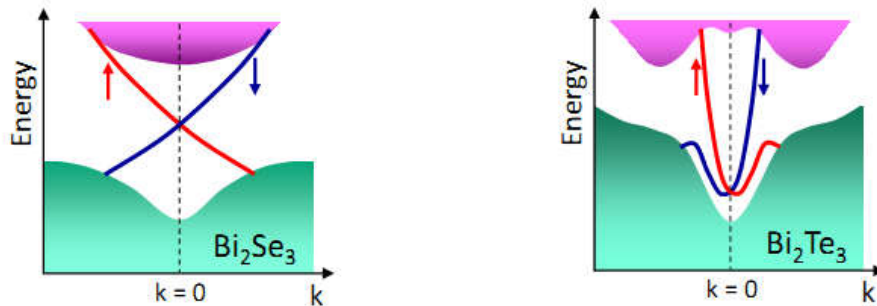
Figure 2. *Schematic bulk and surface structures of (a) Bi_2Se_3 and (b) Bi_2Te_3*

These materials were also experimentally confirmed and reported in references [6-10]. Furthermore, the bulk gap of Bi_2Se_3 is relatively large (0.3 eV), and thus one can see the technological relevance that topological properties can be exploited at room temperature. However, its chemistry is always degenerately doped due to naturally occurring crystalline defects, which cause its transport properties to be dominated by bulk carriers. In this respect, TI material having tetradymite structure is promised and it was first reported for Bi_2Te_2Se and Sb_2Te_2Se [10-12]. An important theme in the research of TIs is to reduce unintentionally-doped bulk carrier that hinders observations of surface transport properties by using suitably

doped elements [13-15]. In fact, another useful approach to reducing bulk carriers is to reduce the size of samples by making thin ribbons, films and nanowires [16-18]. Another candidate topological zero-gap semimetals are Heusler or half-Heusler compounds (LnAuPb, LnPtBi…). Several experimental evidences of this have been reported so far [19-21]. Moreover, the rare earth containing crystal SmB_6 is also predicted to be a TI due to strongly correlated heavy fermion material to exhibit topological surface states [22]. Recently, our collaborating research group in Japan has succeeded in fabricating high quality crystalline $[(GeTe)_2(Sb_2Te_3)_1]_n$ (GTST) topological superlattices, which lead to as much as a 95% reduction in the switching energy of electrical non-volatile phase-change random-access memory [23]. In this study, we investigated the effect of annealing process on the crystalline structures and electrical properties of the GTST multilayers, and influence of fabrication conditions on structure of SmB_6 bulk samples prepared by the Aluminum-flux method.

2. Experiment

Most of the confirmed TI materials are chalcogenides. Since the chalcogen atoms are volatile, the syntheses of the TI materials can be done by using Bridgman method for bulk samples, molecular beam epitaxy (MBE) or sputtering system for thin films and chemical vapor transport for ribbon and nanowires samples. To avoid unexpected contaminations, the grown crystalline should be done in the vacuum or in Ar/I_2 gas.

The $[(GeTe)_2(Sb_2Te_3)_1]_n$ topological superlattices were fabricated at different substrate temperatures of 150 to 210 ºC on Si wafers using a helicon-wave sputtering system that has GeTe and Sb_2Te_3 composite targets (2-inch) and automated control shutters at pressures less than 0.5 Pa Ar. Thicknesses of each GeTe and Sb_2Te_3 sublayers were 0.85 nm and 1.0 nm, respectively. A 3 nm-thick Sb_2Te_3 layer was firstly deposited to ensure the strong crystalline orientation. Finally, a 20 nm-thick $ZnS-SiO_2$ layer was deposited as a capping layer to protect the GTST multilayers from oxidation [24]. We then investigated the effect of annealing process on the crystalline structures and electrical properties of the GTST multilayers by using X-ray diffraction (XRD) and resistivity measurements, respectively.

By reviewing several fabrication methods of topological insulator materials, we realized that Bridgman and Aluminum-flux methods can be realized on the research facilities in Vietnam. In addition, most components of TI materials contain toxic elements such as Pb, Bi, Sb, and Se. Therefore, the selection of investigational compounds would be selected to limit the effect on human and environment. In this work, SmB_6 compound was chosen to synthesize by the aluminum-flux method with the starting materials of samarium ingot, boron powder and aluminum granules. Sm, B, and Al were weighted in an atomic ratio of 1:4:200. The mixture was placed in an alumina crucible and heated to 1150ºC in the vacuum. During the reaction, the crucible was covered with an alumina lid to reduce Al evaporation. After maintaining at 1150ºC for 2 hours, the furnace was slowly cooled to 25ºC in 10 hours. The aluminum - flux was dissolved by a concentrated NaOH solution in a fume hood, and shiny single crystals of SmB_6 of millimeter-size were picked out.

Scanning/Transmission Electron Microscopy (SEM/TEM) and X-ray diffraction (XRD) measurements were used to study the structure of the SmB_6 samples.

3. Results and discussion

The XRD patterns of the as-deposited GTST multilayers are shown in Figure 3a. For the higher depositing temperature of 210ºC multilayer has a better crystalline structure. Especially, the intensity of the (001) crystalline direction gradually increases when the depositing temperature increases from 150 to 210ºC. These results can be explained by the self-organized van der Waals epitaxy model due to the reactive selectivity of the surface [25]. It has been reported that Te forms a compound with Si, while Sb does not. On the other hand, both the Sb and Te react with O which will form a mixed position of Sb and Te on the first Sb_2Te_3 sublayer. Therefore, it is expected that the surface oxide would be effectively removed at higher temperatures, resulting in a reactive selectivity and the surface would be covered with a monolayer of Tb preferentially. Then the second monolayer would be Sb as the layer by layer structure of Te and Sb atomics.

The 150ºC as-deposited multilayer was annealed at 210ºC for 1 hour and its XRD patterns was measured again as shown in Figure 3b. It is clearly seen that the crystalline structure was significantly improved after the annealing process due to reconstruction at higher temperatures.
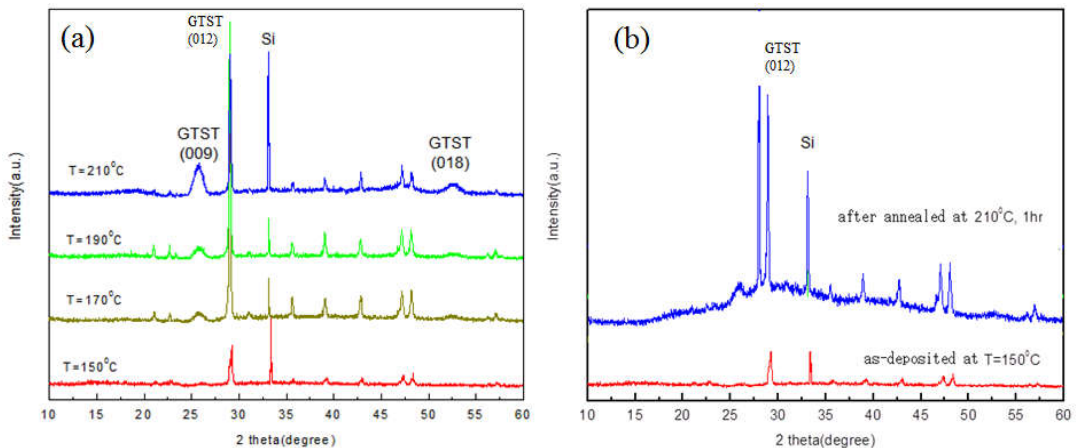
Figure 3. X-ray diffraction patterns of (a) 150, 170, 190, and 210 ºC as-deposited GTST multilayers and (b) the 150ºC as-deposited multilayer was annealed at 210ºC for 1 hour

The magnetic field dependences of the resistivity measured at room temperature for the 150, 210ºC as-deposited and 210ºC annealed GTST multilayers are shown in figure 4. For the 150ºC as-deposited sample, its resistivity is one order higher than those of the other ones. This high resistivity is comparable with that of the GeSbTe alloy. It means that the main part of the 150ºC as-deposited sample is not in well crystalline structures as shown in the XRD patterns (figure 3) but in alloy compounds of GeTe and SbTe which have semiconductor behaviors at

room temperature. On the other hand, the resistivity of the 210ºC as-deposited and 210ºC annealed GTST multilayers is as low as that of a good GeTe-SbTe superlatice. It suggested that the annealing process at high temperatures can improve the crystalline structure as well as the electrical property of the low temperature deposited GTST films due to the reconstruction of atoms.
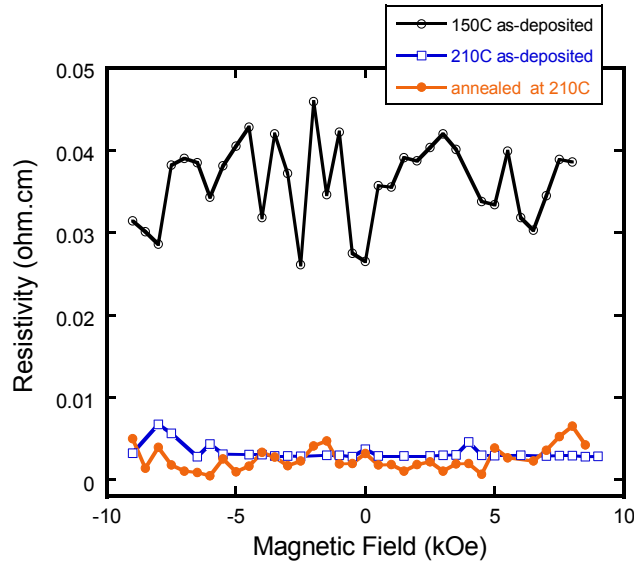
Figure 4. Magnetic field dependences of resistivity for 150ºC as-deposited (opened circles) and 210ºC as-deposited (opened squares) GTST multilayers, and the 150ºC as-deposited multilayer was annealed at 210ºC for 1 hour (solid circles)
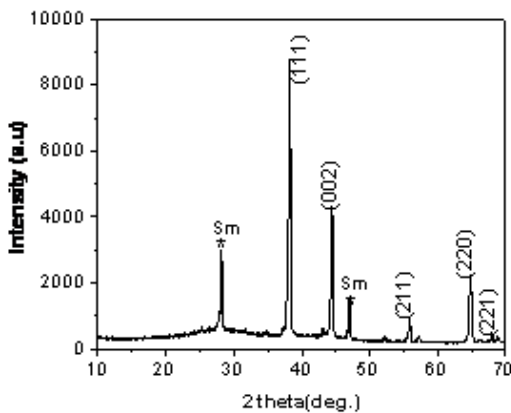
Figure 5. XRD pattern of SmB_6 bulk sample synthesized at 1150^0C
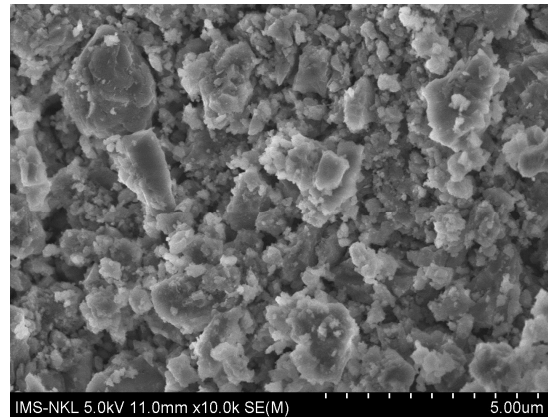
Figure 6. SEM image of SmB6 bulk sample synthesized at 1150^0C

As shown in [22], the single crystal structure of SmB_6 is cubic lattice with constant a = 4.1353Å. Figure 5 shows XRD pattern of SmB_6 prepared at 1150ºC using Sm, B, and Al as raw material. Aluminum here plays the role of reducing the melting temperature of elements in the component. It can be seen that all the diffraction peaks are not really the

SmB_6 single crystal structure. However, its XRD patterns are well indexed and assigned to the parallel crystal planes of (221), (220), (211), (002), (111) [26]. The impurity phases are identified to be Sm element.

The SEM image is shown in Figure 6. It can be seen that the SmB_6 bulk sample prepared at 1150°C is mainly composed of a great deal of aggregated particles without any regular shapes, there are some large grains with non-cubic morphology mixing together. In the next steps, we will continue to synthesize samples at different temperatures to obtain the better SmB_6 single crystals.

4. Conclusion

We investigated the effect of annealing process on the crystalline structures and electrical properties of the GTST multilayers. It is found that the annealing process at high temperatures can improve the crystalline structure as well as the electrical property of the low temperature deposited GTST films due to the reconstruction of atoms. On the other hand, we also fabricated SmB_6 single crystals by the Aluminum-flux method and investigated their structure. The results showed that the SmB_6 bulk sample prepared at 1150°C is mainly composed of a great deal of aggregated particles without regular shapes. There are some large grains with non-cubic morphology mixing together.

References

[1] D. Hsieh, D. Qian, L. Wray, Y. Xia, Y. S. Hor, R. J. Cava, and M. Z. Hasan (2008), *A topological Dirac insulator in a quantum spin Hall phase*, Nature: vol. 452, pp. 970-974,

[2] P. Roushan, J. Seo, C. V. Parker, Y. S. Hor, D. Hsieh, D. Qian, A. Richardella, M. Z. Hasan, R. J. Cava, and Yazdani (2009), *Topological surface states protected from backscattering by chiral spin texture*, Nature, vol. 460, pp. 1106-1109.

[3] A. Nishide, A. A. Taskin, Y. Takeichi, T. Okuda, A. Kakizaki, T. Hirahara, K. Nakatsuji, F. Komori, Y. Ando, amd I. Matsuda (2010), *Direct mapping of the spin-filtered surface bands of a three-dimensional quantum spin Hall insulator,* Phys. Rev. B, vol. 81, 041309(R).

[4]   H. Zhang, C.-X. Liu, X.-L. Qi, X. Dai, Z. Fang, and S.-C. Zhang (2009), *Topological insulators in Bi,* Nature Phys. vol. 5, pp. 438-442.

[5]   C.-X. Liu, X.-L. Qi, H. Zhang, X. Dai, Z. Fang, and S.-C. Zhang (2010), *Model Hamitonian for topological insulators,* Phys. Rev. B, vol. 82, 045122, 2010.

[6]   Y. Xia, D. Qian, D. Hsieh, L. Wray, A. Pal, H. Lin, A. Bansil, D. Grauer, Y. S. Hor, R. J. Cava, and M. Z. Hasan (2009), *Observation of a large-gap topological-insulator class with a single Dirac cone on the surface*, Nature Phys., vol. 5, pp. 398-402.

[7]   Y. L. Chen, J. G. Analytis, J.-H. Chu, Z. K. Liu, S.-K. Mo, X. L. Qi, H. J. Zhang, D. H. Lu, X. Dai, Z. Fang, S. C. Zhang, I. R. Fisher, Z. Hussain, and Z.-X. Shen (2009), *Experimetal realization of a three-dimentional topological insulator, Bi_2Te_3*, Science, vol. 325, pp. 178-181.

[8]   D. Hsieh, Y. Xia, D. Qian, L. Wray, F. Meier, J. H. Dil, J. Osterwalder, L. Patthey, A. V. Fedorov, H. Lin, A. Bansil, D. Grauer, Y. S. Hor, R. J. Cava, and M. Z. Hasan (2009), *Observation of time-reversal-protected single-Dirac-cone topological-insulator states in Bi_2Te_3 and Sb_2Te_3*, Phys. Rev. Lett., vol. 103, 146-401.

[9]   Y. Jiang, Y. Wang, M. Chen, Z. Li, C. Song, K. He, L. Wang, X. Chen, X. Ma, and Q. K. Xue (2012), *Landau quantization and the thickness limit of topological insulator thin films of Sb_2Te_3*, Phys. Rev. Lett., vol. 108, 016401.

[10]   C. H. Li et al. (2014), *Electrical detection of charge-current-induced spin polarization due to spin-momentum locking in Bi_2Se_3*, Nature Nanotech., vol. 9, pp. 218-224.

[11]   Z. Ren, A. A. Taskin, S. Sasaki, K. Segawa, and Y. Ando (2010), *Large bulk resistivity and surface quantum osillations in the topological insulator Bi_2Te_2Se*, Phys. Rev. B, vol. 82, 241306(R).

[12]   J. Xiong, A. C. Petersen, D. Qu, Y. S. Hor, R. J. Cava, and N. P. Ong (2012), *Quantum oscillations in a topological insulator Bi_2Te_2Se with large bulk resistivity*, Physica E, vol. 44, pp. 917-920.

[13]   Z. Ren, A. A. Taskin, S. Sasaki, K. Segawa, and Y. Ando (2011), *Observations of two-dimensional quantum oscillation and ambipolar transport in the topological insulator Bi2Se3 achieved by Cd doping*, Phys. Rev. B, vol. 84, 075316.

[14]   H. Ji, J. M. Allred, M. K. Fuccillo, M. E. Charles, M. Neupane, L. A. Wray, M. Z. Hasan, and R. J. Cava (2012), *A topological insulator in the tetradymite family*, Phys. Rev. B, vol. 85, 201103.

[15]   P. Gehring, H.M.Benia, Y.Weng, R. Dinnebier, C. R. Ast, M.Burghard, and K. Kern (2013), *A natural topological insulator*, Nano Lett*.,* vol. 13, 1179.

[16]   D. Kong, J. C. Randel, H. Peng, J. J. Cha, S. Meister, K. Lai, Y. Chen, Z.-X. Shen, H. C. Manoharan, and Y. Cui (2010), *Topological insulator nanowires and nanoribbons*, Nano Lett., vol. 10, pp. 329-333.

[17]   D. Kong, Y. Chen, J. J. Cha, Q. Zhang, J. G. Analytis, K. Lai, Z. Liu, S. S. Hong, K. J. Koski, S.-K. Mo, Z. Hussain, I. R. Fisher, Z.-X. Shen, and Y. Cui (2011), *Ambipolar field effect in topological insulator nanoplates of $(Bi_xSb_{1-x})_2Te_3$*, Nature Nanotechnol., vol. 6, pp. 705-709.

[18] S. S. Hong, J. J. Cha, D. Kong, and Y. Cui (2012), *Ultra-low carrier concentration and surface-dominant transport in antimony-doped Bi_2Se_3 topological insulator nanoribbons*, Nature Commun., vol. 3, pp. 757-763.

[19] S. Chadov, X.-L. Qi, J.K¨ubler, G. H. Fecher, C. Felser, and S.-C. Zhang (2010), *Tunable multifunctional topological insulators in ternary Heusler compounds,* Nature Mater, vol. 9, pp. 541-545.

[20] H. Lin, L. A. Wray, Y. Xia, S. Xu, S. Jia, R. J. Cava, A. Bansil, and M. Z. Hasan (2010), *Half-Heusler ternary compounds as new multifunctional experimental platforms for topological quantum phenomena,* Nature Mater., vol. 9, 546-549.

[21] D. Xiao, Y. Yao, W. Feng, J. Wen, W. Zhu, X.-Q. Chen, G. M. Stocks, and Z. Zhang (2010), *Half-Heusler compounds as a new class of three dimensional topological insulators*, Phys. Rev. Lett., vol. 105, 096404.

[22] M. Ciomaga Hatnean, M. R. Lees, D. McK. Paul & G. Balakrishnan (2013), *Large, high quality single-crystals of the new Topological Kondo Insulator, SmB_6*, Nat. Sci. Rep., vol.3, 3071, 2013.

[23] Tominaga J et al. (2015), *Giant multiferroic effects in topological $GeTe$-Sb_2Te_3 superlattices*, Sci. Technol. Adv. Master*, vol. 16, 014402.

[24] D. Bang et al. (2014), *Mirror-symmetric Magneto-optical Kerr Rotation using Visible Light in [(GeTe)2(Sb2Te3)1]n Topological Superlattices*, Nat. Sci. Rep., vol. 4, 5727; DOI:10.1038/srep05727.

[25] Y. Saito et al. (2015), *Self-organized van der Waals epitaxy of layered chalcogenide structures*, Phys. Status Solidi B,vol. 252, 2151-2158.

[26] Lihong Bao et al. (2015), *SmB_6 nanoparticals: Synthesis, valence states, and magnetic properties*, Journal of Alloys and Compounds, vol. 651, pp. 19-23.

ARTIFACT CHARACTERIZATION OF JPEG DOCUMENTS

Pham The Anh, Mathieu Delalandre

Abstract: *This paper addresses the problem of blocking artifact characterization that is introduced when using low bit-rate JPEG compression. Specifically, a novel blocking metric is presented to characterize the distortion of JPEG blocking artifact when applied to document content. Furthermore, the proposed metric is directly processed in the transform domain without the need of fully decompressing the images, making its computation very time-efficient. Correlation of the proposed metric to OCR performance is validated through our experiments.*

1. Introduction

The JPEG standard has been widely used for multi-media data compression nowadays. In its essence, the JPEG codec divides input image into non-overlapping 8×8 blocks, each of which is then individually compressed by a pipeline of following steps: image de-correlation using Discrete Cosine Transform (DCT), quantization and entropy coding. The DCT coefficients $F(m,n)$ of an image block $f(x,y)$ are defined as follows:

$$F(m,n) = \frac{e(m)e(n)}{4} \sum_{x=0}^{7} \sum_{y=0}^{7} f(x,y) C_{16}^{(2x+1)m} C_{16}^{(2y+1)n} \qquad (1)$$

where $C_y^x = \cos(\frac{x\pi}{y})$, $e(t) = \begin{cases} \frac{1}{\sqrt{2}} & \text{if } t = 0 \\ 1 & \text{otherwise} \end{cases}$

The inverse DCT transforms (IDCT) is defined to accordingly recover the original image by:

$$f(x,y) = \frac{1}{4} \sum_{m=0}^{7} \sum_{n=0}^{7} e(m)e(n) F(m,n) C_{16}^{(2x+1)m} C_{16}^{(2y+1)n} \qquad (2)$$

At low bit-rate coding, JPEG encoded images are subject to heavy distortion of blocking artifact due to the independent coding of each block. Characterization of blocking

Pham The Anh

Faculty of Information and Communication Technologies, Hong Duc University

Email: Phamtheanh@hdu.edu.vn (✉)

Mathieu Delalandre

Computer Science Lab, Francois Rabelais University, Tours city, France

Email: Mathieu.delalandre@univ-tour.fr (✉)

behavior is thus a critical task for various problems including blocking artifact reduction, OCR prediction, adaptive compression, image quality assessment, etc.

Basically, blocking artifact refers to the discontinuities of pixel values along the block boundaries. At low bit-rate coding, the transformed coefficients are heavily quantized resulting in the loss of information of intra-block pixels and of inter-block transitions. Consequently, the decompressed image is annoyed by the discontinuities over the blocks. In the literature, various blocking metrics have been proposed to characterize the blocking artifact for natural images [1]-[7]. However, little attention has been investigated to characterize the blocking distortion for document content.

In this work, we aim at measuring the blocking distortion when using JPEG coding applied to document content. Specifically, the main contribution of this work is three-fold. First, a novel blocking artifact measure is presented to characterize the blocking distortion at low bit-rate compression. Second, we propose computing this measure directly in the DCT domain without decompressing the images. This feature is opposed to many approaches in the literature in which a full decompression stage is obligated [1], [3], [5]-[7]. As such, the characterization becomes time-efficient and could be exploited in a context of adaptive compression or artifact post-processing optimization. At last, we show by experimental results the relevance of the proposed blocking measure to OCR performance.

The rest of this paper is structured into five sections. Section II reviews the key methods for blocking artifact characterization in the literature. Section III presents a technique to efficiently compute block boundary variation in the transform domain. The proposed blocking measure is described in Section IV. Experimental results are provided in Section V and we conclude the paper in Section VI.

2. Review of blocking artifact characterization

A number of blocking metrics have been proposed to characterize the image degradation caused by low bit-rate compression. Most of these metrics were conducted in the image spatial domain [1], [3], [5]-[8], while several attempts proposed computing blocking measure directly in DCT domain [2], [4], [9], [10].

In [1], a blocking measure was estimated by counting the number of zero-valued DCT coefficients. To differentiate the naturally uniform regions from the uniform areas caused by blocking artifact, the number of zero-valued coefficients is weighted using a quality relevance map which is computed based on the slope of the Fourier magnitude spectrum of the blurred image. A small value of the slope indicates the presence of naturally uniform regions. The authors in [3] detect blocking candidates by measuring the abrupt changes at the block boundaries. Doing so, true edge blocks are also included in the candidate list but they are then filtered out based on the observation that the intensity values are often mutually different on the edge boundary. Blocking strength is finally estimated from the remaining candidates by averaging the sums of horizontal masked cross-block-boundary difference (SHMCD).

While all the aforementioned methods are dedicated to measure blocking artifact in the spatial domain, several attempts have been investigated to detect blockiness disortion directly in the DCT transform [2], [4], [9], [10]. Blockiness processing in the DCT domain brings great benefit of efficient computation as it avoids applying IDCT transform which is too costly. One of the earliest blocking metrics was proposed in [9] so-called mean squared difference of slope (MSDS). In its essence, MSDS is computed as the mean square difference between the gradient computed at a horizontal/vertical boundary of a block and the average gradient computed from the adjacent slopes along that boundary.

It is worth mentioning that all these blocking metrics are devoted to natural images. There has been little discussion about the behavior of blocking artifact for document images. To our best of knowledge, only the work in [11] provided a preliminary evaluation of JPEG, JPEG 2000 and MRC coding methods using the PSNR metric using a few document samples. In the following sections, we attempt to bring a novel and efficient metric for measuring blocking distortion dedicated to document content.

3. Computing block boundary variation in DCT domain

Given an image f having the size of $M \times N$, let B_x and B_y be the number of blocks in the vertical and horizontal directions (i.e., $B_x = \left\lceil \dfrac{M}{8} \right\rceil$ and $B_y = \left\lceil \dfrac{N}{8} \right\rceil$). For the sake of presentation, we denote a block located at k^{th} row and l^{th} column by (k,l) with $k = 0,1,...,B_x - 1$ and $l = 0,1,...,B_y - 1$. We also denote $F^{k,l}(m,n)$ as the DCT coefficients of the block (k,l) with $m,n \in \{0,1,...,7\}$. Since blocking artifact causes the abrupt changes in pixel intensity at the block boundaries, it makes sense to analyze the variation along the boundaries of the blocks. Specifically, we suggest computing block boundary variation (BBV) for each block by dividing the block into 16 subregions (Figure 1).

Figure 1. *Computing block boundary variation at 2×2 super-pixel level*

15

Each subregion is regarded as a super-pixel corresponding to a local window having the size of 2×2. Each super-pixel (u, v) is assigned with an average intensity value $S_{uv}^{k,l}(u, v \in \{0, 1, 2, 3\})$ computed by [12]:

$$S_{uv}^{k,l} = \frac{1}{4}\sum_{i=0}^{1}\sum_{j=0}^{1} f^{k,l}(2u+i, 2v+j) \qquad (3)$$

Where $f^{k,l}(x, y)$ is the intensity value of the pixel (x, y) in the block (k, l) of the image f.

For each block (k, l), we define $BBV_H(f^{k,l})$ and $BBV_v(f^{k,l})$ as horizontal and vertical block boundary variation, respectively. These measures are computed as follows:

$$BBV_H(f^{k,l}) = \sum_{i=0}^{3}\left|S_{i0}^{k,l+1} - S_{i3}^{k,l}\right|$$

$$BBV_v(f^{k,l}) = \sum_{i=0}^{3}\left|S_{0i}^{k+1} - S_{3i}^{k,l}\right|$$

In what follows, we investigate a means for fast computing BBV in the DCT domain. The following materials are targeted to computing $BBV_H(f^{k,l})$ although the same process can be applied to compute $BBV_v(f^{k,l})$.

Firstly, substituting (2) into (3) and rearranging the terms in a similar manner as given in [12], we obtain the following expression:

$$S_{uv}^{k,l} = \sum_{m=0}^{7}\sum_{n=0}^{7} F^{k,l}(m,n)w_{uv}(m,n) \qquad (4)$$

where $w_{uv}(m,n) = \frac{1}{4}e(m)e(n)C_{16}^{m}C_{8}^{(2u+1)m}C_{16}^{n}C_{8}^{(2v+1)n}$.

For simplification purpose, we define D_i with $i \in \{0, 1, 2, 3\}$ as the sub-terms of $BBV_H(f^{k,l})$: $D_i = S_{i0}^{k,l+1} - S_{i3}^{k,l}$. Accordingly, D_0 is represented in the form of:

$$D_0 = S_{00}^{k,l+1} - S_{03}^{k,l}$$

$$= \sum_{m=0}^{7}\sum_{n=0}^{7}(F^{k,l+1}(m,n)w_{00}(m,n) - F^{k,l}(m,n)w_{03}(m,n))$$

$$= \sum_{m=0}^{7}\sum_{n=0}^{7}\frac{e(m)e(n)C_{16}^{n}C_{16}^{m}C_{8}^{m}}{4}(F^{k,l+1}(m,n)C_{8}^{n} - F^{k,l}(m,n)C_{8}^{7n})$$

Note that $C_{8}^{7n} = (-1)^{n}C_{8}^{n}$, we obtain:

$$D_0 = \frac{1}{4}\sum_{m=0}^{7}\sum_{n=0}^{7}e(m)e(n)C_{16}^{n}C_{16}^{m}C_{8}^{m}C_{8}^{n}R(m,n)$$

where $R(m,n) = F^{k,l+1}(m,n) - (-1)^{n}F^{k,l}(m,n)$. In the same manner, the remaining D_i are computed by $1 \le i \le 3$: $D_i = \frac{1}{4}\sum_{m=0}^{7}\sum_{n=0}^{7}e(m)e(n)C_{16}^{n}C_{16}^{m}C_{8}^{(2i+1)m}C_{8}^{n}R(m,n)$

Let $z_k(m,n) = \dfrac{1}{4} e(m)e(n)C_{16}^n C_{16}^m C_8^{km} C_8^n$ with $k \in \{1,3,5,7\}$, due to the fact that $C_8^{5n} = (-1)^n C_8^{3n}$, the following properties are derived for $z_k(m,n)$:

- $\dfrac{z_7(m,n)}{z_1(m,n)} = \dfrac{z_5(m,n)}{z_3(m,n)} = (-1)^m$

- $k_m = \dfrac{z_3(m,n)}{z_1(m,n)} = \dfrac{C_8^{3m}}{C_8^m}$ (see Table 1)

- $z_k(m,n) = 0$ for either $m = 4$ or $n = 4$

As each D_i is composed of symmetric terms, we can unroll D_i by defining G_3^{odd} and G_3^{even} with $j \in \{0,1\}$ as follows: $G_j^{odd} = \displaystyle\sum_{m=1,3,5,7} \sum_{n=0}^{7} z_{2j+1}(m,n)R(m,n)$.

$$G_j^{even} = \sum_{m=0,2,6} \sum_{n=0}^{7} z_{2j+1}(m,n)R(m,n)$$

As a result, each D_i is represented in the form of:

$$D_0 = G_0^{even} + G_0^{odd}$$
$$D_1 = G_1^{even} + G_1^{odd}$$
$$D_2 = G_1^{even} - G_1^{odd}$$
$$D_3 = G_0^{even} - G_0^{odd}$$

Table 1. *Precomputetion of* k_m

m	0	1	2	3	5	6	7
k_m	1	$\dfrac{C_8^3}{C_8^1}$	-1	$-\dfrac{C_8^1}{C_8^3}$	$\dfrac{C_8^1}{C_8^3}$	-1	$-\dfrac{C_8^3}{C_8^1}$

If the property of k_m in Table 1 is taken into account, we can further simplify the computation of G_1^{even} and G_1^{odd} by:

$$G_1^{even} = \sum_{n=0}^{7} (z_1(0,n)R(0,n) - z_1(2,n)R(2,n) - z_1(6,n)R(6,n))$$

$$G_1^{odd} = \sum_{n=0}^{7} (k_1 z_1(1,n)R(1,n) + k_3 z_1(3,n)R(3,n) - k_3 z_1(5,n)R(5,n) - k_1 z_1(7,n)R(7,n))$$

$$= k_1 \sum_{n=0}^{7} z_1(1,n)R(1,n) - k_1 \sum_{n=0}^{7} z_1(7,n)R(7,n) + k_3 \sum_{n=0}^{7} z_1(3,n)R(3,n) - k_3 \sum_{n=0}^{7} z_1(5,n)R(5,n)$$

To compute D_i efficiently, we define H_t with $t \in \{0,1,2,3,5,6,7\}$ by:

$$H_t = \sum_{n \in \{0,1,2,3,5,6,7\}} z_1(t,n)R(t,n)$$

With these results in mind, D_i can be finally computed by:

$$D_0 = H_0 + H_2 + H_6 + (H_1 + H_3 + H_5 + H_7)$$
$$D_3 = H_0 + H_2 + H_6 - (H_1 + H_3 + H_5 + H_7)$$
$$D_1 = H_0 - (H_2 + H_6) + k_1(H_1 - H_7) + k_3(H_3 - H_5)$$
$$D_2 = H_0 - (H_2 + H_6) - (k_1(H_1 - H_7) + k_3(H_3 - H_5))$$

In short, computation of $BBV_H(f^{k,l})$ requires 51M + 106A. This complexity is much more efficient than applying full IDCT (i.e., 4096M + 4096A) even when comparing with fast IDCT.

4. Document blocking artifact measure (DBAM)

In general, blocking artifact causes the abrupt changes at the boundaries of the blocks. Hence, measuring the changes along the block boundaries is a good indication of blocking artifact. However, since document content is mostly composed of two-intensity values, the transition between foreground (FG) and background (BG) would cause the abrupt changes as well. This occurs when parts of the characters' strokes are located at the boundaries of the blocks (see the characters 'P', 'H', and 'L' for example). To correctly estimate the blocking artifact measure, it is desired to differentiate the abrupt changes caused by the natural FG/BG transition from the changes introduced by blocking artifact. We propose handling this matter based on the following two observations.

First, since the size of each character is likely to be much higher than the conventional block size (i.e., 8×8), each character can be considered as a region composing of several blocks. Therefore, it is occasionally the case that all four boundaries of one block contain the strokes of the characters. In contrary, at low bit-rate coding, the abrupt changes caused by blocking artifact are likely to occur along all the block boundaries since each block is independently encoded.

<center>(a)   (b)</center>
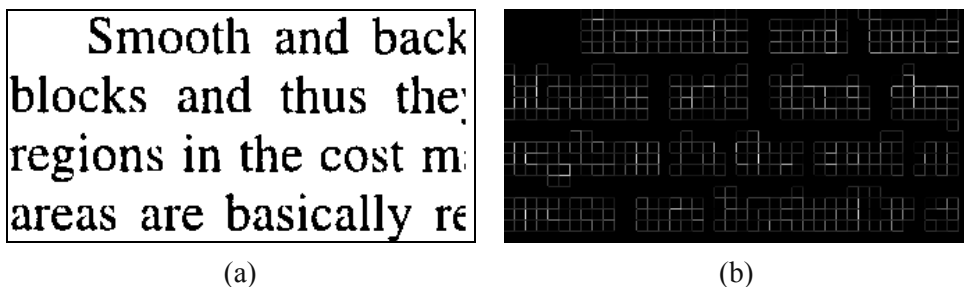
Figure 2. (a) Original image; (b) BBV strength map (higher values, brighter pixels) with JPEG quality factor = 2

Figure 2 plots the BBV strength map (JPEG quality = 2) where one can see the boundary discontinuities virtually occur at all the boundaries of foreground blocks. For original or high bit-rate coding image, the boundary discontinuities partially occur at the block

boundaries with a much lower frequency. Consequently, one can exploit the BBV distribution at four boundaries of each block to eliminate the contribution caused by the FG/BG transition at that block. This can be simply done by weighting each block by the ratio of the smallest value to the biggest one among four BBV measures of the block.

Second, it was found that the BBV peaks are likely to occur at the areas corresponding to the natural FG/BG transitions. This observation suggests that using a high-band filter seems to be a good solution to eliminate the BBV peaks at these regions. Such a technique, however, requires a good threshold selection step which is not easily handled. Alternatively, we propose using a non-linear filter to address this problem. The rationale is again based on the fact that the BBV map of a low bit-rate coding image is distributed more uniformly than that of a high bit-rate coding image. Therefore, a non-linear filtering technique such as median filtering would help eliminate the outliers corresponding to the BBV peaks caused by the FG/BG transitions. Specifically, we construct a circular masking filter $M_{k,l}(r)$ centered at the block (k,l) with the radius r as shown in Figure 3.
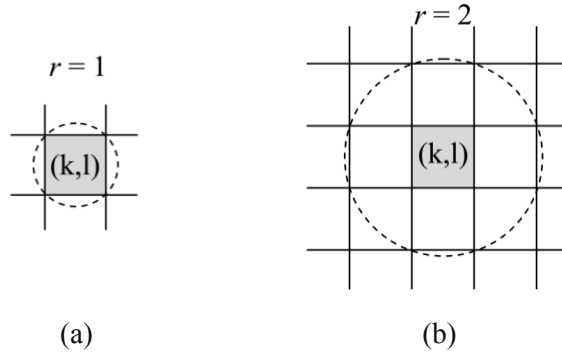
Figure 3. *Non-linear mask filtering: (a) radius = 1, (b) radius = 2*

Accordingly, $M_{k,l}(1)$ and $M_{k,l}(2)$ contain 4 and 12 BBV elements, respectively. Next, we define a blockiness measure, $BM_{k,l}$, for the block (k,l) by the weighted median value among all the BBV values positioning inside the mask $M_{k,l}(r)$. In our experiments, we set the parameter $r = 2$.

For completeness, the procedure to compute the blockiness measure is sketched out as follows:

• Compute BBV_V and BBV_H for all the boundaries of the blocks.

• Compute a weight $\alpha_{k,l}$ for each block (k,l) by:

$$\alpha_{k,l} = \frac{\min_{i \in M_{k,l}(1)} \{BBV_i\}}{\max_{i \in M_{k,l}(1)} \{BBV_i\}}$$

• Compute the blockiness measure $BM_{k,l}$ for each block (k,l) by:

$$BM_{k,l} = \alpha_{k,l} MED_{i \in M_{k,l}(2)} \{BBV_i\}$$

where $MED\{X\}$ is the median value of the list X.

• Compute the document blocking artifact measure (DBAM):

$$DBAM = \frac{1}{|U|}\sqrt{\sum_{(k,l)\in U} BM_{k,l}^2}$$

where U is the set of all image blocks.

(a)	(b)
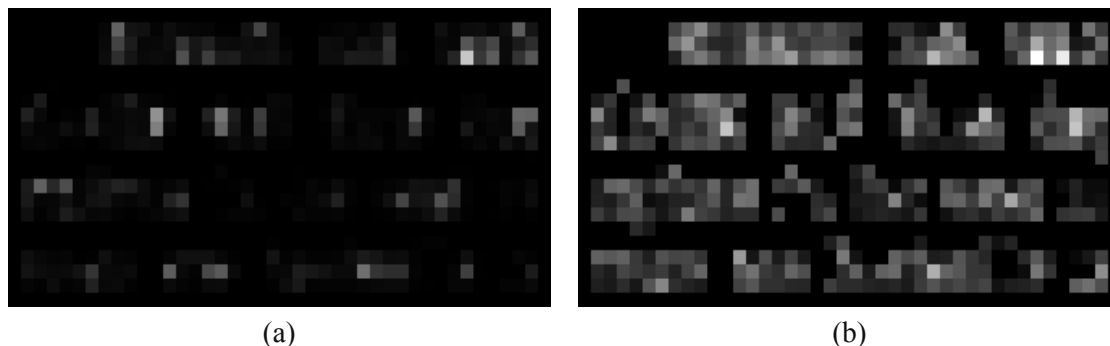
Figure 4. Blockiness measure (BM) map for the image in Figure 2 (higher values, brighter pixels): (a) JPEG quality = 20; (b) JPEG quality = 2

Figure 4 illustrate the $BM_{k,l}$ maps for all the blocks of the image in Figure 2 in which the JPEG quality factor is first set to 20 and then 2. As can be seen in Figure 4(b), when encoding the image at low bit-rate, most of the foreground blocks are disturbed by blocking artifact. To obtain a global evaluation for the entire image, we define a document blocking artifact measure (DBAM) as the mean square root of all the $BM_{k,l}$.

5. Experimental results

5.1. Dataset and experimental settings

The proposed DBAM metric is evaluated for a wide range of bit-rate coding in accordance with the OCR performance. For this purpose, the software ABBYY FineReader 12.0[1] is employed to compute the OCR results. Specifically, OCR accuracy is computed as the ratio of the number of correctly recognized characters to the total characters in the groundtruth. We used the dataset Medical Archive Records (MAR) for OCR recognition from U.S.National Library of Medecine[2]. This dataset contains real documents which are scanned from different types of biomedical journals. Each document contains several zones accompanying with corresponding groundtruth information. For simplification, each zone is independently treated as an image along with its corresponding groundtruth, resulting in 296 images in total. Each image is encoded at 16

---

[1] http://finereader.abbyy.com/professional/features/

[2] http://marg.nlm.nih.gov/

JPEG compression qualities (i.e., $\{1,2,\ldots,16\}$). From the compressed images, the bit-rates are computed and these was found that the obtained bit-rates vary in the range of $[0.1,1.1]$. All the experiments are performed on the following machine configuration: Windows 7 (64-bit), Intel Core i7 (2.1 GHz), 16Gb RAM.

5.2. DBAM characterization results
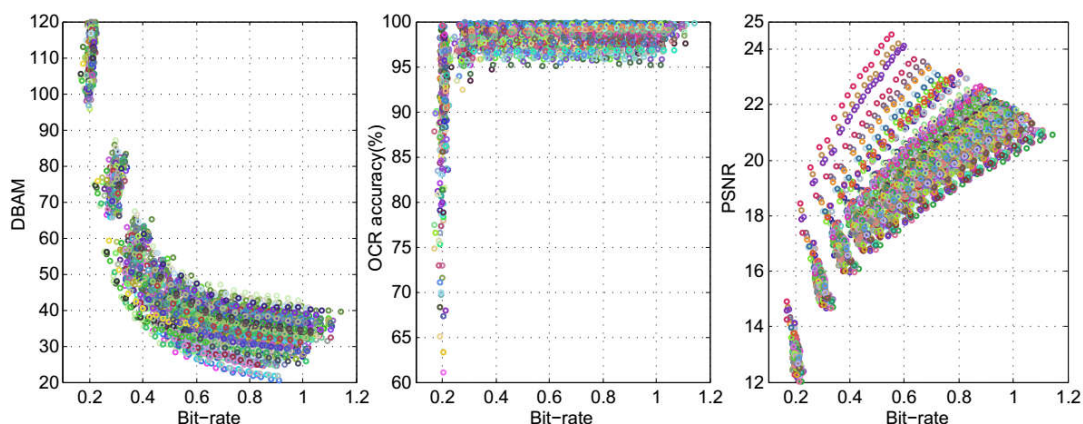
Figure 5. DBAM, OCR accruacy and PSNR for 296 images

Figure 5 presents DBAM results, OCR accuracy and PSNR results over the bit-rates for all the images in the dataset. The common range of DBAM values is in $[10,120]$ (i.e., the smaller the DBAM, the lower the blocking distortion). As can be seen, the DBAM curves have quite similar behavior (i.e., the marginal slope) for all the images. Specifically, the marginal slopes of DBAM values are quite sharp at low bit-rates (i.e., $[0.15,0.3]$) and tend to be gradually stable afterward. The same remark is extracted for the OCR accuracy in which high DBAM values correspond to low OCR performance. Also, OCR results start to be less sensitive to blocking artifact when the bit-rate > 0.3. Consequently, it seems that the correlation between DBAM and OCR results is non-linear, but they can be well represented by piecewise functions of the bit-rate. To be more precise, the first parts of DBAM and OCR results are very linearly correlated up to a specific limit of the bit-rate (e.g., bit-rate < 0.4). However, this degree of linear dependence is greatly dropped when the bit-rate is sufficiently high since both DBAM measure and OCR performance can be virtually modeled by two constant functions.

To validate these propositions, we computed the Pearson correlation coefficient (PCC) between DBAM and OCR results for two intervals of the bit-rate: $[0.1,0.4)$ and $[0.4,1.1]$. The range of PCC is well-defined in the interval of $[-1,1]$ with the senses that perfect linear correlation has the corresponding PCC of 1 (positive correlation) or -1 (negative correlation), and no correlation corresponds to a PCC value of 0. The obtained PCC results are -0.9583 and -0.2635 with respect to the bit-rate intervals $[0.1,0.4)$ and $[0.4,1.1]$. In other words, the

DBAM and OCR results are highly (linear) correlated at low bit-rates and less dependent at high bit-rates.

For comparative evaluation, we computed the peak signal-to-noise ratio (PSNR) between the decompressed images and the original ones. PSNR is a common criterion for measuring image quality of natural images, especially in the domain of image compression, reconstruction and denoising. As can be seen in Figure 5.1, PSNR values are in the range of $[10,25]$ (i.e., higher PSNR, better image quality) and have relative high dispersion for the bit-rates in $[0.3,0.8]$. In addition, we also computed the correlations of PSNR and DBAM to OCR results for the bit-rates in $[0.1,1.1]$. Accordingly, the obtained PCC values are 0.7191 and -0.8729. That said, PSNR is reasonably and positively correlated to OCR accuracy, whereas DBAM is highly and negatively correlated to OCR results.

6. Conclusions

A novel and efficient approach has been presented to compute the blocking artifact measure for document content. In contrast to previous work, the proposed DBAM measure is directly computed in the DCT domain and is dedicated to estimate JPEG artifact distortion when applied to document images. Experiments showed that DBAM is highly correlated to OCR performance and is extremely efficient. Future work would be targeted to optimal document image decompression.

References

[1]   S. Golestaneh and D. Chandler (2014), *No-reference quality assessment of jpeg images via a quality relevance map*, Signal Processing Letters (SPL), vol. 21, no. 2, pp. 155-158.

[2]   C. Park, J. Kim, and S. Ko (2007), *Fast blind measurement of blocking artifacts in both pixel and dct domains*, Journal of Mathematical Imaging and Vision, vol. 28, no.3, pp. 279-284.

[3]   S. Lee and S. J. Park (2012), *A new image quality assessment method to detect and measure strength of blocking artifacts*, Signal Processing: Image Communication, vol. 27, no. 1, pp. 31 - 38.

[4]   S. Liu and A. Bovik (2002), *Efficient dct-domain blind measurement and reduction of blocking artifacts*, Transactions on Circuits and Systems for Video Technology (TCSVT), vol. 12, no. 12, pp. 1139-1149.

[5]   F. Pan, X. Lin, S. Rahardja, E. Ong, and W. Lin (2007), *Using edge direction information for measuring blocking artifacts of images*, Multidimensional Systems and Signal Processing (MSSP), vol. 18, no. 4, pp. 297-308.

[6]   F. Yan, S. Wan, Y. Chang, and Z. Luo (2006), *A no-reference blocking artifact metric for b-dct video*, Journal of Zhejiang University SCIENCE A, vol. 7, no. 1, pp. 95-100, 2006.

[7] L. Meesters and J. Martens (2002), *A single-ended blockiness measure for jpeg-coded images*, Signal Processing, vol. 82, no. 3, pp. 369-387.

[8] S. Suthaharan (2009), *No-reference visually significant blocking artifact metric for natural scene images*, Signal Processing, vol. 89, no. 8, pp. 1647-1652.

[9] S. Minami and A. Zakhor (1995), *An optimization approach for removing blocking effects in transform coding*, Circuits and Systems for Video Technology, IEEE Transactions on, vol. 5, no. 2, pp. 74-82.

[10] G. Triantafyllidis, D. Tzovaras, and M. Strintzis (2002), *Blocking artifact detection and reduction in compressed data*, Transactions on Circuits and Systems for Video Technology (TCSVT), vol. 12, no. 10, pp. 877-890.

[11] M. Barni (2006), *Document and Image Compression*. CRC Press.

[12] H. S. Chang and K. Kang (2005), *A compressed domain scheme for classifying block edge patterns*, IEEE Transactions on Image Processing, vol. 14, no. 2, pp. 145-151, Feb 2005.

RESEARCH STATUS OF WASTE COLLECTION AND TREATMENT FROM AGRICULTURAL PRODUCTION ACTIVITIES ALONG MA AND CHU RIVERS IN THANH HOA PROVINCE

Le Sy Chinh, Pham Do Tuong Linh

Abstract: *Ma and Chu river basins have tributaries across many districts and cities of Thanh Hoa province, such as Thanh Hoa city, Thieu Hoa, Dong Son, Quang Xuong district; four coastal districts: Hau Loc, Nga Son, Sam Son, Hoang Hoa and nine mountainous and midland districts: Quan Son, Quan Hoa, Muong Lat, Ba Thuoc, Ngoc Lac, Thuong Xuan, Vinh Loc and Cam Thuy, Tho Xuan, Yen Dinh. This research has mainly investigated, surveyed and assessed the status of agricultural waste collection and treatment from agricultural production activities in 13 districts and cities, which have significant impact on water quality in Ma and Chu rivers. These research results could be used as practical basics to propose the measures for environmental protection of the basin.*

1. Introduction

Ma river has a total length of 512km, in which 270km flows through districts of Thanh Hoa province including: Muong Lat, Quan Hoa, Ba Thuoc, Cam Thuy, Vinh Loc, Yen Dinh, Thieu Hoa, Thanh Hoa, Hoang Hoa, Quang Xuong, Sam Son... and then enters the sea at three river estuaries: Lach Hoi, Lach Truong and Lach Sung [1]. Chu river is the largest branch of the Ma river system, derived from Sam Nua (Laos) at an altitude of 1,100 meters, running through Vietnam in Thuong Xuan district, Tho Xuan, Thieu Hoa and then joining Ma river at the Giang confluence [2].

With the large scale of catchment area, Ma river basin is now a region with rapid developing economy of the country, there are many establishments, enterprises and households on basin basing on natural resources and their benefits. On this basin there are

Le Sy Chinh
Faculty of Engineering and Technology, Hong Duc University
Email: Lesychinh@hdu.edu.vn (✉)

Pham Do Tuong Linh
Faculty of Engineering and Technology, Hong Duc University
Email: Phamdotuonglinh@hdu.edu.vn (✉)

activities to develop the hydropower, mining, farming, fishing, utilize water resources for daily life, agricultural production and manufacturing facilities, sales close localities, households... bring a prosperous life for the people living along the banks of the Ma river in particular and people in Thanh Hoa province in general. The river also supplies water for two major metropolitan cities of Thanh Hoa and Sam Son. However, agricultural production in the province has generated a relatively large amount of waste with no proper collection and treatment, causing water pollution. This situation has a relative negative impact on the lives and health of people, biodiversity, and fishery production. Therefore, the investigation and assessment of the current status of agricultural waste collection and treatment to assess water pollution in Ma, Chu river is very important and imperative.

2. Objectives and methods

2.1. Objectives

The research investigated, surveyed, assessed the status of agricultural waste collection and treatment in 13 districts where have sources of waste generation and significant impact on water quality in Ma and Chu rivers, including: Quan Hoa, Ba Thuoc, Quan Son, Cam Thuy, Thuong Xuan, Tho Xuan, Vinh Loc, Yen Dinh, Thieu Hoa, Hoang Hoa, Quang Xuong, and cities: Thanh Hoa, and Sam Son.

2.2. General procedures

The research has applied the approach and used methods for analysis and assessment of the current status in wasted collection and treatment from agricultural activities along Ma and Chu rivers:

Practical, systematic and comprehensive approach: In fact, due to the economic - social development demands - water pollution in Ma and Chu rivers are rising worse. Therefore, there is a need to implement the project using practical approach.

Methods of sociological surveys: Through interviewing techniques, how to ask questions (according to the content of prepared questions) to find out the source and type of waste generated from agricultural activities along two Ma and Chu rivers, and applied treatment technology.

Methods of synthesizing data: Based on the survey data, the study has compiled the survey data based on software Excel.

Expert consultation method: Consulted experts in the relevant fields after completion.

The method of collecting, preserving and analyzing samples carried out under the guidance of national or corresponding international standards.

Method of synthetic analysis and comparison: Compared analytical results with national standards and regulations to assessed the current status of waste collection, management and treatment, along with the current status of water quality in Ma and Chu rivers.

3. Results and discussion

3.1. Current status of agricultural waste water collection and treatment

In 2015, the survey showed that most of research districts and cities had no treatment measures for wastewater from agricultural activities after each crop or season. Wastewater was discharged directly into the irrigation systems with various other sources as shown in the Table 1.

Table 1. Receiving sources of agricultural wastewater

No	Locations	No of participants	Receiving sources		
			Water plants	Canal and infield	Directly discharge to Ma, Chu river
1	Yen Dinh	10	3	3	4
2	Cam Thuy	15	4	4	7
3	Vinh Loc	17	7	3	7
4	Hau Loc	2	0	1	1
5	Thanh Hoa city	13	2	1	10
6	Quan Hoa	3	0	0	3
7	Thieu Hoa	16	8	3	5
8	Thuong Xuan	6	2	2	2
9	Tho Xuan	2	1	0	1
10	Hoang Hoa	11	9	2	0
11	Ba Thuoc	1	0	0	1
12	Quang Xuong	1	0	0	1
13	Sam Son	3	0	3	0
	Total	100	36	22	42
	Scale	100%	36%	22%	42%

According to the survey, 42% local residents directly discharged untreated wastewater into Ma, Chu river; 36% reused for watering plants and 22% discharged canals and infield. Results of water quality analysis in Ma, Chu river at 10 water discharge points, sewer and drainage from agricultural fields showed most of the water quality in these areas were contaminated, as follows:

Water quality at the water outfall from upstream areas, in the river confluence between Ma and Lo rivers at Hoi Xuan commune, Quan Hoa district, was contaminated with BOD_5, NO_2 exceeding QCVN 40: 2011/BTNMT 1,046 and 3.5 times respectively.

Water quality at the water outfall from upstream areas, in the river confluence between Ma and Am river at Giao An commune, Lang Chanh district, was contaminated with BOD_5, NO_2 exceeding QCVN 40: 2011/BTNMT 1.05 and 3.7 times respectively.

Water quality in the drainage at Muc Son, Lam Son, Tho Xuan district, discharing to Chu river was contaminated with TSS exceeding 2.33 times; COD exceeding 6.04 times; BOD_5 exceeding 8.96 times; NO_2 exceeding 10.5 times; Amoni exceeding 7.8 times compared to QCVN 40: 2011/BTNMT.

Water quality in the drainage at Xuan Lai, Tho Xuan district, discharing to Chu river was contaminated with TSS exceeding 2.18 times; COD exceeding 4.04 times; BOD_5 exceeding 7.5 times; NO_2 exceeding 18.5 times; Phospho exceeding 2.5 times compared to QCVN 40: 2011/BTNMT.

Water quality in the drainage at Cam Phong, Cam Thuy district, discharing to Chu river was contaminated with TSS exceeding 1.86 times; COD exceeding 4.1 times; BOD_5 exceeding 5.58 times; NO_2 exceeding 18.6 times; Amoni exceeding 4.15 times compared to QCVN 40: 2011/BTNMT.

Water quality in the drainage at Yen Truong, Yen Dinh district, discharing to Ma river was contaminated with TSS exceeding 2.09 times; COD exceeding 4.35 times; BOD_5 exceeding 5.11 times; NO_2 exceeding 29 times; Amoni exceeding 5.3; Clorua exceeded 10 times; Endrin exceeding 3.33 times; DDT exceeding 20 times; Endosunphat exceeding 4 times; Chlordan and Heptachlor exceeding 2 times; Phospho exceeding 1.95 times; Malation exceeding 1.12 times compared to QCVN 40: 2011/BTNMT.

Water quality in the drainage at Xu Nhan, Thieu Duy, Thieu Hoa District, discharing to Chu river was contaminated with TSS exceeding 2.09 times; COD exceeding 4.42 times; BOD_5 exceeding 7.5 times; NO_2 exceeding 29 times; Amoni exceeding 5.1; Phospho exceeding 1.7 times; Malation exceeding 10,625 times compared to QCVN 40: 2011/BTNMT.

Water quality in the drainage at (Phu Quang dyke), Hoang Quang, Thanh Hoa city, was contaminated with TSS exceeding 2.05 times; COD exceeding 5.67 times; BOD_5 exceeding 11.33 times; NO_2 exceeding 20.5 times; Amoni exceeding 5.7; Phospho exceeding 1.05 times compared to QCVN 40: 2011/BTNMT.

Water quality in the drainage (Yen Lac dyke) at Vinh Ninh, Vinh Loc district, discharging to Ma river, was contaminated with TSS exceeding 2.05 times; COD exceeding 6.58 times; BOD_5 exceeding 9.26 times; NO_2 exceeding 27.5 times; Amoni exceeding 8.25; Clorua exceeding 15 times; Endrin exceeding 5 times; DDT exceeding 30 times; Endosunphat exceeding 6 times; Chlordan and Heptachlor exceeding 3 times; Phospho exceeding 2.05 times; Malation exceeding 1.28 times; Coliform exceeding 1.18 times compared to QCVN 40: 2011/BTNMT.

Water quality in the drainage at Quang Cu, Sam Son, discharging to Ma river, was contaminated with TSS exceeding 2.36 times; COD exceeding 7.66 times; BOD_5 exceeding 11.75 times; NO_2 exceeding 26 times; Amoni exceeding 9.15; Phospho exceeding 1.25 times; Coliform exceeding 1.06 times compared to QCVN 40: 2011/BTNMT.

3.2. Current status of agricultural solid waste collection and treatment

Besides, the problem of collecting, processing packaging, bottles containing plant protection chemicals and fertilizers was not strictly controlled, affecting water quality in the infield canals. The survey of environment protection for agricultural production along the Ma and Chu river banks with the participation of environmental officers in the province is displayed in the Table 2.

Table 2. Measures of rural waste disposal

District	No of questionnaire	Waste collection available	Number of landfills	Type of landfill		Plant protection chemical products' trash management		
				Spontaneous	Planning	Collect on 1 position	Treated along with sanitary waste	No treatment
Yen Dinh	10	6	10	2	8	6	2	2
Cam Thuy	15	7	9	6	3	2	5	8
Vinh Loc	17	14	17	6	11	5	12	0
Hau Loc	2	2	2	0	2	0	2	0
Thanh Hoa	13	10	13	1	12	4	5	4
Quan Hoa	3	0	3	3	0	0	1	2
Thieu Hoa	16	11	16	5	11	7	4	5
Thuong Xuan	6	4	6	4	2	0	2	4
Tho Xuan	2	2	2	0	2	2	0	0
Quang Xuong	1	1	1	0	1	0	1	0
Ba Thuoc	1	1	1	0	1	1	0	0
Hoang Hoa	11	9	11	4	7	7	0	4
Sam Son	3	3	1	0	1	1	1	1
Total	100	70	92	31	61	35	35	30
Scale (%)		70	92	34.83	65.17	35	35	30

Collecting waste generated from plant protection chemical products: 30% local authorities had no treatment, 35% conducted collection in one position, and 35% had collection and treatment along with sanitary waste.

For the issue of waste collection and treatment: 70% local authorities collected sanitary waste, 92% having dedicated landfills, in which 34.83% landfills were planned by authorities (highest scales at Vinh Loc, Thieu Hoa, and Thanh Hoa city); spontaneous landfills accounted for 34.83%.

For the waste, by-products from cultivation, harvest agricultural products such as: rice straw, rice hulls, corn, bagasse... local residents have many different treatment methods. The most popular method was to use as fuel. Normally, 80% of generated waste was utilized as fuel, the remaining 20% was treated into fertilizer for crops. Particularly in Tho Xuan district, Lam Son Sugar Company has invested to build a factory producing electricity from bagasse with a total capacity of 12.5 MW. The plant operates on the basis of utilizing bagasse to produce electricity, air to the national grid and mainly serve internal consumer demand.

3.3. Current status of collecting and processing livestock waste

Results of the survey of wastewater collection and treatment at 119 farms were presented in Table 3.

Table 3. Current status of collecting and processing livestock waste

No	Survey results	Number		Scale (%)
I	No treatment	8		6.73
II	Treatment available	111		93.27
Applied technologies		**Efficiency assessment**		
		Good	Normal	Not satisfactory / not effective
2.1	Mechanical methods (sedimentation, filtration, separation by mechanical devices, etc.)	0	0	0
2.2	Chemical and physical methods (flocculation, flotation, etc.)	0	0	0
2.3	Biological methods (aerobic, anaerobic, biological clock, etc.)	30	68	13
2.4	Integrated approach	0	0	0
2.5	Total	30	68	13
2.6	Scale (%)	27.03	61.3	11.7

The investigation and study at 119 farms showed that most farms had conducted wastewater treatment systems (93.27%); others were discharged directly into environment without treatment. The amount of wastewater below 50m^3/day accounted for 97.5% and over 50m^3/day accounted for 2.5%. In fact, most of the farms had constructed wastewater treatment as biogas tanks, sedimentation tanks, biological ponds. There were 101 units of self-design, construction of wastewater treatment projects accounted for 84.87%; the farms consulted hired designers often were large scales, with a herd of about 600-1500. However, wastewater treatment systems at many farms were in substandard conditions with a limited capacity of

biogas tanks, sedimentation tanks, some farms have built biogas tanks without proper settling tanks and biological ponds. This was due to the lack of funds and public lands for construction, as well as constructing limitation, in which the cause of lacking funding accounted for the highest percentage of 68.25%.

The number of wastewater treatment facilities in good operating conditions was 30 (27%), normal was 68 (accounting for 61.3%), and 13 of them had been damaged (accounting for 11.71%). The level of satisfaction of the wastewater treatment accounted for 72.26%, not satisfactory accounted for 27.74%. The frequency of regular operation of wastewater treatment facilities was 91.6%, occasional not to use was 1.68% and 6.72%. The above results showed that most of the farms had built wastewater treatment facilities and regular operation, but the efficiency was not high, mainly due to degradation, damage without repaired and operational inefficiencies, wastewater was being discharged into the environment with signs of pollution, odor and sediment polluting the surrounding environment. Treated waste water of the farm, mostly was being discharged directly into the drainage system (83/119 units accounted for 69.74%) 15/119 discharged into ponds accounted for 12.6%, and 21/119 discharged to storage ponds, or composting tanks for crop irrigation). The by-products arising from the wastewater treatment process of the farm, mostly were sewage, manure, sludge and odor. Measures to handle the byproducts of the farms were periodically to dredged mud, using biological products such as Haniodine, EM. In addition to 66 units had no sludge and odor treatment, the rest had no radical solutions causing accumulating a large amount of wastewater in the drainage areas of the region and odor emission around. There had been some complaints of the people nearby about the pollution from livestock farms affecting the farmers' lives.

In addition, the survey indicated that some farms were currently applying padding technology to process biological waste. This was padding on the livestock barn. This cushion is made of fiber such as sawdust, rice husks, cassava pulp, bagasse. The litter is spread on the floor after raising will be sprayed onto the surface of a layer of useful microbial enzyme systems. Pig farmers using this technology reduce the cost of clean water to 80%, labor 60% and food 10%, no or very little use of veterinary drugs. The breeding process does not use water to wash the barn; Do not use the water for bathing, washing pets thus limiting the amount of wastewater and manure huge. The advantage of this technology is well applied to the large poultry farms and small-scale livestock. However, the downside of this technology is difficult to apply in the hot dry season, if not proceed bath, cooling for livestock animals, the risk of disease is very high.

The collection and management of solid waste, farms manure waste was collected, utilized containers after using and sold to feed fish; waste from veterinary drugs and other solid wastes was virtually collected, burned and buried on site of 92 units (accounting for 76.47%), rent collection and treatment unit of 10 units (accounting for 8.4%) and 18 units sold to collectors for recycling (accounting for 15.12%).

The analysis of environmental quality of treated wastewater in 04 pig farms (Pig farm in Tho Xuan - JSC Phu Gia; pig breeding farm at Thieu Phu, Thieu Hoa district - JSC Phu Gia agricultural products; 02 farms of Pham Van Tuan and Nguyen Van Xuan at Vinh Tan commune, Vinh Loc district; farm at Tan Phuc, Vinh Phuc, Vinh Loc district) compared to QCVN 40: 2011/BTNMT demonstrated some parameters exceeding standards, namely: TSS exceeding from 1,006 to 5.81; COD exceeding from 1.04 to 9.14 times; BOD_5 exceeding 1.94 to 7.22 times; NH_4 from 1.28 to 27.78 times; total N from 5.76 to 11.85 times; total P from 1.04 to 5.6 times; Coliform exceeding from 4.8 to 15 times.

Thus, the wastewater from the farm after the treatment, the concentration of pollutants in wastewater had decreased, however, the quality of wastewater before discharge into the environment still exceeded standards at many parameters.

Regarding the implementation of the Law on Environmental Protection on farms, Family farms surveyed showed:

82.35% of farm owners were instructed educated through mass media and 13.44% were trained by the local authorities.

75/119 units had no records, environmental procedures as prescribed (accounting for 63%), 44 units had established a commitment for environmental protection (37%).

22/44 units had environmental protection commitment, but not implemented (accounting for 50%); 11/44 units performed occasionally (25%) and 11/44 performed regularly (25%).

Number of units had been checked by authorities on the work of environmental protection was 39/119 accounting for 32.88% (in which 10 units were punished for administrative violations of environmental protection), 80 units accounted for 67.22% were not checked accounting for 67.22%. Investigation showed that 100% units were not yet fully implemented the environmental protection measures in the process of breeding, mainly due to lack of funding, lack of human resources who expertise in the environmental protection and knowledge of waste processes and treatment technologies.

3.4. Current state gelling and process of waste of agriculture from the product of agriculture

Wastewater generated from trade villages often had very high concentrations of pollution especially for the food processing industry, farming and slaughter. Most villages had not been invested to build wastewater treatment system or had unefficient operation; wastewater without proper treatment were directly discharged into the environment causing pollution of surface and underground water of surrounding areas. For instance, wastewater generated from a village of reeling, weaving at Hong Do, Thieu Do, Thieu Hoa district with high color was discharged directly through the open drain into the environment with no treatment; Village of perishable cargo services (dogs trade) at Thanh Loc, Hau Loc District, currently having 40 households was separated in a designated business area. Wastewater as fertilizer, household food waste was processed through the septic tank; dead dogs were buried;

Sanitary wastewater contained high concentration of pollutants was not collected and treated properly before releasing into the environment; emissions, odor was not treated affecting local people and nearby.

4. Conclusion

The study showed that farms were more and more rising awareness about environmental protection by investing in waste treatment facilities using various technologies. However, the quality of treated wastewater was not efficient due to old-fashioned technologies. Besides, the operation of these facilities was not conducted regularly or properly, leading to the degradation and damage of system. For agricultural waste, the percentage of districts and towns carried out the collection and treatment of wastewater was very low. This kind of waste is difficult to control due to limiting awareness of most farmers. Sanitary waste was generated in a huge volume and mostly discharged with no treatment. In general, most of areas in Thanh Hoa province do not have a dedicated waste collection and treatment system (except Thanh Hoa city but not yet perfect). The results of this study are to propose suitable treatment solutions.

References

[1]   https://vi.wikipedia.org/wiki/Sông_Mã
[2]   https://vi.wikipedia.org/wiki/Sông_Chu
[3]   QCVN 40:2011/BTNMT National Technical regulations on Industrial wastewater

MODEL PREDICTIVE CONTROL FOR INDUSTRIAL APPLICATIONS OF THREE - PHASE INVERTERS

Tran Hung Cuong, Le Phuong Hao

Abstract: *This paper proposes a Model Predictive Control (MPC) method used for DC-AC converter applications to connect the electrical systems in industry. DC-AC inverters used to convert DC power into AC power for supplying to an AC load. Parameters are controlled in output voltage value or current value, corresponding to voltage source inverter (VSI) inverter and current source inverter (VSC) [1]. DC-AC converter phase three is the main part of the three-phase inverter. Today, controlling for DC-AC inverter has many methods applied [2]-[3]. However, the FCS-MPC method has many advantages: Impact fast, easy to apply, high conversion efficiency, etc. The design procedure of FCS-MPC is based on first, a discrete-time model of the system that is used to predict the behavior of the controlled variables for all the possible switching states of the converter and second, a cost function should be defined according to the control requirements of the system [1]-[2]. The switching state that minimizes the cost function will be selected to be applied to the converter at the next sampling time [4]. This study presents in detail description of a cost function-based predictive control strategy called Finite Control Set Model Predictive Control (FCS-MPC) and its applications to the control of power electronics converters DC-AC.*

1. Introduction

The power electronics converter typically includes the voltage converter DC-DC, DC-AC [3]. DC-AC converter is the device changing direct current into alternating current with the frequency which can be changed and work with independent load [3]. DC power is voltage rectifiers, battery and DC power sources independent. Today, Independent inverter has been widely used in fields such as electricity supply from independent sources such as batteries, AC drive systems, communications, power transmission, metallurgy, energy savings, used in daily life when grid power has been cut... [2]. In fact, three-phase inverters are commonly used

Tran Hung Cuong
Faculty of Engineering and Technology, Hong Duc University
Email: Tranhungcuong@hdu.edu.vn (✉)

Le Phuong Hao
Faculty of Engineering and Technology, Hong Duc University
Email: Lephuonghao@hdu.edu.vn (✉)

because it has large capacity and satisfy industrial applications. Currently, there have been many studies to design the controller for DC-AC converter to create the alternating high quality currents. However, applying the classic controller will be difficult for DC-AC converter high capacity such as the switching frequency of large valves, system power loss, in the alternating currents instability leading to affect the quality of converter [1]. In this paper, Finite Control Set Model Predictive Control will be applied to a simple three-phase voltage source inverter (VSI) which is connected to a typical R-L-e load. The designed controller capabilities are verified by simulating the system in MATLAB/SIMULINK. Model Predictive Control or MPC was first introduced in 1960s. It has more complex calculations compared to classical linear controllers, while it provides faster controller with higher accuracy and stability. From 1980s, the idea of MPC in power electronics applications was introduced despite the lack of fast processors at that time, limited its applications only to low switching frequencies [1]-[2]. Due to invention of fast and powerful processors such as DSP and FPGA, the power electronics industry could take advantages of MPC strategy in practice. Many papers have studied a finite MPC method to control the power converter [4]. Based on MPC, three alternatives have been introduced in order to reduce its high amount of calculations; Generalized Predictive Control (GPC), Explicit MPC and Finite Control Set MPC (FCS-MPC). The focus of this study will be on FCS-MPC, because FCS-MPC is a powerful control technique that has several advantages such as high accuracy, flexibility and stability, easy implementation, simple and understandable concepts, but the most important and exclusive feature of this control strategy is the inclusion of nonlinearities and system constraints in the cost function. As a result, all the control requirements can be considered by one controller at the same time [4 - 8]. The details are described in the following parts. In Section 2, the system structure and operating principles of the DC-AC are introduced. Section 3 presents the design of control system. In Section 4, simulations studies analyses are carried out in the Matlab/Simulink software. Conclusions are summarized in Section 5.

2. The DC-AC three phase voltage source converter

2.1. Structure DC-AC converter

Three-phase/two-level voltage source inverter is a very well-known topology in power electronics. It has six power switch-diode combinations. The circuit diagram of the three-phase inverter connected to an RLe load has been illustrated in Figure1.
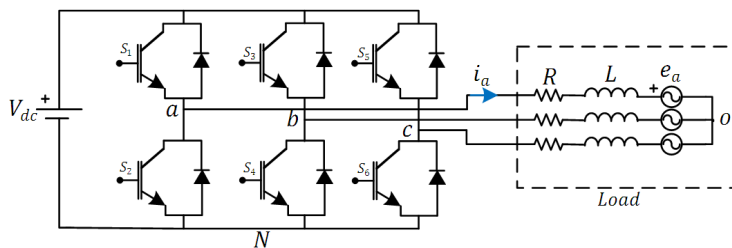

Figure 1. *Voltage source inverter power circuit*

IGBT has been selected to be power switches. The transient switching time will be neglected and only two possible states for each IGBT is going to be assumed that are completely ON or completely OFF. These switching states are not acceptable:

Both of switches in each phase are ON at the same time (short circuiting the dc link).

Both of switches in each phase are OFF at the same time (no power transfer) Consequently, eight (23) possible switching states can be found (Table 1).

The load consists of three branches of a resistor (R), an inductor (L) and a voltage source (e) that have been connected together in star shape. This voltage source can be a representation of motor back emf.

2.2. Modeling of DC-AC converters

As space vector analysis is a good method in order to simplify three phase equations to a single equation, the mathematical equation of the load will be:

$$v = L\frac{di}{dt} + Ri + e \qquad (1)$$

Where v, i and e are the representations of the inverter terminal voltage, phase currents and load back emf space vectors, respectively. They can be found by the following equations based on the space vector theorem.

$$i = \frac{2}{3}\left(i_a + ai_b + a^2 i_c\right) \qquad (2)$$

$$e = \frac{2}{3}\left(e_a + ae_b + a^2 e_c\right) \qquad (3)$$

$$v = \frac{2}{3}\left(v_{aN} + av_{bN} + a^2 v_{cN}\right) \qquad (4)$$

$$a = e^{j\frac{2\pi}{3}} = -\frac{1}{2} + j\frac{\sqrt{3}}{2} \qquad (5)$$

Based on this approach and the inverter topology depicted in Figure 1, the relation between switching states and terminal voltage can be found (Table 1).

Table 1. Switching states and voltage vectors

State	S_1	S_2	S_3	S_4	S_5	S_6	Inverter terminal voltage space vector v
0	0	1	0	1	0	1	$v_0 = 0$
1	1	0	0	1	0	1	$v_1 = \frac{2}{3}V_{dc}$
2	0	1	1	0	0	1	$v_2 = \frac{1}{3}\left(-1 + j\sqrt{3}\right)V_{dc}$
3	0	1	0	1	1	0	$v_3 = \frac{1}{3}\left(-1 - j\sqrt{3}\right)V_{dc}$

4	1	0	1	0	0	1	$v_4 = \dfrac{1}{3}\left(1 + j\sqrt{3}\right)V_{dc}$
5	1	0	0	1	1	0	$v_5 = \dfrac{1}{3}\left(1 - j\sqrt{3}\right)V_{dc}$
6	0	1	1	0	1	0	$v_6 = -\dfrac{2}{3}V_{dc}$
7	1	0	1	0	1	0	$v_7 = 0$

3. Proposed MPC strategy based on the mathematical model of the DC-AC converter

3.1. Introduction of Model Predictive Control

The operating principle of MPC based on the cost function can contain different linear functions and depend on the characteristics of each system [8].

Where $x(k)$ is the controlled variables. Based on the discrete model of system (load and converter), the current values of the controlled variables $x(k)$ are used to predict their future values $x(k+1)$ for all N possible switching states. All the predicted values of the controlled variables $x(k+1)$ are compared with their reference values $x_{ref}(k+1)$ in the cost function minimization block. Finally, the switching state (S) that minimizes the cost function will be selected as the next switching state and it will be applied to the converter. The procedure of switching state selection has been shown in Figure 3; t_k is presenting the current state, t_{k+1} and t_{k+2} are the next time steps. The sampling time is T_s.
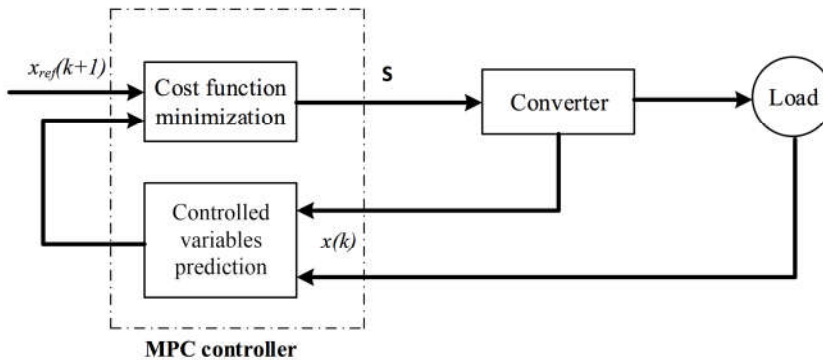
Figure 2. *The control lock diagram of MPC*

MPC model applied to the inverter power electronics began with discrete variables such as current, voltage, etc. The cost function must be determined according to the desired behavior of the system. At each sample time, the cost function will calculate all the switching status for the next sample cycle based on the present state. Then, the optimal state will be selected to apply for the conversion. In designing controller MPC for power electronics there are three phases: Perform discrete model of the system under control variables to be able to predict the future of the variable; Identify all the switching states for conversions and their

relationship with other variables; Determine the cost function to calculate the optimum value representing the desired behavior of the system.

3.2. MPC strategy of the DC-AC converter

At the beginning of the controller design, the system model should be discretized with Ts as sampling period and one of Euler methods; forward, backward or midpoint [5]. Then, a cost function based on the control requirements will be defined follow Forward Euler method.

By applying this method on Eq 1, the system model will be found as follows:

$$i(k+1) = \left(1 - \frac{T_s R}{L}\right) i(k) + \frac{T_s}{L} \left(v(k) - e(k)\right) \tag{6}$$

Where k is the presentation of the instant that the last switching state has been applied to the inverter (it is very close to now) and k+1 represents the next sampling instant. (k) is measured, $v(k)$ is assumed to be approximately equal to $v(k + 1)$ that is the future value of the inverter terminal voltage. There are 7 different values related to $(k + 1)$ depending on the switching states (Table 1). Finally, (k) can be simply measured or estimated by $e(k - 1)$, if the sampling frequency is high enough. In other words, it can be approximated constant $((k) \approx e(k-1))$ in one sampling time. By rewriting Eq. 6 based on the previous step time, $(k - 1)$ can be found:

$$e(k) \approx v(k-1) - \left(\frac{L}{T_s}\right) i(k) + \frac{L - RT_s}{T_s} i(k-1) \tag{7}$$

[3] has used this method.

3.3. Cost function definition

According to the system model, the cost function can be defined as:

$$J = \left| i_\alpha^*(k+1) - i_\alpha(k+1) \right| + \left| i_\beta^*(k+1) - i_\beta(k+1) \right| \tag{8}$$

Where $i(k + 1)$ and $i_\beta(k + 1)$ are the real and imaginary parts of the load currents that are predicted by mathematical system model and $i_\alpha^*(k+1)$, $i_\beta^*(k+1)$ is the presentation of the controlled variables reference value. In high sampling frequency, the reference current can be approximated to be constant during a step time for simplification purposes.

$$J = \left| i_\alpha^*(k) - i_\alpha(k+1) \right| + \left| i_\beta^*(k) - i_\beta(k+1) \right| \tag{9}$$

Since the cost function in this case has two parts with the same unit, the weighting factor is not needed. The FCS-MPC controller repeats the control algorithm at each time step in order to find the switching state that minimizes the predefined cost function. The selected switching state will be applied to IGBTs' gates. It is worth mentioning that there is no need for pulse width modulation. In addition, the switching frequency is not fixed in contrast with an ordinary PWM controller and it can be minimized by additional terms to the cost function.

4. Simulation results

This section evaluates the performance of grid connected DC-AC converter of Figure. 1 that operates based on the proposed MPC strategy. The simulation studies are conducted in the MATLAB/SIMMULINK environment to demonstrate the performance of the proposed MPC strategy in terms of control current AC side. The inverter is assumed to be connected to a utility grid load. Table 2 contains the inverter and load parameter as well as sampling frequency.

Table 2. *Parameters of the study system illustrated in Figure 1*

V_{DC}	6.6 kV	R	0.3 Ω
e	3.3kV	L	2.5 mH
f	50 Hz	T_s	100 μs
$I_{nominal}$	3.5 kA	f_s	10 kHz

Figure 3 illustrates the schematic of the system depicted in SIMULINK. The reference currents are fixed sinusoidal waveforms with amplitude equal to nominal current (3500 A) and 50 Hz frequency.
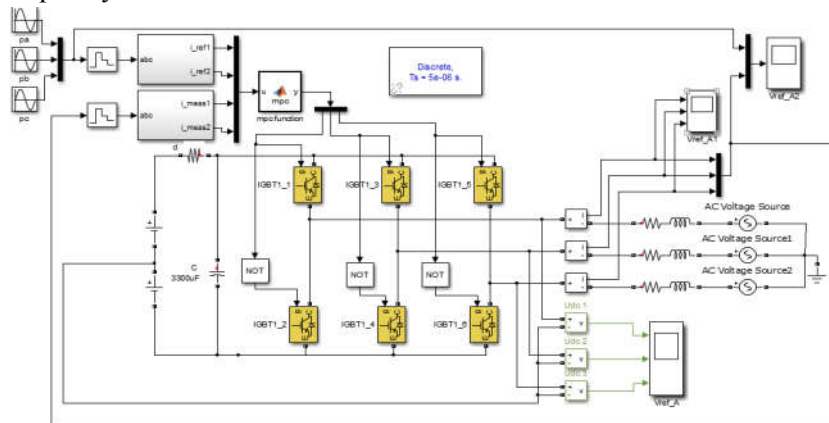
Figure 3. *Circuit model built in SIMULINK*

The output currents have been illustrated in Figure 4 when applying all the Euler methods. It can be seen that the proposed FCS-MPC control method is very successful in reference tracking. All Euler methods provide satisfying performance although midpoint Euler method establishes more accurate currents with the least ripple.
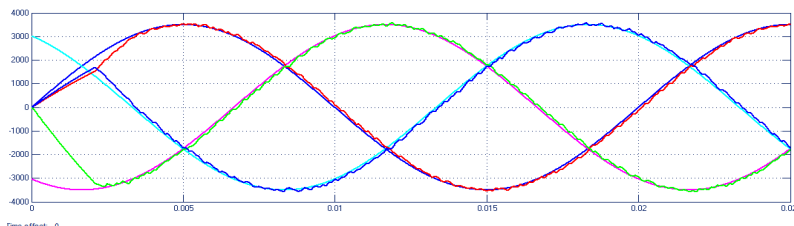

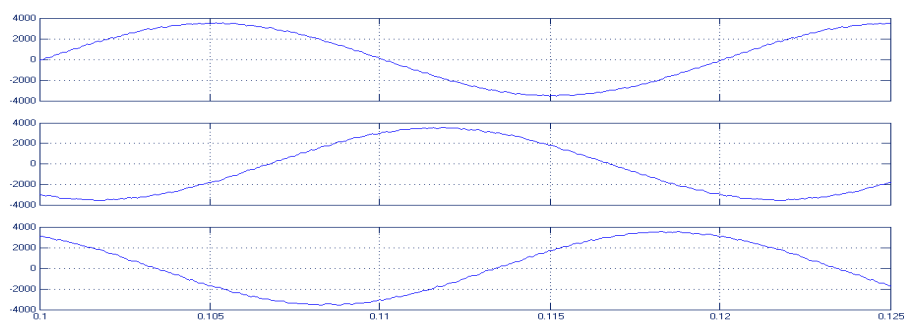**Figure 4.** *The three-phase load currents using Euler methods*

Figure 5. *The three-phase load currents using Euler methods in the next cycle*
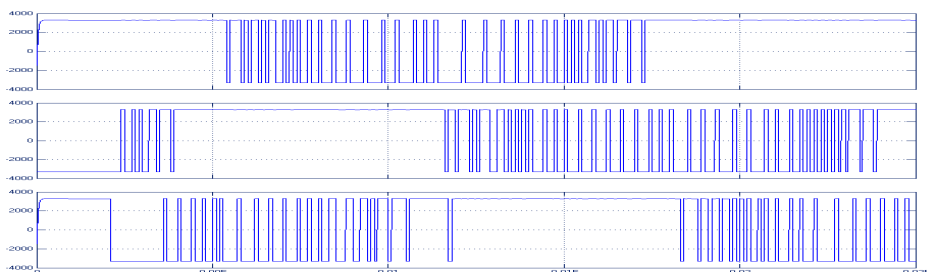
Figure 6. *The inverter phase-a pole voltage (V) using Euler methods*

5. Conclusions

This paper proposes an MPC strategy for a DC-AC converter. Based on the concept of predictive control, a discrete-time mathematical model of a DC-AC is derived. The discrete model is used to minimize a defined cost function associated with the internal control objectives of an DC-AC, the simulation results prove the accurate and fast performance of the proposed FCS-MPC applied on a three-phase voltage source inverter. The controlled variables (load currents) are forced to follow their reference signals by the controller. All the Euler methods for discretizing the load equation provide acceptable results. Effectiveness of the proposed control strategy for a DC-AC converter under various operating conditions, is evaluated based on simulation studies in the MATLAB/SIMMULINK environment.

References

[1]   Specialization Project, Razieh Nejati Fard (2013), *Predictive Control in Power Electronics Converters*.

[2]   First Edition, Jose Rodriguez and Patricio Cortes (2012), *Predictive Control of Power Converters and Electrical Drives.*

[3]   P. Cortes, M.P.Kazmierkowski, R. M. Kennel, D. E. Quevedo, J. Rodriguez (2008), *Predictive Control of in Power Electronics and Drives*, IEEE Transactions on Industrial Electronics, vol. 55, no. 12, pp. 4312-4324.

[4]   http://en.wikipedia.org/wiki/Backward_Euler_method

[5]   J. Rodriguez, J. Cortes, R. M. Kennel, M. P. Kazmierkowski (2009), *Model predictive control a simple and powerful method*, IEEE Power Electronics and Motion Control Conference, Chile.

[6]   P. Cortes, J. Rodriguez, R. Vargas and U. Ammann (2006), *Cost function-based predictive control for power converters*, Proc. 32nd Annu. IEEE IECON, pp.2268 - 2273.

[7]   M.A. Perez, E. Fuentes, J. Rodríguez (2010), *Predictive current control of ac-ac modular multilevel converters*, in Proc. IEEE International Conference on Industrial Technology (ICIT), Valparaíso, Chile, pp. 1289-1294.

[8]   J. M. Maciejowski (2002), *Predictive Control*. Englewood Cliffs, NJ: Prentice-Hall.

A CERTIFICATELESS SIGNATURE SCHEME WITHOUT RANDOM ORACLES

Trinh Viet Cuong

Abstract: *In the context of certificateless public key cryptography, there is no need to use the certificate to certify the public key, and neither the user nor the authority can derive the full private key by himself. There have been several efforts to propose a certificateless signature (CLS) scheme in the standard model, but all of them either make use of the Waters' technique or of the generic conversion technique which both lead to inefficient schemes. In this paper, we introduce a new and direct approach to construct a CLS scheme, secured in the standard model, with constant-size of all parameters and having efficient computing time. Our scheme is therefore very efficient when comparing to existing CLS schemes in the standard model.*

Keywords: *Certificateless, signature, standard model, strong adversary.*

1. Introduction

The era of modern cryptography has started with the introduction of public key cryptography (PKC). In the context of PKC, each user possesses a private key (e.g., to digitally sign a message) and a corresponding public key (e.g., to verify the obtained signature). To verify whether a public key belongs to the correct identified user, the public key needs to be associated to a certificate provided by a trusted Certificate Authority (CA), introducing the notion of Public Key Infrastructure (PKI). During the life-cycle of e.g., a signature scheme, the PKI is therefore in charge of providing, maintaining and revoking a large amount of certificates, which requires using a lot of resources when deployed in the real world. To deal with this drawback, Shamir [13] has introduced the concept of identity-based cryptography for which the public key of a user is exactly his/her identity, such as his/her phone number or email address. The corresponding private key is next generated by some private key generator (PKG), from a master secret key and the identity of the requesting user. However, identity-based cryptography naturally suffers an important disadvantage (named key escrow problem): the PKG knows the private key of all users. One basic solution is to distribute the key of the PKG into several entities. But first, such distribution is not compatible with all identity-based schemes, or leads to non-efficient solutions. And second, the whole infrastructure may become too complex for a practical deployment.

Trinh Viet Cuong

Faculty of Information and Communication Technologies, Hong Duc University

Email: Trinhvietcuong@hdu.edu.vn (✉)

Certificateless Cryptography. To eliminate this new problem, Al-Riyami and Paterson have introduced in [1] the notion certificateless cryptography. There is still no need for a certificate and, this time, the PKG has no way to obtain the user private key. In fact, the key is computed by both the PKG and the user such that only the latter obtains the result. The part which is still provided by the PKG is computed from a master secret key and the user's identity.

We now focus on the case of certificateless signature (CLS) schemes and give some words about related work before explaining our contribution on this topic.

1.1. Related work on certificateless signature schemes

To date, there have been numerous efforts to propose CLS schemes in both the random oracle (using hash function in the construction and then model it as random oracle in the security proof) [1], [9], [21], [4], [14], [16], [8] and the standard models (not model hash function as random oracle in the security proof) [20], [7], [10], [17], [19], [18]. Al-Riyami and Paterson [1] have proposed the first CLS scheme, but Huang et al. [9] have then pointed out that their work is insecure.

Regarding constructions secure on the random oracle model, Zhang et al. [21], Choi et al. [4], and Tso et al. [14] have proposed three efficient CLS schemes, where all parameters are of constant-size. In [8], Huang et al. go one step further by revisiting the security model and proposing two efficient constructions in the random oracle model.

We now focus on the constructions that are secure in the standard model. In this case, there are currently two types of constructions in the literature.

Using Waters' hash function. In [15], Waters has proposed a new hash function technique that can be used to map an identity (of arbitrary length) to a key (of fixed bit length) in a CLS scheme. The main problem of such technique is that it leads to relatively large public parameters and heavy computing time. More precisely, both the space and time complexities are a function of the size of the expected fixed bit length. One possibility is then to apply the Naccache's [11] or Chatterjee-Sarkar's [3] techniques to reduce this fixed length, but the price to pay is either a security loss or a less efficient scheme.

The first concrete construction using Waters' hash function has been given by Liu et al [10]. Three other schemes can now be found in the literature [17], [19], [18].

Yum-Lee generic transformation. In [20], Yum and Lee have introduced a generic construction for certificateless signature schemes (applied in both the random oracle and the standard models). The first step of this construction consists in designing an identity-based signature (IBS) scheme and then combining it with a standard signature (SS). The resulting efficiency for the CLS scheme is however approximately worse than the one of the chosen IBS plus the one of the chosen SS. Moreover, a way to construct an IBS scheme is to apply the folklore conversion technique which either uses two SS schemes or a 2-level Hierarchical Identity-Based Encryption (but we then fall into the above case of using Waters' technique). Again, the resulting efficiency is approximately three times worse than the efficiency of the underlying SS scheme. It is also worth to remark that Hu et al. [7] have pointed out that Yum

and Lee's technique is insecure against a Type I forger. They have next given a modification but at the price of a loss in terms of efficiency.

To the best of our knowledge, it then remains an open problem to design a truly efficient CLS scheme secure in the standard model. In this paper, we propose such construction by providing a new technique.

1.2. Our contribution and organization of the paper

Our construction is based on the stacking of the Boneh-Boyen BB standard signature [2] in the recent Pointcheval-Sanders PS one [12], both secure in the standard model. More precisely, the generator used in the PS signature corresponds to a BB signature including the master secret key and user's identity. Adding one element in the signature, we obtain a unique pairing equation to verify both the validity of our CLS and the one of the related public key, instead of two if basically applied together, or if other standard signature schemes are used.

Our resulting scheme enjoys the constant-size of all parameters together with an efficient computing time. It is therefore the most efficient CLS scheme in the standard model to date. We give in Table 1 the detailed comparison among our CLS scheme and most relevant other existing CLS schemes secure in the standard model.

Table 1. *Comparison between our scheme and some previous CLS schemes in the standard model. n_u, n_m are the fixed length corresponding to the parameters of the Water's function. E, P and M_G denote the exponentiation in a group G, the pairing computation and the multiplication in a group G, respectively. $|Sig|, |pk|, Sign, Verify$ denote the signature size, public key size, signing time, verifying time of a SS secure in the standard model, respectively*

	Sig size	Public key size	Singing time	Verifying time
[10]	$3|G|$	$(n_u + n_m + 5)|G|$	$5E + \left(\dfrac{n_u + n_m}{2} + 3\right)M_G$	$6P + \dfrac{n_u + n_m}{2}M_G + 2M_{G_T}$
[19]	$4|G|$	$(n_u + n_m + 4)|G|$	$9E + \left(\dfrac{n_u + n_m}{2} + 7\right)M_G$	$6P + \dfrac{n_u + n_m}{2}M_G + 2M_{G_T}$
[17]	$3|G|$	$(n_u + n_m + 5)|G|$	$5E + \left(\dfrac{n_u + n_m}{2} + 3\right)M_G$	$3P + \dfrac{n_u + n_m}{2}M_G + 1E + 2M_{G_T}$
[18]	$4|G|$	$(n_u + 7)|G|$	$6E + \left(\dfrac{n_u}{2} + 4\right)M_G$	$5P + \dfrac{n_u + 1}{2}M_G + 1E + 2M_{G_T}$
[7]	$3|Sig| + 1|pk|$	$1|pk|$	$2Sign$	$3Verify$
Ours	$4|G|$	$7|G|$	$6E + 2M_G$	$3P + 6M_G + 2E$

Paper organization. The next section introduces definition for a CLS scheme. Section 3 gives some tools that we will need for our main construction. In Sections 4 we give our CLS scheme and its security analysis.

2. Certificateless signature scheme

We recall in this section the definition for a CLS scheme, based on the work given in [8]. A certificateless signature scheme requires three actors: a designated authority acting as a Private Key Generator PKG, a signer and a verifier.

Informally speaking, the main difference between a standard signature scheme and a certificateless signature scheme is the way keys are generated. In a CLS scheme, the key generation process is divided into four steps which finally permits to compute the user private key SK_{ID}, computed from both a secret value x_{ID} chosen by the user him/herself and a partial private key D_{ID} generate by the PKG from a master key and the user's identity.

More formally, a CLS scheme consists of seven probabilistic algorithms.

Setup: This algorithm takes as input a security parameter λ and returns the system parameters param and a master secret key *msk*.

Partial-Private-Key-Extract: This algorithm takes as input param, the master key *msk* and a user's identity ID. It returns a partial private key D_{ID} devoted to the user with identity ID.

Set-Secret-Value: This algorithm takes as input the security parameter λ and a user's identity ID and returns the user's secret value x_{ID}

Set-Public-Key: This algorithm takes as input a user's secret value x_{ID}. It returns the user's public key PK_{ID}.

Set-Private-Key: This algorithm takes a user's partial private key D_{ID} and public key PK_{ID}, and his secret value x_{ID} as input. It returns the user's full private key SK_{ID}.

Sign: This algorithm takes param, a message *m*, and a user's full private key SK_{ID} as input. It returns a signature σ.

Verify: This algorithm takes param, a message *m*, a user's identity ID, a public key PK_{ID}, and a signature σ as input. It returns 1 if σ is a valid signature of the message *m* and 0 otherwise.

Regarding efficiency, the main purpose of a certificateless signature scheme is to give a verification phase for which the time complexity does not correspond to the verification of the signature (output by Sign) plus the verification that the partial private key is a correct one (that is, output by Partial-Private-Key-Extract and derived by the PKG).

3. Preliminaries

In this section, we give some useful tools we will need all along the paper. If needed, some other details will be given directly in the description of our scheme, when necessary.

In the sequel, a standard signature scheme SS is given by the three algorithms (KeyGen, Sign, Verify).

3.1. Bilinear groups

Let $G, \widetilde{G}$ and G_T denote three finite multiplicative abelian groups of large prime order $p > 2^{\lambda}$ where λ is the security parameter. Let g be a generator of G and $\widetilde{g}$ be a generator of $\widetilde{G}$. We assume that there exists an admissible asymmetric bilinear map $e : G \times \widetilde{G} \to G_T$, meaning that for all $a, b \in Z_p$.

1. $e\left(g^a, \widetilde{g}^b\right) = e(g, \widetilde{g})^{ab}$;

2. For $g \neq 1_G$ and $\widetilde{g} \neq 1_{\widetilde{G}}, e(g, \widetilde{g}) \neq 1_{G_T}$

3. $e(g, \widetilde{g})$ is efficiently computable.

In the sequel, the set $\left(p, G, \widetilde{G}, G_T, g, \widetilde{g}, e\right)$ is called a bilinear map group system. In this paper, we consider in the sequel type 3 pairings where there is no efficiently computable homomorphism $\left(\phi : G \to \widetilde{G}\right)$ exist between G and $\widetilde{G}$ in either direction [5].

3.2. Boneh-Boyen signature scheme

Boneh and Boyen have proposed in [2] short signature schemes (named BB for short), secure in the standard model, under the q-SDH assumption [2]. In this paper, we make use of the weak version of the BB signature.

In a nutshell, the BB scheme requires a bilinear map group system $\left(p, G, \widetilde{G}, G_T, g, \widetilde{g}, e\right)$ and works as follows (details can be found in [2]).

KeyGen: The secret key $s \in Z_p^*$, the corresponding public key is $\widetilde{w} = \widetilde{g}^s$.

Sign: On input the secret s, the signature of a message $m \in Z_p$ is obtained by computing $\sigma = g^{1/(s+m)}$.

Verify: On input a message m and the corresponding signature σ, together with the public key w, anybody can verify the validity of $\widetilde{\sigma}$ by checking that:

$$e\left(\sigma, \widetilde{w} \widetilde{g}^m\right) = e(g, \widetilde{g})$$

3.3. Pointcheval-Sanders signature scheme

Recently, Pointcheval and Sanders have proposed in [12] a new construction for a signature scheme (called PS in the sequel) with additional features. They prove the security of their construction in the standard model, under a new assumption they have introduced, called PS assumption 1, and given below.

In a nutshell, the PS scheme necessitates a bilinear map group system $\left(p, G, \widetilde{G}, G_T, g, \widetilde{g}, e\right)$ and works as follows (details can be found in [12]).

KeyGen: The secret key is a tuple $(x, y) \in Z_p^*$, and the public key is composed of a random generator $\widetilde{h} \in \widetilde{G}$ and the corresponding tuple $\left(\widetilde{X}, \widetilde{Y}\right)$ where $\widetilde{X} = \widetilde{h}^x$ and $\widetilde{Y} = \widetilde{h}^y$

Sign: On input the secret (x, y), the signature of a message $m \in Z_p$ is obtained by selecting a random $h \overset{\$}{\leftarrow} G$ and outputs $\sigma = (\sigma_1, \sigma_2)$ where $\sigma_1 = h$ and $\sigma_2 = h^{(x+ym)}$

Verify: On input a message m and the corresponding signature $\sigma = (\sigma_1, \sigma_2)$, together with the public key $\left(\widetilde{h}, \widetilde{X}, \widetilde{Y}\right)$, anybody can verify the validity of σ by checking that:

$$\sigma_1 \neq 1_{G_1};$$
$$e\left(\sigma_1, \widetilde{X}\widetilde{Y}^m\right) = e(\sigma_2, \widetilde{g})$$

4. Construction and security analysis

We are now ready to describe our construction. We first describe a high-level intuition of the construction and the security analysis.

4.1. Intuition and security analysis

Intuitively, the master secret key s is a BB signing key and our certificateless signature corresponds to a PS signature by the user, with a BB signature as a generator, that is $h = g^{\frac{1}{s+ID}}$.

The user's partial private key is then a triplet corresponding to a true PS public key, using the above h and a secret key (x, y) which is common to all users. The differentiation between users is done by using a secret value b_i to randomize the PS secret key, as $(x + b_i, y)$. Such key finally helps the user (using x and y "in blind", i.e., without knowing them) to compute the certificateless signature as a PS signature. More precisely, we use the randomization technique of a PS signature, as described in [12].

Regarding security, the unforgeability of the Boneh-Boyen's signature scheme ensures that the adversary cannot derive the partial private key of the target user. The security of the Pointcheval-Sanders' signature scheme then prevents the adversary from forging a valid signature of the target user, on a new message.

Regarding efficiency, the main point is that, using BB and PS signature schemes in the above somewhat generic description, we have found that they are totally compatible in our certificateless setting. In fact, we can arrange the verification equations to have only one single pairing equation to be directly convinced that both the user's whole public key and the given signature are valid.

We now give the details of our construction.

4.2. Detailed description

The construction of our CLS scheme is detailed as follows.

Setup $\left(1^{\lambda}\right)$: The algorithm takes as input the security parameter λ, generates a bilinear map group system $\left(p, G, \widetilde{G}, G_T, g, \widetilde{g}, e\right)$. Let $s, x, y \overset{\$}{\leftarrow} Z_p^*$

The public parameters *param* are then

$$param = \left(g, \widetilde{g}, \widetilde{S} = \widetilde{g}^s, \widetilde{X} = \widetilde{g}^x, \widetilde{Y} = \widetilde{g}^y, X = g^x, Y = g^y\right)$$

and the master secret key is *msk* = s.

Partial-Private-Key-Extract: It takes as input param, $msk = s$, and the identity ID of user *i*. For notational simplicity, we suppose that identity $ID_i \in Z_p^*$. It returns a partial private key

$$D_{ID_i} = \left(D_{1,i}, D_{2,i}, D_{3,i}\right) = \left(g^{\frac{x}{s+ID_i}}, g^{\frac{y}{s+ID_i}}, g^{\frac{1}{s+ID_i}}\right)$$

for user *i*.

Set-Secret-Value: It takes as input user's identity ID_i. It chooses random values $b_i \overset{\$}{\leftarrow} Z_p^*$ and returns $x_{ID_i} = b_i$ as user *i*'s secret value.

Set-Public-Key: It takes as input param, x_{ID_2} and returns $PK_{ID_2} = \widetilde{g}^{b_i}$ as the public key for user *i*.

Set-Private-Key: It takes as input x_{ID_i}, D_{ID_i} and returns $SK_i = \left(x_{ID_i}, D_{ID_i}\right)$ as the full private key for user *i*.

Sign: It takes as input param, ID_i, SK_i, and a message *m*. For notational simplicity, we suppose that $m \in Z_p$. The algorithm chooses $r \overset{\$}{\leftarrow} Z_p^*$ and computes:

$$U = \left(D_{1,i}\right)^r \left(D_{2,i}\right)^{mr} \left(D_{3,i}\right)^{b_i r} = g^{\frac{(x+b_i+my)r}{s+ID_i}}, \ V = \left(D_{3,i}\right)^r = g^{\frac{r}{s+ID_i}}$$

$$W = g^r, L = \widetilde{Y}^{\frac{b_i}{r}} = \widetilde{g}^{\frac{b_i y}{r}}$$

It returns $\sigma = \left(U, V, W, L\right)$ as the signature on the message *m*.

Verify: It takes as input param, PK_{ID_i}, ID_i, $\sigma = \left(U, V, W, L\right)$ and a message *m*, and computes $U' = \widetilde{S}.\widetilde{g}^{ID_i}$ and $W' = \widetilde{X}.PK_{ID_i}.\widetilde{Y}^m.\widetilde{g}$.

It then checks if $e\left(U.V, U'\right).e\left(W, L\right) = e\left(W, W'\right).e\left(Y, PK_{ID_i}\right)$ holds. If this is the case, it outputs 1. Otherwise, it outputs 0.

Completeness. We can easily show that:

$$e(U.V, U').e(W, L) = e\left(g^{\frac{(x+b_i+m.y).r}{s+ID_i}} \cdot g^{\frac{r}{s+ID_i}}, \widetilde{g}^s \cdot g^{ID_i} \right).e\left(g^r \cdot \widetilde{g}^{\frac{b_i y}{r}} \right)$$

$$= e\left(g^r, \widetilde{g}^{x+b_i+m.y+1} \right) e\left(g^y, \widetilde{g}^{b_i} \right) = e(W, W').e(Y, PK_{ID_i})$$

4.3. Efficiency considerations

Regarding efficiency, as shown in Table 1, it is obvious that the signature generation necessitates one multi exponentiation in G, two additional modular exponentiations in G and one modular exponentiation in $\widetilde{G}$.

The verification phase consists in executing 2 exponentiations and 4 multiplications in $\widetilde{G}$ and then check the pairing equation. As this the latter can be written

$$e(U.V, U').e(W, L/W') = e(Y, PK_{ID_i})$$

it suffices to compute 3 pairings, one multiplication in G, and one in $\widetilde{G}$ for this step.

5. Conclusions

In this paper, we focus on CLS scheme in the standard model, we in fact introduce a new and direct approach to construct an efficient CLS scheme in the standard model, while the existing approaches either make use of the Waters' technique or use the generic conversion technique which both lead to inefficient CLS schemes.

References

[1] S. Al-Riyami and K. G. Paterson (2003), *Certificateless public key cryptography*. In C.-S. Laih, editor, Advances in Cryptology - *ASIACRYPT*.

[2] D. Boneh and X. Boyen (2008), *Short signatures without random oracles and the SDH assumption in bilinear groups*, J. Cryptology, 21(2):149-177.

[3] S. Chatterjee and P. Sarkar (2005), *Trading time for space: Towards an efficient IBE scheme with short(er) public parameters in the standard model*, ICISC'05 Proceedings of the 8th international conference on Information Security and Cryptology.

[4] K. Y. Choi, J. H. Park, J. Y. Hwang, and D. H. Lee (2007), *Efficient certificateless signature schemes*, 5th International Conference on Applied Cryptography and Network Security, ACNS 2007 - Zhuhai, China.

[5] S. D. Galbraith, K. G. Paterson, and N. P. Smart (2008), *Pairings for cryptographers*, Discrete Applied Mathematics, 156(16):3113-3121.

[6] S. Goldwasser, S. Micali, and R. L. Rivest (1988), *A digital signature scheme secure against adaptive chosen-message attacks*, SIAM Journal on Computing.

[7] B. C. Hu, D. S. Wong, Z. Zhang, and X. Deng (2006), *Key replacement attack against a generic construction of certificateless signature*, Conference: Information Security and Privacy, 11th Australasian Conference, ACISP 2006, Melbourne, Australia, July 3-5, 2006, Proceedings.

[8] X. Huang, Y. Mu, W. Susilo, D. S. Wong, and W. Wu (2012), *Certificateless signatures: New schemes and security models*, The Computer Journal.

[9] X. Huang,W. Susilo, Y. Mu, and F. Zhang (2005), *On the security of certificateless signature schemes from Asiacrypt 2003*, in: CANS 05, LNCS 3810, pp.13-25.

[10] J. Liu, M. Au, and W. Susilo (2007), *Self-generated-certificate public key cryptography and certificateless signature/encryption scheme in the standardmodel*, ASIACCS '07 Proceedings of the 2nd ACM symposium on Information, computer and communications security, pp. 273-283.

[11] D. Naccache (2005), *Secure and practical identity-based encryption,* Cryptology ePrint Archive, Report 2005/369.

[12] D. Pointcheval and O. Sanders (2016), *Short randomizable signatures*, In Topics in Cryptology - CT-RSA 2016 -The Cryptographers' Track at the RSA Conference.

[13] A. Shamir, *Identity-based cryptosystems and signature schemes*, In G. R. Blakley and D. Chaum, editors, Advances in Cryptology - CRYPTO'84, pp.47-53.

[14] R. Tso, X. Yi, and X. Huang (2008), *Efficient and short certificateless signature*, In M. K. Franklin, L. C. K. Hui, and D. S. Wong, editors, CANS 08, pp.64-79.

[15] B. R. Waters (2005), *Efficient identity-based encryption without random oracles*, In R. Cramer, editor, Advances in Cryptology - EUROCRYPT 2005.

[16] Q. Xia, C. Xu, and Y. Yu (2010), *Key replacement attack on two certificateless signature schemes without random oracles*, Key Eng. Mater.

[17] H. Xiong, Z. Qin, and F. Li (2008), *An improved certificateless signature scheme secure in the standard model*, Fundamenta Informaticae, vol.88, pp.193-206.

[18] Y. Yu, Y. Mu, G. Wang, Q. Xia, and B. Yang (2012), *Improved certificateless signature scheme provably secure in the standard model*, IET Inf. Secur, vol.6, issue 2, June 2012.

[19] Y. Yuan, D. Li, L. Tian, and H. Zhu (2009), *Certificateless signature scheme without random oracles*. Proc. ISA, LNCS 5576, pp.31-40.

[20] D. H. Yum and P. J. Lee (2004), *Generic construction of certificateless signature*. In H. Wang, J. Pieprzyk, and V. Varadharajan, editors, ACISP 04, pp.200-211.

[21] Z. Zhang, D. S. Wong, J. Xu, and D. Feng (2006), *Certificateless public-key signature: Security model and ecffient construction*.ACNS 06, pp.293-308.

MULTICAST ROUTING HEURISTIC ALGORITHMS IN NON-SPLITTING WDM NETWORKS

Le Dinh Danh

Abstract: *Multicast at core WDM layer is known as the efficient way of communications to perform data transmission from a source to several destinations. However, due to costly and complicated fabrication of multicast capable switches, multicasting still partly leverages non-splitting devices like TaC cross-connects. This paper investigates multicasting in such context with the objective of minimizing the cost of using wavelengths in network links. Without splitters, a set of light-spiders starting from the multicast source covering all the destinations is known as the traditional solution. This paper argues that the exact solution for the problem is a set of non-elementary spiders called light-spider hierarchies. Two efficient heuristic algorithms are proposed to compute the light-spider hierarchies to illustrate our findings.*

Keywords: *WDM networks, multicast routing, heuristics.*

1. Introduction

Among the optical constraints, the availability of light splitters in the switches is often the most difficult one due to many reasons. First, splitters are expensive and complicated in fabrication. Besides, splitting causes significant power loss. In the ideal case, the power loss is inversely proportional to the number of split signals at the outgoing ports [1]. Also, wavelength converters are still immature. Therefore, we assume neither splitters nor wavelength converters available in this study. Fortunately, multicasting in WDM networks without splitters and wavelength converters is still feasible with the help of Tap-and-Continue (TaC) cross-connects proposed in [2].

In fact, multicasting in non-splitting WDM networks without wavelength converters have been studied in several works [2 -5]. These works were based on either light-paths [3, 4], light-trails [2], or light-forest [5]. However, there is lack of a deep investigation on the best light-structures for the problem as well as efficient algorithms to find them. In addition, all of the above previous works assume the same set of wavelengths available in all the network links, which is not practical. Regarding the optimization objective, these works aimed at minimizing the network resources taking both the number of wavelengths and the wavelength cost into account, with more focus on the number of wavelengths. In practical routing,

Le Dinh Danh

Faculty of Information and Communication Technologies, Hong Duc University

Email: Ledinhdanh@hdu.edu.vn (✉)

however, the wavelengths are occupied and released dynamically, leading to arbitrary wavelengths available in each link at a certain time. In such cases, minimizing the total number of links used is more important than the total number of wavelengths.

This paper aims at filling the gaps in literature works for routing in non-splitting WDM networks. Specifically, first, a general case with arbitrary wavelength distribution is investigated. Second, total link cost is focused instead of number of wavelengths. Third, two heuristic algorithms are proposed. Finally and most importantly, the exact route structure is identified for the problem. Numerous simulations are conducted to support our announced findings. The rest of this chapter is organized as follows. Section 2 defines the problem and related metrics. Section 3 analyses the exact light-structures for the problem. Section 4 presents two heuristic algorithms, followed by their evaluation described in Section 5. Section 6 concludes the paper.

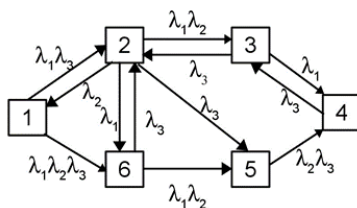## 2. Minimum Cost Multicast (MCM) Problem

Figure 1. A WDM network

A WDM network topology is given by a directed graph $G = (V,A)$, wherein V represents a set of nodes which are all equipped with TaC cross-connects, and A represents a set of directed fibers (links). We assume that there are at most two fibers between every node pair, and each fiber has an arbitrary set of spare wavelengths. Let W be the set of all the possible wavelengths in the network. Since the number of wavelengths can be different in the fibers, we denote $w(l)$ the set of available wavelengths in fiber link $l \in A$: $w(l) \subseteq W$, $\forall\, l \in A$. Also, each fiber l is associated with a positive number $c(l)$ representing the cost of using a wavelength on that fiber (suppose that $c(l)$ is the same for every wavelength in fiber l). Fig. 1 illustrates an example of a WDM network with different distribution of wavelengths in the fibers.

Given a multicast request denoted by $r = (s, D)$, the problem consists in finding a multicast route F starting at the source that spans the destinations D and targeting a given objective function. Without loss of generality, suppose that F consists of K light-structures T_i, $i = 1,...,K$, each using a wavelength. The number of wavelengths needed to accommodate the multicast request r is equal to K, i.e., $numwl(F) = K$. The cost of F is the summation of the costs of all the light-structures T_i:

$$\text{cost}(F) = \sum_{i=1}^{K} \text{cost}(T_i) = \sum_{i=1}^{K} \sum_{l \in T_i} c(l)$$

The problem aims at minimizing the combined total cost function expressed as:

$$TotalCost(F) = \Delta * cost(F) + numwl(F) = \Delta * \sum_{i=1}^{K} \sum_{l \in T_i} c(l) + K, \, \Delta > W$$

By choosing $\Delta > W$, the problem aims at minimizing total wavelength link cost first, followed by number of wavelengths.

The multicast route F must comply several constraints. Since there is no wavelength converter, a wavelength should be retained on all the links along a light-structure (*wavelength continuity constraint*), and the light-structures sharing a common link must use different wavelengths (*distinct wavelength constraint*) [7]. Besides, since there is no light splitter, every node (except the multicast source[1]) used in any light-structure should have a degree bounded by two. It is called the *degree constraint.*

3. Exact solutions

Conventionally, the minimum cost multicast route corresponds to tree structure, since there is no redundant edge (arc) created. In non-splitting case, to guarantee this degree constraint, the solution should become a spider-like structure (a spider is a tree with at most one branch vertex [7]). Thus the solution for multicasting without splitters is conventionally a set of light-spiders. However, optical cross-connects allow light signals to be switched using input/output port pairs using a same wavelength as long as no collision occurs. In other words, nodes can be traversed more than once by a route using a wavelength. This makes it possible to realize *non-elementary* routes, as illustrated in Figure 2. Accordingly, three solutions for the request $r=(s,\{d_1,d_2\})$ on the same network condition are possible. Assume that every link is undirected and has unity cost (cost=1). Among possible solutions, light-spider (Fig. 2a) is an *elementary* route; whereas a set of light-paths (Fig. 2b) and a light-trail (Fig. 2c) which are examples of *non-elementary* routes. Obviously, in this context, non-elementary routes are preferred for the cost optimal solution than that of elementary one (light-spider). In the remainder of the paper, we call the mentioned non-elementary routes *light-spider hierarchy*, to distinguish them from elementary light-spider. With this in mind, Theorem 1 gives exact solutions for MCM problem.
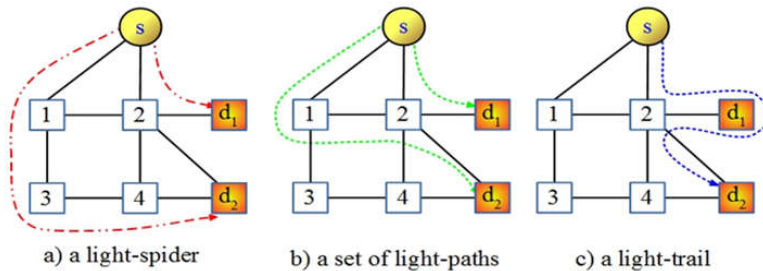

Figure 2. *Different solutions for the multicast request r=(s,{d1,d2})*

Theorem 1. The exact solutions for MCM problem is a set of light-spider-hierarchies.

In the next two sections, two heuristic algorithms to compute the approximate solutions for the MCM problem are presented and evaluated.

---

[1] *Because optical networking allows nodes to be equipped with multiple transmitters, so the multicast source can inject the same wavelength to arbitrary number of successors.*

4. Heuristic algorithms

In this section, we propose two efficient heuristic algorithms for MCM problem.

4.1. Notations

The two proposed heuristic algorithms work on layered graph model [8] instead of topology graph. To support the description of the two heuristic algorithms, we define some used notations as follows.

$G'=(V',A')$: the layered graph constructed from the topology graph $G=(V,A)$.

$r'=(s',D')$: the corresponding request of the original request $r=(s,D)$ created in the layered graph. We call s' the *source*, and $d' \in D$*'s ink* in short.

MC_SET: the set of copies of the original source s in all the layers.

$CONN\_SET$: the set of connectors, which can be used to grow the current hierarchy H. For the aforementioned degree constraint, not all the vertices in H but a subset of them can be used to grow the hierarchy. They include the s', copies of the original source s, MC_SET and leaf-nodes in H.

$SPT(c,D')$: the shortest path tree from source c to set D'.

$P(u,v)$: the shortest path from u to v.

$pred(d')$: the predecessor of sink $d' \in D'$ in the shortest path from s' to a sink d'.

4.2. Nearest Destination First Algorithm

Nearest Destination First (NDF) algorithm employs the basic idea of the Minimum Path Heuristic [6], which constructs an approximate Steiner tree from an initial vertex by iteratively adding a destination together with the shortest path (one at a time) until all the destinations reached. However, to satisfy the aforementioned degree constraint, MPH is modified in NDF heuristic to compute a valid route.

Given a WDM network modeled by a topology graph $G=(V,A)$, and a multicast request $r=(s,D),$ NDF computes a minimum cost route for the corresponding request $r'=(s',D')$ on layered graph $G'=(V',A')$. The algorithm returns a multicast route (*hierarchy*) H rooted at the source s' and spans the *sinks* D' = {d'$_1$,d'$_2$,.., d'$_D$}. After pruning pseudo vertices and arcs from H, the resulting hierarchy H consists of a set of light-spider-hierarchies (LSHs). Each of these LSHs is located in a different layer, using a distinct wavelength. The description of NDF is given in the Algorithm 1.

Initially, H consists of only the source s'. At each iteration, the algorithm searches for the nearest sink d' (line 11) from $CONN\_SET$ in the current hierarchy H to all the *unreached* sinks $d' \in D'$. This is done by gathering set $CONN\_SET$ as a virtual source c, and then creating a shortest path tree from c to the sinks in D' (line 7). Then the algorithm adds all vertices and arcs in the path $P(c, pred(d'))$ to H, then removes the arcs in the path $P(c,d')$ from the layered graph G', and update $CONN\_SET$ (lines 15-18). The algorithm terminates when there is no reachable destination remaining, or equivalently, H cannot be extended. To obtain the final multicast route, the final step prunes all the pseudo vertices (source and sinks) and the relevant pseudo arcs. The result is a set of LSHs routed at the source duplicates. Obviously, the

resulting hierarchy respects all the aforementioned constraint. One example to illustrate the algorithm is shown in Figure 4.

4.3. Critical Destination First Algorithm

NDF algorithm always chooses the nearest sink to extend the current hierarchy. However, there are cases in which this policy is not effective. Let us see Fig.4 for an example. The network is shown in Figure 4a, with the request $r=(s, \{d_1, d_2, d_3\}$. The corresponding layered graph with attached link costs are shown in Figure 4b. According to NDF, the first sink should be d'_3 with the shortest path computed in layer 1: $(s',s^1,2^1,4^1,5^1,d^1_3,d'_3)$ with length (cost) of 4. For the next iteration, only d'_1 can be reached (through layer 2) with the corresponding shortest path $(s',s^2,1^2,4^2,6^2,d^2_1,d'_1)$ with length of 8. The algorithm terminates and d'_2 is not routed (Fig.4c)!.

Now we see that d'_2 has a least number of incoming arcs (1 in this case). Naturally, it should be chosen first since it has the least probability to be routed. Suppose that we choose d'_2 first, the corresponding shortest path is $(s', s^1, 2^1, 4^1, 5^1, d^1_2, d'_2)$ with the length of 5 is added to the hierarchy. To choose the next sink between d'_1 and d'_3, since they have the same number of incoming links, the nearest one from the current hierarchy should be chosen.

So the next sink should be d'_3, and the corresponding shortest path $(d^1_2,5^1,d^1_3,d'_3)$ with the length of 3. Finally, the last sink d'_1 and the shortest path $(s', s^2, 1^2, 4^2, 6^2, d^2_1, d'_1)$ with the length of 8 is added to the hierarchy, resulting in the solution that reaches all the sinks with total cost of 16 as shown in Figure 4d.

Algorithm 1 Nearest Destination First Algorithm

Input: A topology graph $G = (V,A)$, a set of wavelengths W, a multicast request $r = (s,D)$
Output: A minimum cost hierarchy H
1: Construct the layered graph $G' = (V',A')$ from G, and the multicast request $r' = (s',D')$ from r
2: $MC\_SET \leftarrow \{s^1\} \cup \{s^2\} \cup ... \cup \{s^{|W|}\}$
3: $CONN\_SET \leftarrow \{s'\} \cup MC\_SET$
4: $H \leftarrow \{s'\}$
5: **while** $(D' \neq \emptyset)$ **do**
6:      Gather set CONN_SET as a virtual source c
7:      Compute in G' the shortest path tree $SPT(c,D')$
8:      **if** $(SPT(c,D') = \emptyset)$ **then**
9:          **break**
10:      **end if**
11:      Find the nearest sink d' from c
12:      $H \leftarrow H \cup P(c, pred(d'))$
13:      $D' \leftarrow D' \setminus \{d'\}$
14:      $A' \leftarrow A' \setminus \{$arcs in $P(c,d')\}$
15:      $CONN\_SET \leftarrow CONN\_SET \cup \{pred(d')\}$
16:      **if** $(c \notin MC\_SET)$ **then**
17:          $CONN\_SET \leftarrow CONN\_SET \setminus \{c\}$
18:      **end if**
19: **end while**
20: Prune all the pseudo vertices and relevant pseudo arcs from H
21: **return** H

From the above observation, it is more beneficial to give higher priority to the sinks with lower incoming degree when extending the current hierarchy. We call these sinks *critical destinations*, and the incoming degree *critical degree*, since the incoming degree of a sink indicates the reachability of it from the source *s'* (Fig.4b). The least critical degree sink is thus the most critical destination. This gives rise to the new policy, i.e., choosing the most critical destination first, and hence the name: Critical Destination First (CDF) heuristic. When there are multiple sinks having the same critical degree, the nearest one from the current hierarchy will be chosen first as in NDF.

Basically, CDF has the same framework as NDF, except that instead of finding a nearest sink of *D'*, CDF finds the most critical sink from *D'*. This difference leads to two other different points in the description of CDF algorithm. The first point comes from the possibility that the shortest path *P(c,pred(d'))* may contain destination duplicates which are associated with some sinks. If so, the corresponding sinks must be removed from *D'*. The second different point is that the algorithm should update the reachability of all the affected sinks whenever *P(c,pred(d'))* has been added. These points are dealt using efficient technique in implementation in such a way that the complexity of CDF is the same order as NDF. For space limit, however, the description of CDF and all technical details are omitted in this paper.
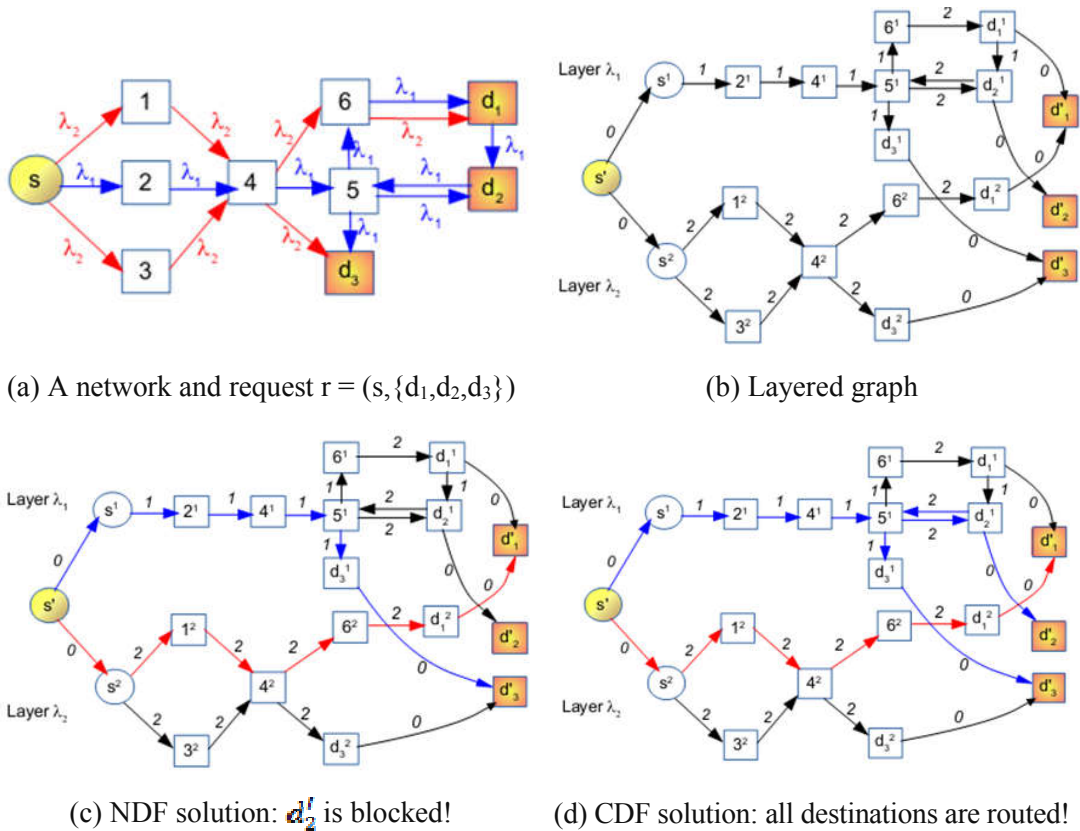

(a) A network and request r = (s,{d₁,d₂,d₃}) (b) Layered graph

(c) NDF solution: d_2^1 is blocked! (d) CDF solution: all destinations are routed!

Figure 4. *Illustration of the two heuristics*

5. Performance evaluation

5.1. Performance metrics

This work considers the case with arbitrary distribution of the wavelengths in the links. Hence, in the cases with limited available wavelengths, it is possible that not all the destinations routed for a given multicast request. Two blocking models are taken into account: *full destination blocking* and *partial destination blocking* [9]. Accordingly, under full destination blocking model, a multicast request is established if the source can reach to all the destinations. In this case, the appropriate metric to evaluate the solutions is the request blocking probability (RBP), i.e., the ratio of the number of requests blocked to the total number of requests arrived. For full destination blocking model, the destination blocking probability (DBP), i.e., the ratio between the destinations blocked and the total number of destinations of the request is calculated.

5.2. Simulation settings

The simulations are run on random network topologies $G = (V, A)$, with random distribution of wavelengths in each arc. $|V|$ is chosen in (50,100,150), $W = 10$, and $|D|$ varies in (10%, 20%; …, 90%) of $|V|$. For each $|D|$, we run 1000 instances, then calculate the 95% confident intervals for all the mean values of the above-defined blocking probability metrics (DBP and RBP).

5.3. Results and discussion

For space limit, only result for the case with $|V|=100$ is displayed in Figure 5, but the tendency is the same for the other cases. Among the algorithms, CDF-LSH outperforms the others when always achieving lowest DBP as well as RBP. NDF-LSH appears close to CDF-LSH on DBP but it is by far higher on RBP. Comparing LSH with LS solutions over all the conducted simulations, LSHs are always better than LSs whatever heuristics are employed. In particular, with NDF algorithm, NDF-LSH profits 4.5% (on average) lower on DBP, and 18% on RBP compared with NDF-LS. Similarly, the corresponding gains of 6.5% and 21.5% obtained when comparing CDF-LSH with CDF-LS. Especially, based on the same LSH solutions, CDF-LSH works better than NDF-LSH when achieving 18% lower RBP, 1% lower DBP.
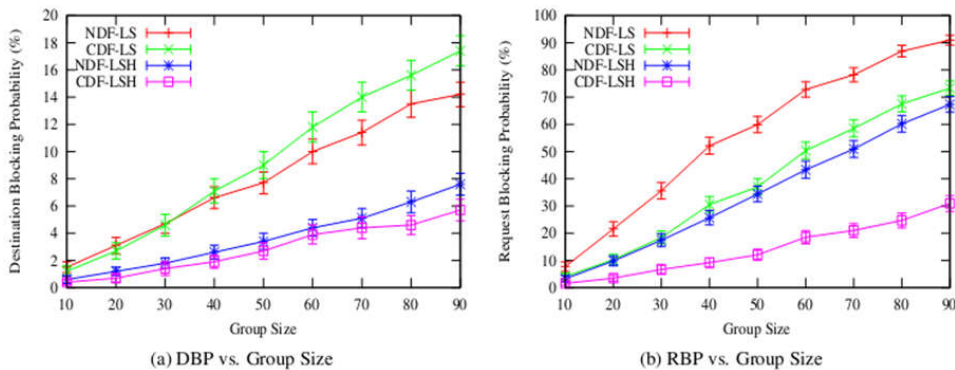

Figure 5. *Performances of algorithms on 100-node random graphs with W= 10*

In short, the LSH solutions are always better than LS counterparts; and the CDF algorithm outperforms NDF. The results are expected and explainable. On one hand, by permitting vertices to be visited more than once, LSH allows to make full use of all the available wavelengths in the links while respecting the three aforementioned constraints. Consequently, more destinations can be reached with a limited available links and wavelengths, it in turn results in better blocking probability. On the other hand, CDF gives high priority to the most critical destinations to extend the hierarchy. Naturally, the most critical destinations will not be abandoned whenever there is a chance. Meanwhile NDF always chooses the nearest one, which may leave some destinations unreached even if there are many other choices.

6. Conclusion

The paper proposed two cost-effective heuristics for the MCM problem: Nearest Destination First and Critical Destination First. These algorithms aim at minimizing the total cost for a given multicast request under the arbitrary availability of wavelengths in non-splitting networks. The two algorithms are designed to compute minimum-cost light-spider hierarchies based on the auxiliary layered graph model. They are different in the way of choosing the candidate destinations. NDF always chooses the nearest destinations at each iteration, while CDF selects the critical destinations first. The performances of the two heuristics are compared with each other. They show that, taking the critical degree of the destinations into account, particularly choosing the most critical destination to route first, results in a better solution under arbitrary wavelength configuration. Once again, the simulation results confirm that light-spider-hierarchies outperform light-spiders counterpart in supporting multicast in non-splitting networks.

References

[1]   M. Ali and J. S. Deogun (2000), *Power-efficient design of multicast wavelength-routed networks*, Selected Areas in Communications, IEEE Journal on, vol. 18, no. 10, pp. 1852 -1862.

[2]   M. Ali and J. S. Deogun (2000), *Cost-effective implementation of multicasting in wavelength-routed networks*, EEE/OSA Journal of Lightwave Technology, vol. 18, pp. 1628 -1638.

[3]   R. Libeskind-Hadas (2000), *Efficient collective communication in WDM networks with a power budget*, in Computer Communications and Networks, 2000. Proceedings. 9th International Conference on, pp. 612 -616.

[4]   S. Yan and J. Deogun (2003), *Multi-drop path model for multicast routing and wavelength assignment*, Information Sciences, vol. 149, no. 1, pp. 113 -134.

[5]   D.-R. Din (2009), *Heuristic Algorithms for Finding Light-Forest of Multicast Routing on WDM Network*, Information Science and Engineering, vol. 25, pp. 83 -103.

[6]   H. Takahashi and A. Matsuyama (1980), *An approximate solution for the Steiner problem in graphs*, Mathematica Japonica, vol. 24, pp. 573 -577.

[7]   L. Gargano, P. Hell, L. Stacho, and U. Vaccaro (2002), *Spanning trees with bounded number of branch vertices*, in Automata, Languages and Programming, pp. 355 -365, Springer.

[8]   C. Chen and S. Banerjee (1996), *A new model for optimal routing and wavelength assignment in wavelength division multiplexed optical networks*, in INFOCOM '96. Fifteenth Annual Joint Conference of the IEEE Computer Societies. Networking the Next Generation. Proceedings IEEE, vol. 1, pp. 164 -171, March 1996.

[9]   Dinh Danh Le, Fen Zhou, and Miklos Molnar (2015), *Minimizing Blocking Probability for MCRWA problem in WDM Networks: Exact Solutions and Heuristic Algorithms*, Journal of Optical Communications and Networking (JOCN). Vol. 7, Iss. 1, pp. 36-48.

A NETWORKED RENDERING PARADIGM FOR REMOTE RENDERING

Nguyen Thanh Dong, Le Dieu Linh

Abstract: *Advances in 3D graphics make it possible to generate highly realistic 3D models which usually contain a huge number of polygons. This large number of polygons gives rise to many challenges with respect to real-time rendering performance, storage requirements, and the transmission of graphics dataset over the network. In this paper, a networked rendering paradigm based on our pipeline-splitting method is introduced to facilitate the remote rendering system. Experimental results show that our method can reduce memory cost and computational workload for the client compared to that of client-side method.*

Keywords: *Remote rendering, cloud computing, networked graphics.*

1. Overview

As 3D models are becoming more realistic, it is challenging to render such models in real time due to the limited resources on mobile devices. As a result, there is a need to make use of client/server architecture in order to offload graphics rendering workload to the remote server leaving only minor tasks on the client-side. In general, methods related to the rendering of 3D graphics in the network environment can be roughly divided into three major categories: *client-side method, server-side method, and hybrid method*.

Client-side method:

In this method, the client is fully responsible for rendering the entire 3D models and the server simply sends graphics data to the client. A conventional way of client-side rendering is to transmit graphics commands to the client to be processed at the client [1, 2]. This method can reduce workload at the server, but it increases the processing demand on the client. This is suited for small applications but is insufficient for applications that require high rendering power. Moreover, graphics data to be transmitted to the client may be large leading to a long downloading time. To make it possible for the transfer of large models, the server performs the simplification and conversion to calculate a progressive representation composed of a

Nguyen Thanh Dong

Faculty of Information and Communication Technologies, Hong Duc University

Email: Nguyenthanhdong@hdu.edu.vn (✉)

Le Dieu Linh

Department of Information System, Hong Duc University

Email: Ledieulinh1504@gmail.com (✉)

simplified model and a series of refinements that the client will progressively download and display [3-5].

Server-side method:

In contrast to the client-side method, this method involves the server as completely responsible for graphics processing. The server renders the 3D scenes and transmits the rendered images to the client to be displayed [6-8]. This is highly beneficial to thin clients which often lack specialized hardware and are memory-limited [9-11]. However, the limitation of this method is that the server may become congested when serving a large number of clients and an appropriate network connection needs to exist. This maybe fine for fixed type networks but not appropriate for wireless networks. In addition, the latency due to the constant transmission of rendered images from the server to client may cause a reduction of interactivity. This is also costly in terms of network bandwidth. Image based rendering (IBR) techniques can be implemented in the client to improve frame rates and to deal with the transmission delay [12, 13]. However, there are some tradeoffs between the image quality and transmission latency [8].

Hybrid method:

In this method, both the client and server get involved in the rendering process. Rendering tasks are partially accomplished at the server and the remainder is performed at the client. The rendering workload can be shared between the server and client [14, 15]. However, deciding which parts to be performed at the client and which parts to be performed at the server is not an easy task. Noguera, et al., [14] proposed a technique to split the rendering workload between the server and the client based on the view volume. The client is responsible for rendering the terrain which is close to the viewer and the server renders the terrain far away from the viewer. Diepstraten, et al., [16], in a different manner, split up the image generation in order to balance workload between the client and the server. The server partially renders the 3D scene and sends 2D primitives to be processed on the client. However, this may lead to the downgrading of image quality since the client has to rely on feature lines abstracted from 3D models to draw the image.

In this paper, we introduce a new networked paradigm for remote rendering. A novel method to split the rendering pipeline is proposed aiming to break the rendering workload from the point that geometry processing is performed at the server, leaving the remaining parts to be done at the client. Different from conventional pipeline-splitting approaches, our approach relies on transform feedback mode[1] to obtain data from the buffer object in the graphics card, hence achieve hardware acceleration for geometry processing. Various 3D models have been experimented with our framework, the experimental results shown that our method can minimize memory cost and computational workload at the client and the processing time at the server.

---

[1] *http://www.opengl.org/registry/specs/NV/transform_feedback.txt*

2. Rendering pipeline analysis

In general, a rendering pipeline typically consists of a number of stages including vertex processing, geometry processing, rasterization, and fragment processing. For the sake of simplicity, we consider the pipeline with only two separated stages. The first stage named geometry processing is responsible for vertex transformations, lighting calculations, and triangle assembly. The second stage named rasterization is a combination of clipping/culling, rasterization, and fragment processing.
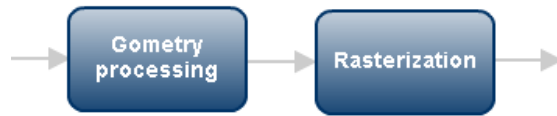

Figure 1. The analytical rendering pipeline

From this perspective, we present an analysis of the rendering pipeline in terms of processing time. It is worth noting that the determination of the most time-consuming stage in the graphics rendering pipeline is challenging as each stage depends on various factors. For example, the processing time at the geometry processing stage depends on the number of primitives while the processing time at rasterization stage depends on the number of input primitives, the viewing angle, and the image resolution.

Let T_p be the processing time of the entire pipeline, and T_g be the processing time of geometry processing stage. The total execution time T_p is equal to the sum of the execution times for the two stages: geometry processing and rasterization. T_g can be roughly estimated by disabling rasterization stage to prevent primitives from being rasterized. Note that we do not take into account the time taken to clear and swap the buffer during the rendering for the sake of simplicity.
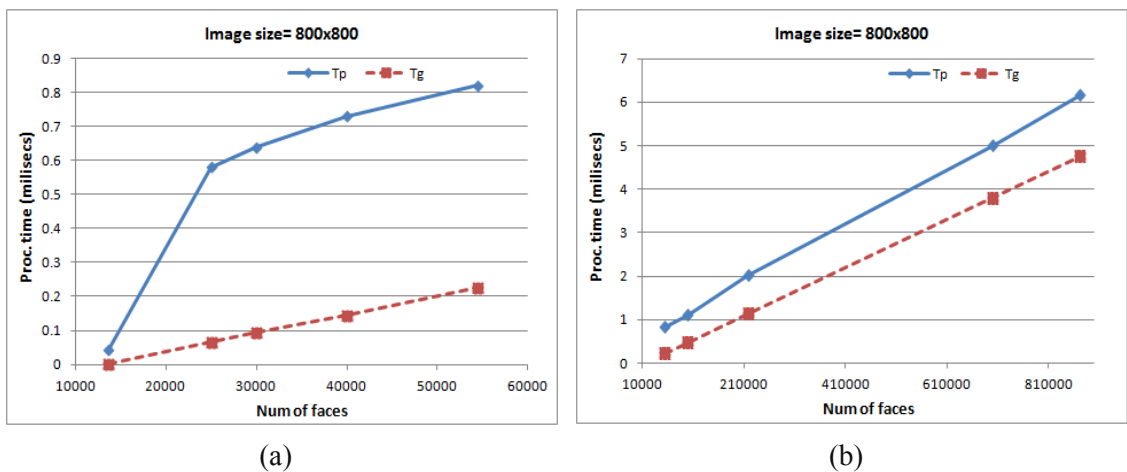

(a) (b)

Figure 2. Processing time at geometry processing stage compared to the rendering time in case of dragon model- graphics card: NVIDIA GeForce 9500GT (a) the number of faces is less than 100k (b) the number of faces ranging from 100k to 1M

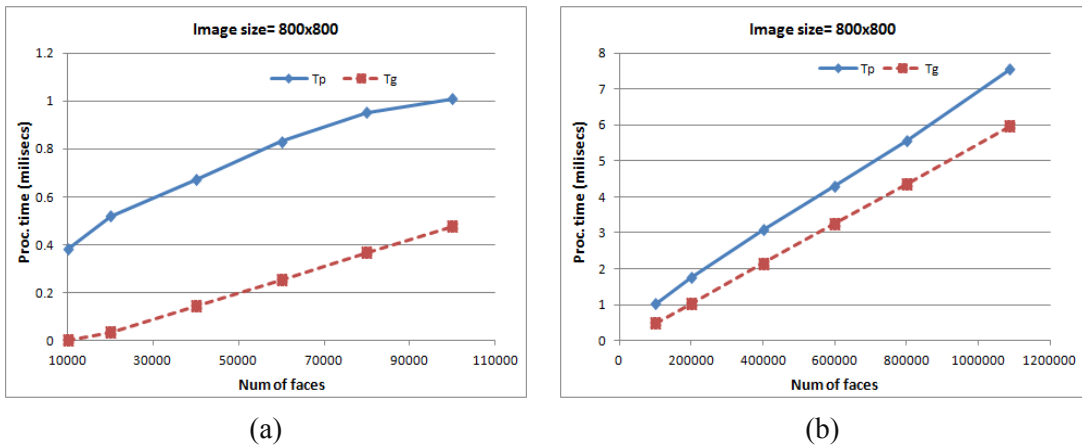(a)   (b)

Figure 3. *Processing time at geometry processing stage compared to the rendering time in case of happy model- graphics card: NVIDIA GeForce 9500GT (a) the number of faces is less than 100k (b) the number of faces ranging from 100k to 1M*
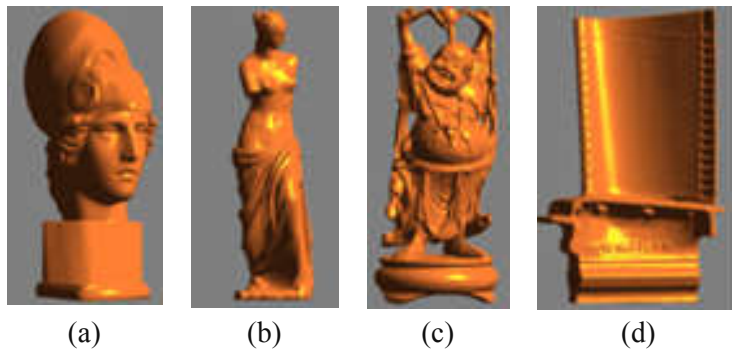

(a)   (b)   (c)   (d)

Figure 4. *3D models are used in the test*

We consider the impact of the image resolution and the number of primitives to the processing time at geometry processing stage and the rendering time of the entire pipeline. Figure 3, 4, 5 demonstrate some experimental results obtained from the test. This shows that for complex 3D models and small image size, tremendous amount of time is spent at geometry processing stage. Therefore, it is desirable to offload geometry processing stage to a dedicated server, and the rasterization is handled at the client. This can balance the rendering workload between the client and the server to some extent.

3. Networked rendering framework

In this section, we describe a scheme for remote rendering based on our pipeline-splitting method. At first, we present a paradigm for a networked rendering pipeline that extends the traditional rendering pipeline to include network transmission of geometry data. The rendering pipeline is divided in a way that some stages of it are offloaded to the remote server and the remainders remain at the client.
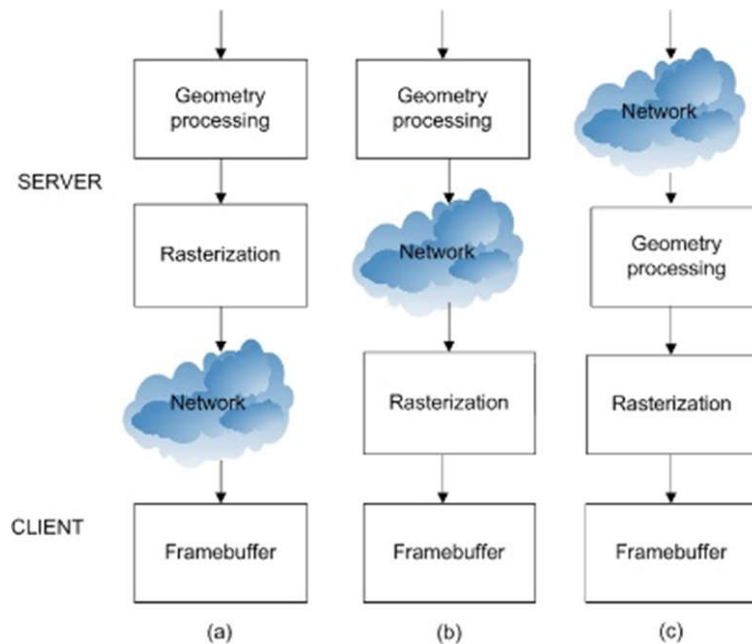
Figure 5. *Different architectures of networked rendering pipeline, (a) the entire pipeline is placed on server, (b) geometry is placed on server, rasterization is on client, (c) the entire pipeline is placed on client*

Pipeline splitting

Typically, the rendering pipeline resides on a single machine. It is difficult to achieve pipeline splitting due to the tight coupling of geometry and rasterization stage. Williams et al. [17, 18] proposed a method to separate the geometry stage and rasterization stage by adding two extensions to OpenGL library: triangle-feedback and triangle-rasterize. The triangle-feedback function passes all primitives through the geometric portion without rasterizing them and the triangle-rasterize function takes the data from geometric portion then put it into rasterization stage. To achieve hardware acceleration for rasterization, a vertex program is implemented to pass primitives into the hardware rasterizer on the graphics card. Graphics hardware acceleration, however, remains uncompleted for geometry processing. Banerjee, et al., [19, 20] combined Mesa3D[2] and socket networking code together to build RMesa which can split up the rendering pipeline into sub stages. The client can offload some stages in the pipeline to the remote server to be processed and then get the result back. Unfortunately, the approach offers no graphics hardware-acceleration for both geometry processing and rasterization. In our research, we split the rendering pipeline based on transform feedback mode. The use of transform feedback makes it possible to capture vertex attributes of the primitives processed by geometry processing stage. Vertex attributes are selected to store in a buffer, or several buffers separately which can be retrieved sometime later. The rest of pipeline can be discarded by disabling rasterization stage to prevent primitives from being rasterized. This way uncouples geometry processing stage from rasterization stage. The

---

[2] http://www.mesa3d.org/

transformed primitives copied from transform feedback buffer then can be rasterized in a different machine by simply put it back to the buffer without passing any transformation parameters. It is worth noting that the entire process happens inside the pipeline, therefore an advantage of our method is that it supports hardware-acceleration to both geometry processing and rasterization stage.
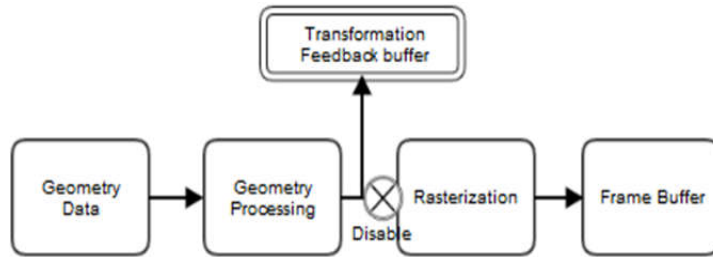

Figure 6. Transform feedback operation-vertices are transformed and stored in the transform feedback buffer object which can be obtained in the middle

Remote rendering based on pipeline-splitting method

In this section, we introduce a remote rendering framework making use of pipeline-splitting method that we have presented earlier. The basic concept is similar to image-based rendering, the major difference is that the sever sends back transformed primitives instead of rendered images to the client.
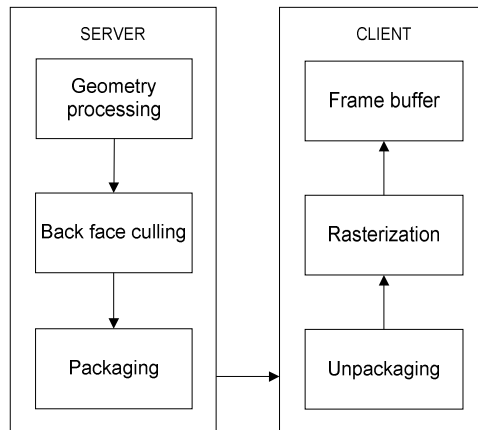
Figure 7. Client-server architecture for the proposed framework

Table 1. Notation 1

Symbols	Quantity
F	List of faces constructed the mesh
F_c	The remaining faces after culling
M, N	The number of faces stored in F and F_c respectively
CHUNK	Number of faces stored in a packet
p	Number of packets to be sent to the client

In our proposed framework, the server performs geometry processing on demand according to the viewing parameters received from the client. The back-face culling method then is employed to cull invisible primitives from transformed ones. The remaining primitives then are packaged to be sent to the client for rasterization.

To deal with restrictions in network performance and bandwidth, we take into account the network protocol for the data transmission. For the sake of transmission efficiency, it is important that UDP is employed for data transmission and TCP is used for exchanging messages and commands. To further reduce the latency, graphics content is packetized or can be compressed prior to the transmission. A chunk of primitives is grouped in a packet to be sent to the client for further processing. The number of packets to be sent for the rendering of a frame can be calculated as follows:

$p = \lceil M/CHUNK \rceil = \lceil \alpha N/CHUNK \rceil$ where $\alpha = M/N$ is culling ratio $(0 < \alpha \leq 1)$.

Transmission latency

Supposed that the time taken to transmit a packet to the client is t_p. t_p depends on network capacity (bw) and the size of packet (s_p): $t_p = s_p/bw$.

Let T be the transmission time of all primitives after performing back-face culling. This is equivalent to the transmission of p packets:

$$T = p \times t_p = \lceil \alpha N/CHUNK \rceil \times (s_p/bw)$$

It can be seen that the transmission latency is linearly proportional to the number of faces (N).

***Table 2.** Time to transmit a packet*

CHUNK	t_p (secs)	
	10 Mbps	100 Mbps
600	0.03456	0.003456
300	0.01728	0.0017728
200	0.01152	0.001152
100	0.00576	0.000576

***Table 3.** A theoretical estimation of the time it takes to transmit 3D models with different level of details (CHUNK=600)*

N	P	T (secs)	
		10 Mbps	100 Mbps
10000	17	0.58752	0.058752
20000	34	1.17504	0.117504
40000	67	2.31552	0.231552

60000	100	3.456	0.3456
80000	134	4.63104	0.463104
100000	167	5.77152	0.577152

4. Experimentation

We have implemented a remote rendering system on Windows in C++ using OpenGL making use of the proposed pipeline-splitting method to split the rendering workload between the server and client. The server we used in the test is Intel ® Core ™ i7 CPU, 3.24 GB of RAM, with NVIDIA GeForce 9500. A DELL T6600, Intel® Core™ 2 Duo CPU 2.2 GHz, 2G RAM is used as a client.

Processing time in the pipeline

We make a comparison between local rendering and our method in terms of processing time in the rendering pipeline at the client. As the number of faces being processed at the client has been reduced and geometry processing has been carried out at the remote server, our method can reduce the processing time at the client.

Table 4. *A comparison between our proposed method and local rendering in terms of processing time*

Model	Num of verts	Num of faces	Local rendering (secs)	Our method (secs)
Beethoven	2521	5030	0.0042	0.0027
Car	5247	10474	0.0072	0.0048
Ateneam	7546	15014	0.0100	0.0060
Dragon	10006	20000	0.0170	0.0080
Venus	19847	43357	0.0320	0.0180
Bunny	34834	69451	0.0486	0.0276

We compare our method with server-side rendering in terms of processing time at the server. In case of server-side rendering, we measure the processing time of the entire pipeline plus the time taken to copy data from the frame buffer to CPU. For our method, we measure the processing time at geometry processing stage and the time to copy data from the transform feedback buffer. When the number of primitives to be processed is small and the image size is large, the processing time at the server is significantly reduced in our method compared to that of server-side rendering. Note that when the fragment processing is relatively cheap, the transform feedback could end up being a major bottleneck leading to more processing time at the server in our method compared to that of server-side rendering.
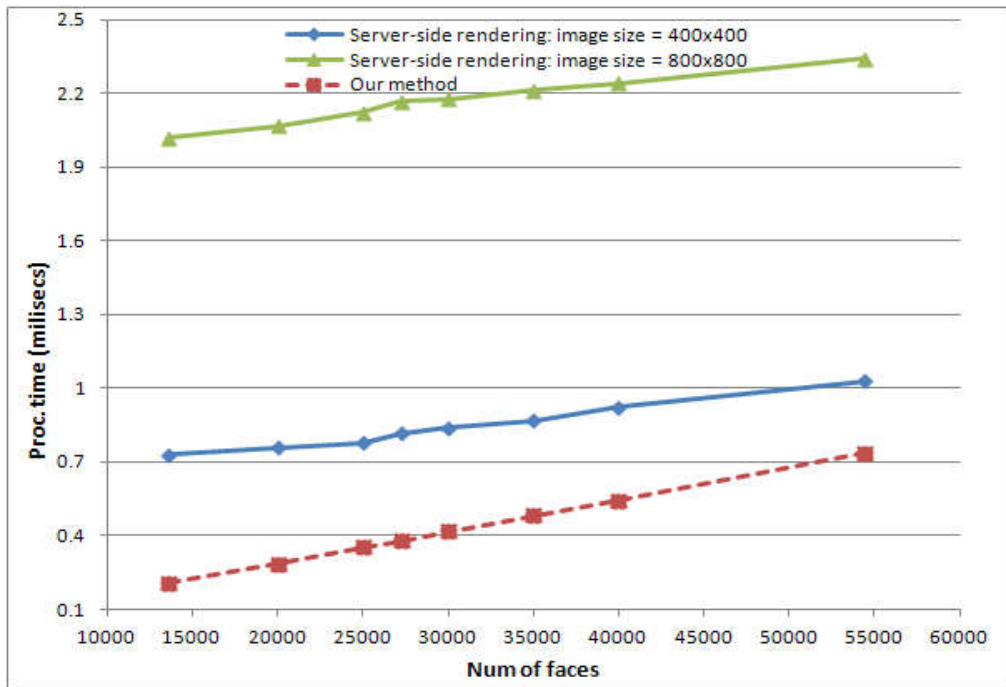
Figure 8. *A comparison between server-side rendering and our method in terms of processing time tested with dragon model*
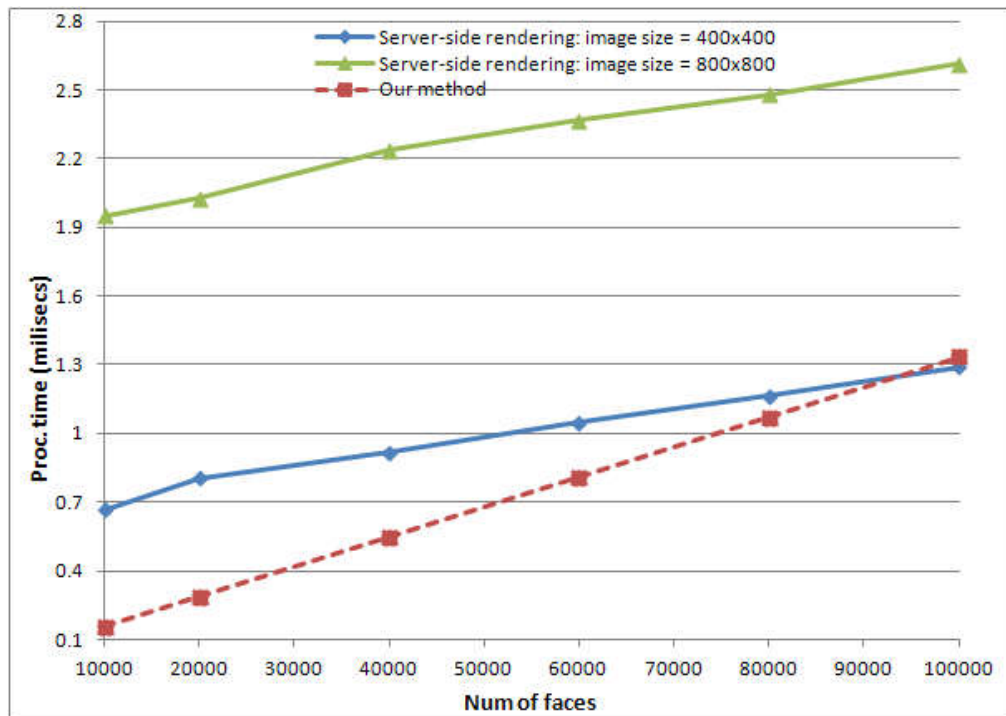

Figure 9. *A comparison between server-side rendering and our method in terms of processing time tested with happy model*

Storage requirements

After back-face culling[3] is performed at the server, only visible faces are sent to clients for further processing. Therefore, the amount of faces to be handled at the client is significantly reduced. As can be seen in the Figure below, about 40-50% of the faces are actually processed at the client. As such, our method would be of great benefits to thin clients since they are limited in their storage capacity.
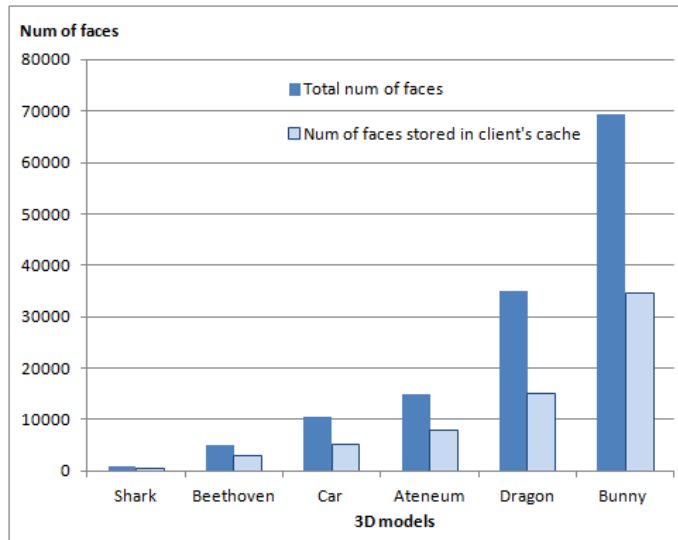

Figure 10. *Average number of faces processed at the client*

Network communication

The data transfer capability is considered a major bottleneck in the remote rendering. Network communication for the proposed framework is built on TCP/IP sockets. We employ UDP for the transmission of graphics datasets and TCP for sending commands from client to server and vice versa. We have previously presented a theoretical analysis of transmission latency in previous section. Therefore, this experiment is also able to verify the theoretical analysis of our proposed framework. Our test is conducted in both a 10Mbps and 100Mbps Ethernet connections. To further reduce the transmission latency, we can make use of a compression/decompression technique. However, it is worth noting that the process of compression/decompression may introduce some delays to the system.

Table 5. *Transmission latency measured in different network connections*

Model	Num of faces	Latency (seconds)	
		10 Mbps	100 Mbps
Shark	734	0.0380	0.0043
Apple	1704	0.0750	0.0084

---

[3] https://en.wikipedia.org/wiki/Back-face_culling

Ant	912	0.0380	0.0044
Beethoven	5030	0.1778	0.0199
Car	10474	0.3432	0.0337
Ateneam	15014	0.3840	0.0469
Big dodge	16646	0.5261	0.0543
Dragon 1	20000	0.6247	0.0641
Dragon 2	35000	1.0741	0.1117
Venus	43357	1.2881	0.1359
Bunny	69451	2.1737	0.2124

5. Conclusion

In this paper, we have investigated the graphics rendering pipeline in terms of processing time. We have proposed a networked rendering paradigm based on our pipeline-splitting method to facilitate remote rendering. It is shown that our method can reduce memory cost and computational workload at the client compared to that of client-side rendering and processing time at the server compared to that of server-side rendering. The work also can be applied to distributed-rendering as we can distribute geometry processing and rasterization to be handled on different machines in the cloud. It is worth noting that our framework can work with pretty large 3D models, however, there must be a limit since the residual list is linearly proportional to the number of faces of the 3D model.

References

[1]   G. Jung and S. Jung (2006), *A Streaming Engine for PC-Based 3D Network Games onto Heterogeneous Mobile Platforms*, in Technologies for E-Learning and Digital Entertainment. vol. 3942, Z. Pan, R. Aylett, H. Diener, X. Jin, S. Göbel, and L. Li, Eds., ed: Springer Berlin / Heidelberg, pp. 797-800.

[2]   A. Mohr and M. Gleicher (2002), *HijackGL: reconstructing from streams for stylized rendering*, presented at the Proceedings of the 2nd international symposium on Non-photorealistic animation and rendering, Annecy, France, pp.13-ff.

[3]   G. Hesina and D. Schmalstieg (1998), *A Network Architecture for Remote Rendering*, presented at the Proceedings of the Second International Workshop on Distributed Interactive Simulation and Real-Time Applications, pp.88.

[4]   M. Isenburg and P. Lindstrom (2005), *Streaming meshes*, in Visualization, 2005. VIS 05. IEEE, 2005, pp. 231-238.

[5]   H. T. Vo, S. P. Callahan, P. Lindstrom, V. Pascucci, and C. T. Silva (2007), *Streaming Simplification of Tetrahedral Meshes*, Visualization and Computer Graphics, IEEE Transactions on, vol. 13, pp. 145-155.

[6]   X. Liu, H. Sun, and E. Wu (2000), *A hybrid method of image synthesis in IBR for novel viewpoints*, presented at the Proceedings of the ACM symposium on Virtual reality software and technology, Seoul, Korea.

[7]   Z. J. Y. Lei, D. Chen, and H. Bao (2004), *Image-Based Walkthrough over Internet on Mobile Devices*, in Proc. GCC Workshops, pp. 728-735.

[8]   Y. a. C.-O. Mann, D. (1997), *Selective Pixel Transmission for Navigating in Remote Virtual Environments,* Eurographics '97, Volume 16, Number 3.

[9]   A. Boukerche, T. Huang, and R. W. N. Pazzi (2005), *A real-time transport protocol for image-based rendering over heterogeneous wireless networks*, presented at the Proceedings of the 8th ACM international symposium on Modeling, analysis and simulation of wireless and mobile systems, Montral, Quebec, Canada.

[10]   A. Boukerche, F. Jing, and R. B. de Araujo (2006), *A 3D image-based rendering technique for mobile handheld devices*, in World of Wireless, Mobile and Multimedia Networks, International Symposium, pp. 7 pp.-331.

[11]   F. Lamberti and A. Sanna (2007), *A Streaming-Based Solution for Remote Visualization of 3D Graphics on Mobile Devices*, Visualization and Computer Graphics, IEEE Transactions on, vol. 13, pp. 247-260.

[12]   P. Bao and D. Gourlay (2003), *Low bandwidth remote rendering using 3D image warping*, in Visual Information Engineering, 2003. VIE 2003. International Conference on, 2003, pp. 61-64.

[13]   P. Bao and D. Gourlay (2006), *A framework for remote rendering of 3-D scenes on limited mobile devices*, Multimedia, IEEE Transactions on, vol. 8, pp. 382-389.

[14]   J. M. Noguera, R. J. Segura, C. J. Ogáyar, and R. Joan-Arinyo (2011), *Navigating large terrains using commodity mobile devices*, Computers & Geosciences, vol. 37, pp. 1218-1233, 2011.

[15]   M. Levoy (1995), *Polygon-assisted JPEG and MPEG compression of synthetic images*, presented at the Proceedings of the 22nd annual conference on Computer graphics and interactive techniques.

[16]   J. Diepstraten, M. Gorke, and T. Ertl (2004), *Remote Line Rendering for Mobile Devices*, presented at the Proceedings of the Computer Graphics International.

[17]   J. L. Williams and R. E. Hiromoto (2005), *Sort-middle multi-projector immediate-mode rendering in Chromium*, in Visualization. VIS 05. IEEE, 2005, pp. 103-110.

[18]   J. L. Williams and R. E. Hiromoto (2003), *A proposal for a sort-middle cluster rendering system*, in Intelligent Data Acquisition and Advanced Computing Systems: Technology and Applications, 2003. Proceedings of the Second IEEE International Workshop on, 2003, pp. 36-38.

[19]   K. S. Banerjee and E. Agu (2005), *Remote execution for 3D graphics on mobile devices*, in Wireless Networks, Communications and Mobile Computing, International Conference on, 2005, pp. 1154-1159 vol.2.

[20]   E. Agu, B. Kutty, N. Shirish, O. Rekutin, and D. Kramer (2005), *A middleware architecture for mobile 3D graphics*, in Distributed Computing Systems Workshops. 25th IEEE International Conference on, 2005, pp. 617-623.

COMPUTER SIMULATION FOR FINDING NONCLASSICAL PROPERTIES IN KERR NONLINEAR COUPLER WITH NONLINEAR EXCHANGE

Nguyen Thi Dung

Abstract: *In this paper, we present the techniques of simulation modelling for quantum dynamics of Kerr nonlinear coupler system which consists of two nonlinear quantum oscillators mutually coupled by continuous nonlinear interaction. We show that by using evolution operator formalism we can model the quantum system and derive the "exact" solution for finding the existence of nonclassical properties in terms of squeezing, antibunching, intermodal entanglement and their higher order counterparts under the effect of dissipation process.*

1. Introduction

Over last decades, there exists a rapid development of a particular interest in research of quantum correlations in multi-parties systems consisting of two or more subsystems. Such correlations are the significant problem from both the physical viewpoints and applications in quantum information theory [2,3,6,23]. These signature of nonclassicalities are related to different quantum features as squeezing, higher order squeezing, antibunching, higher order antibunching, intermodal entanglement, and higher-order entanglement. Squeezing can be defined in terms of the quadrature variance of a component, and used for the performance of continuous variable quantum information processing [6]. Antibunching can be defined by correlation function at zero delay. This phenomenon is used to build a high-quality single photon sources [23] and applied to perform quantum communication and quantum computation [6]. Entanglement plays an important role in implementation quantum cryptography, quantum teleportation, quantum key distribution [1,6,23]. Generation of those correlations in physical systems becomes one of the most important points. Therefore, finding physical models allowing for generating such states seems to be especially substantial. This paper aims to show how it is possible to

Nguyen Thi Dung

Faculty of Natural Sciences, Hong Duc University

Email: Nguyenthidung@hdu.edu.vn (✉)

generate non-classicalities by using techniques of simulation modeling for quantum dynamics of Kerr-like nonlinear coupler system under effect of damping process. Quantum Kerr-like nonlinearity models are widely discussed in numerous applications. For instance, they are considered as a source of non-Gaussian motional states of trapped ions [21], and are discussed in a context of the Bell's inequality violations [19]. Such models can also be applied in description of nanomechanical resonators and various optomechanical systems [20], Bose-Einstein condensates [18]. Thus, the modes of nonlinear directional coupler proved to be a promising device, easy treatment for finding numerical solutions and generating nonclassical effects and hence its quantumness.

2. The model description and simulation method

The considered system consists of two nonlinear Kerr-like oscillators mutually coupled by nonlinear interaction, where each oscillator corresponds to a single mode of the field labeled a and b [11] with not only the self-coupling term exits [12] but also so-called cross-Kerr coupling is taken into account [10,15]. The Hamiltonian comprising all above- terms which describes the dynamics of the our system can be written as (assuming $\hbar = 1$):

$$\hat{H} = \hat{H}_{free} + \hat{H}_{nl} + \hat{H}_{int} \tag{1}$$

Where

$$\hat{H}_{free} = \omega_a \hat{a}^\dagger \hat{a} + \omega_b \hat{b}^\dagger \hat{b} \tag{2}$$

is free renormalized Hamiltonian,

$$\hat{H}_{nl} = \frac{\chi_a}{2} \hat{a}^{\dagger 2} \hat{a}^2 + \frac{\chi_b}{2} \hat{b}^{\dagger 2} \hat{b}^2 + \tilde{\chi} \hat{a}^\dagger \hat{a} \hat{b}^\dagger \hat{b} \tag{3}$$

describes Kerr-like media (involving cross-Kerr coupling), and

$$\hat{H}_{int} = \varepsilon \hat{a}^{\dagger 2} \hat{b}^2 + \varepsilon^* \hat{b}^{\dagger 2} \hat{a}^2 \tag{4}$$

corresponds to the nonlinear interaction between two modes of the field.

The parameters $\chi_a (\chi_b)$ are proportional to the third-order susceptibility, $\tilde{\chi}$ describes the cross-action process, whereas ε means the strength of the nonlinear interaction. Since Hamiltonian system is expressed in term of bosonic creation and annihilation operators, we can present them as square matrices, for example of mode a:

$$\hat{a}^\dagger = \begin{bmatrix} 0 & 0 & 0 & ... & 0 & 0 \\ 1 & 0 & 0 & ... & 0 & 0 \\ 0 & \sqrt{2} & 0 & ... & 0 & 0 \\ \vdots & \vdots & \vdots & \ddots & \vdots & ... \\ 0 & 0 & 0 & ...\sqrt{n-1} & 0 \end{bmatrix} \tag{5}$$

$$\hat{a} = \begin{bmatrix} 0 & 1 & 0 & ... & 0 & 0 \\ 0 & 0 & \sqrt{2} & ... & 0 & 0 \\ \vdots & \vdots & \vdots & \ddots & \vdots & ... \\ 0 & 0 & 0 & ... & 0 & \sqrt{n-1} \\ 0 & 0 & 0 & ... & 0 & 0 \end{bmatrix}. \tag{6}$$

The creation (annihilation) operator $\hat{b}^\dagger \left(\hat{b} \right)$ for mode b can be also constructed by the same way. Assuming that the field was initially in the Glauber coherent states for the both modes as:

$$\left| \psi(0) \right\rangle = \left| \alpha \right\rangle \otimes \left| \beta \right\rangle \tag{7}$$

Obviously, it is possible to construct those coherent states in Fock basis as:

$$\left| \alpha \right\rangle = \mathrm{e}^{-\frac{|\alpha|^2}{2}} \sum_{n_a=0}^{\infty} \frac{\alpha^{n_a}}{\sqrt{n_a!}} \left| n_a \right\rangle; \qquad \left| \beta \right\rangle = \mathrm{e}^{-\frac{|\beta|^2}{2}} \sum_{n_b=0}^{\infty} \frac{\beta^{n_b}}{\sqrt{n_b!}} \left| n_b \right\rangle \tag{8}$$

where α and β are equal to the mean number of photon by the following relation $\left\langle \hat{n}_a \right\rangle = \left\langle \hat{a}^\dagger \hat{a} \right\rangle = |\alpha|^2$ and $\left\langle \hat{n}_b \right\rangle = \left\langle \hat{b}^\dagger \hat{b} \right\rangle = |\beta|^2$. In consequence, we can easily express these states in the matrix presentation.

The aim of our consideration is to check how interaction with external bath can influence on nonclassical properties generation.

When the system is influenced by external bath, time-evolution of our system is described by the density matrix, which is a solution of the master equation, within the standard Markov approximation [4] as:

$$\frac{d\hat{\rho}}{dt} = -i\left(\hat{H}\hat{\rho} - \hat{\rho}\hat{H} \right) + \hat{L}_{loss}^{(a)}\hat{\rho} + \hat{L}_{loss}^{(b)}\hat{\rho}, \tag{9}$$

where appearing here Liouvillian of two-mode density matrix $\hat{\rho}$ are given by

$$\hat{L}_{\mathrm{loss}}^{(a)}\hat{\rho} = \frac{\gamma_a}{2}\left(\left[\hat{a}\hat{\rho}, \hat{a}^\dagger \right] + \left[\hat{a}, \hat{\rho}\hat{a}^\dagger \right] \right) + \gamma_a \bar{n}_a \left[\left[\hat{a}, \hat{\rho} \right], \hat{a}^\dagger \right] \tag{10}$$

$$\hat{L}_{\mathrm{loss}}^{(b)}\hat{\rho} = \frac{\gamma_b}{2}\left(\left[\hat{b}\hat{\rho}, \hat{b}^\dagger \right] + \left[\hat{b}, \hat{\rho}\hat{b}^\dagger \right] \right) + \gamma_b \bar{n}_b \left[\left[\hat{b}, \hat{\rho} \right], \hat{b}^\dagger \right] \tag{11}$$

caused by amplitude damping [4]. The parameter $\gamma_i \left(i = a, b \right)$ is damping constants, whereas $\bar{n}_i \left(i = a, b \right)$ denotes the mean number of photon in thermal bath. Note that we have quiet "reservoirs" at zero temperature corresponding to the case $\bar{n}_a = \bar{n}_b = 0,$ and noisy "reservoirs" when the temperature is greater than zero corresponding to $\bar{n}_a, \ \bar{n}_b > 0$.

Thank to *quantum Monte Carlo*, it is possible to solve operator equation (9) by appropriate standard numerical simulation using calculation of matrix exponentials and

advantage of considering super operators. Matlab computing language [16] is a appropriate software for performing our purposes due to their simplicity and ease of use even for computer users who are not very experienced in numerical calculations.

3. The existence of nonclassical properties

3.1. Squeezing and higher-order squeezing effect

In order to investigate the single mode squeezing effect we define quadrature variances and principal squeezing variances [14,22] as:

$$\left\{ \begin{matrix} S_a \\ S_a^{'} \end{matrix} \right\} = \frac{1}{2}\left[\left\langle \Delta\hat{a}^{\dagger}\Delta\hat{a} \right\rangle \pm \mathrm{Re}\left\langle \left(\Delta\hat{a}^2 \right) \right\rangle \right] \tag{12}$$

$$\lambda_a = \frac{1}{2}\left[\left\langle \Delta\hat{a}^{\dagger}\Delta\hat{a} \right\rangle - \left| \left\langle \left(\Delta\hat{a}^2 \right) \right\rangle \right| \right] \tag{13}$$

where the fluctuation of operators are defined as

$$\left\langle \Delta\hat{X}\Delta\hat{Y} \right\rangle = \left\langle \hat{X}\hat{Y} \right\rangle - \left\langle \hat{X} \right\rangle\left\langle \hat{Y} \right\rangle \tag{14}$$

The expectation value can be calculated from density matrix as

$$\left\langle \hat{X} \right\rangle = \mathrm{Tr}\left(\hat{\rho}\hat{X} \right) \tag{15}$$

Two mode squeezing can be defined from two mode quadrature variances and principal squeezing as [9]:

$$\left\{ \begin{matrix} S_{ab} \\ S_{ab}^{'} \end{matrix} \right\} = 2\left[1 + \left\langle \Delta\hat{a}^{\dagger}\Delta\hat{a} \right\rangle + \left\langle \Delta\hat{b}^{\dagger}\Delta\hat{b} \right\rangle + 2\mathrm{Re}\left\langle \Delta\hat{a}^{\dagger}\Delta\hat{b} \right\rangle \pm \mathrm{Re}\left(\left\langle \left(\Delta\hat{a}^2 \right) \right\rangle + \left\langle \left(\Delta\hat{b}^2 \right) \right\rangle + 2\left\langle \Delta\hat{a}^{\dagger}\Delta\hat{b} \right\rangle \right) \right] \tag{16}$$

$$\lambda_{ab} = 2\left[1 + \left\langle \Delta\hat{a}^{\dagger}\Delta\hat{a} \right\rangle + \left\langle \Delta\hat{b}^{\dagger}\Delta\hat{b} \right\rangle + 2\mathrm{Re}\left\langle \Delta\hat{a}^{\dagger}\Delta\hat{b} \right\rangle + \left| \left\langle \left(\Delta\hat{a}^2 \right) \right\rangle + \left\langle \left(\Delta\hat{b}^2 \right) \right\rangle + 2\left\langle \Delta\hat{a}^{\dagger}\Delta\hat{b} \right\rangle \right| \right] \tag{17}$$

One mode squeezing can be detected when quadrature variances and principal squeezing go below zero [8] and two mode squeezing can be observed in a quantum system if the two mode quadrature variances and principal squeezing are smaller than 2 [9]. In the Fig.1 we show the time-evolution of the squeezing parameters $S_{a(b)}, S_{a(b)}^{'}$ and that of principal squeezing $\lambda_{a(b)}$ for single mode. For the chosen values of the parameters, squeezing cannot be created in $S_{a(b)}^{'}$ factors. Assuming that the amplitude of the initial coherent states α and β are real and equal to each other. Because of the equivalence, the lines for two modes are identical. From the behavior of squeezing factors and principle squeezing, we see that despite of effect of dissipation process, our system can give single mode squeezing in both modes a and b.
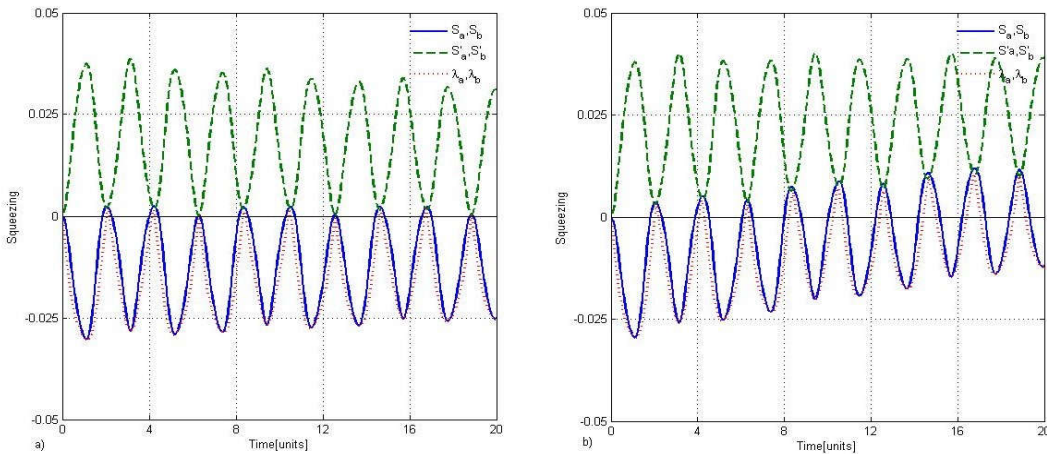
Figure 1. *Evolution of one mode squeezing factor when initial coherent states are*
$\alpha = 0.2,\ \beta = 0.2$ *, other parameters* $\chi_a/2 = \chi_b/2 = \tilde{\chi} = 1,\ \varepsilon = 0.5,\ \gamma = 0.001$*. We assume that*
$\overline{n}_a = \overline{n}_b = 0$ *in Figure a) and* $\overline{n}_a = \overline{n}_b = 0.1$ *in Figure b)*

In the Figure 2 two-mode quadrature variances S_{ab}, S'_{ab} and two-mode principle squeezing λ_{ab} are plotted. For the initial coherent states $\alpha=0.2$, $\beta=0.2$, we see that the quadrature S'_{ab} does not give any signature of squeezing, contrary to S_{ab} and λ_{ab} which appear with a quite high intensity. Additionally, with non-zero temperature bath, one and two-mode squeezing decay very slow in the time domain. Of course, when $\overline{n}_a = \overline{n}_b = 0.1$, squeezing effects degenerate faster than for non-zero temperature bath, we can conclude that our system is more sensitive with nonzero temperature bath.
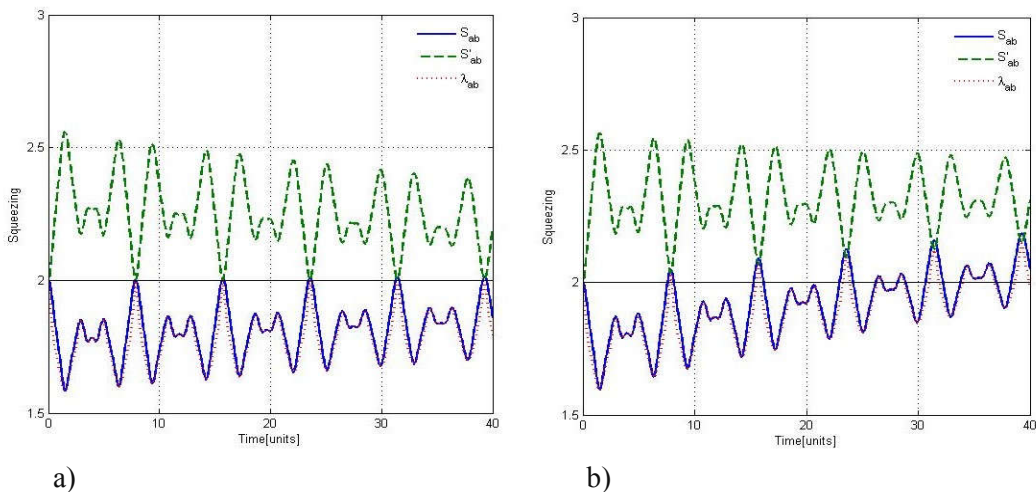

Figure 2. *The time-evolution of two-mode quadrature variances when initial coherent states*
are $\alpha = 0.2,\ \beta = 0.2$ *, other parameters* $\chi_a/2 = \chi_b/2 = 1;\ \tilde{\chi} = 1,\ \varepsilon = 0.5,\ \gamma = 0.001$*. We assume*
that $\overline{n}_a = \overline{n}_b = 0$ *in Figure a) and* $\overline{n}_a = \overline{n}_b = 0.1$*in Figure b)*

One-and two-mode squeezing are widely applied in the literatures. However, they can be treated as the lowest order nonclassicality indicators, whereas there appear other criteria which are can be applied to test *higher-order squeezing* effect. In our consideration, for convenience we use the definition given by Hillery [5], that provides witness for the existence of higher-order nonclassicality through the two amplitude powered quadrature variables defined with use of higher power of creation and annihilation operators as:

$$\hat{X}_{1,a} = \frac{\hat{a}^k + \hat{a}^{\dagger k}}{2}, \quad \hat{X}_{2,a} = i\frac{\hat{a}^{\dagger k} - \hat{a}^k}{2} \tag{18}$$

for the mode *a*, where *k* is a positive integer. Since two operators $\hat{X}$ and $\hat{Y}$ do not commute, from uncertainty relation, we can obtain a condition of higher-order squeezing:

$$\begin{Bmatrix} H_{1,a} \\ H_{2,a} \end{Bmatrix} = \left\langle \left(\Delta \hat{X}_{j,a}\right)^2 \right\rangle - \frac{1}{2}\left|\left\langle \hat{Z} \right\rangle\right| < 0, \tag{19}$$

where $j = \{1, 2\}$ and $\left[\hat{X}_{1,a}, \hat{X}_{2,a}\right] = i\hat{Z}$. Of course, we obtain similarly the condition of higher-order squeezing for mode b.

Time-evolution of $H_{1,a}\left(H_{1,b}\right)$ and $H_{2,a}\left(H_{2,b}\right)$ are plotted in Figure 3 to seek for the signal of higher order squeezing. From this figure, where negative parts of the plots depict signature of higher-order squeezing we can recognize that this nonclassical properties are present for the both: zero- and non-zero temperature bath. Of course, one can see that the effect of damping is more evident for the case depicted at the right-hand plots where the negative parts predominate.
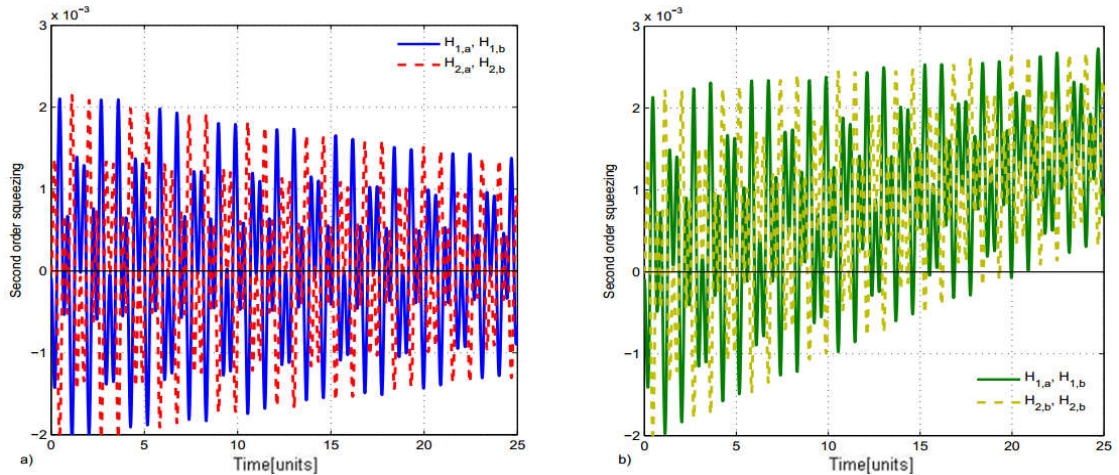

Figure 3. *The time-evolution of $H_{1,a}\left(H_{1,b}\right)$ (solid line), and $H_{2,a}\left(H_{2,b}\right)$ (dashed line) when initial coherent states are $\alpha = \beta = 0.2$, other parameters $\chi_a/2 = \chi_b/2 = 1$; $\tilde{\chi} = 1$, $\varepsilon = 0.5$, $\gamma = 0.001$. We assume that $\bar{n}_a = \bar{n}_b = 0$ in Figure a) and $\bar{n}_a = \bar{n}_b = 0.1$ in Figure b)*

3.2. Antibunching and higher-order antibunching

In quantum statistics, signatures of the single-mode case photon antibunching can be obtained in terms of the correlation function [15], later defined in terms of the creation and annihilation operators as:

$$D_a^2 = \left\langle \hat{a}^{\dagger 2} \hat{a}^2 \right\rangle - \left\langle \hat{a}^\dagger \hat{a} \right\rangle^2 < 0. \tag{20}$$

More general the criteria to investigate the higher-order antibunching of the pure modes was first introduced by C.T.Lee [13], and afterwards was simply expressed by Pathak and Garcia [17] as

$$D_a^k = \left\langle \hat{a}^{\dagger k} \hat{a}^k \right\rangle - \left\langle \hat{a}^\dagger \hat{a} \right\rangle^k < 0. \tag{21}$$

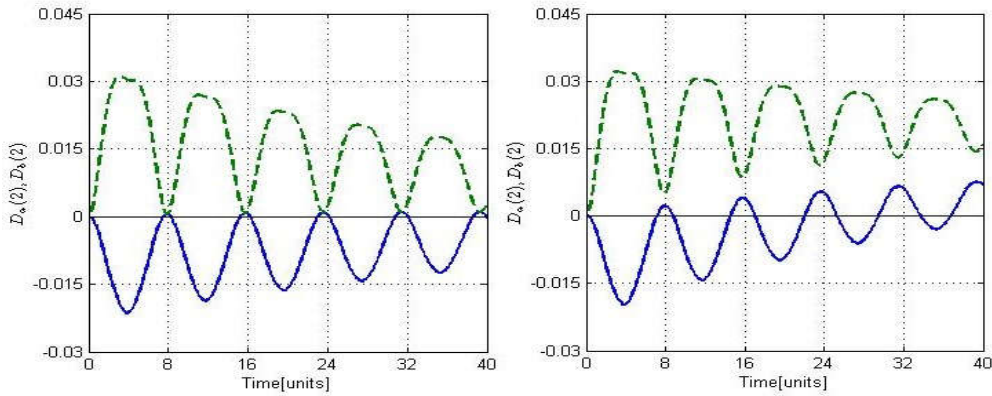When $k=2$ we return to the normal antibunching.

Figure 4. The time-evolution of $D_a(2)$ (solid line), and $D_b(2)$ (dashed line) when damping effects are assumed. The parameters are $\chi_a/2 = \chi_b/2 = 1$; $\tilde{\chi} = 1$, $\varepsilon = 0.5$, $\gamma = 0.001$, $\alpha = 0.2$, $\beta = 0.2$ $\bar{n}_a = \bar{n}_b = 0$ in Figure a) and $\bar{n}_a = \bar{n}_b = 0.1$ in Figure b)
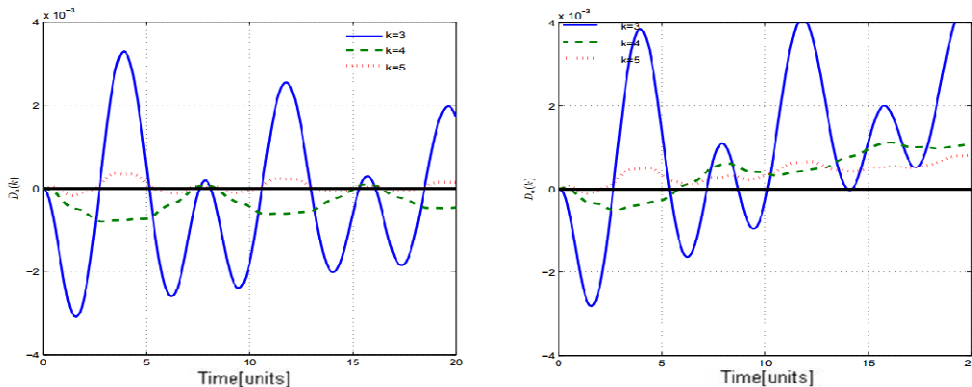

Figure 5. The time-evolution of $D_a(3)$ (solid line), and $D_b(4)$ for $k=4$ (dashed line) when damping effects are assumed. The parameters are the same as those for Figure 4

When the coherent single modes are equal ($\alpha=\beta$), there does not exist any signature of normal and higher-order antibunching. If two initial coherent states are not equal, these effects might be pronounced. The existence of the normal and higher order antibunching in our system are shown in the Figure 4 and the Figure 5. From two figures, we can not observe any normal- and higher-order antibunching in mode b when the value of β is smaller than that of α. It is easy to recognize that for our system, this nonclassical property is evident when the initial states are setting up with smaller values of mean number of photons. The figures also illustrate the influence of damping processes due to the degeneration of D_a factor. For the case of the non-zero temperature bath, this factor is decayed faster.

3.3. Intermodal entanglement

There exist several entanglement criteria which would be directly applicable for multimode problems expressed in terms of expectation values of field operators. Among them, Hillery-Zubairy (HZ) criteria I and II [2,7] have obtained more attention due to simple computation, experimental practicability and their recent success in observing entanglement in various physical system. The HZ-I criterion can be generally expressed in terms of the creation and annihilation operators in the following way [8]:

$$E_{ab}^{kl} = \left\langle \hat{a}^{\dagger k} \hat{a}^{k} \hat{b}^{\dagger l} \hat{b}^{l} \right\rangle - \left| \left\langle \hat{a}^{k} \hat{b}^{\dagger l} \right\rangle \right|^2 < 0 \qquad (23)$$

The HZ-II criterion, which is fulfilled for the separability states can be generalized for higher-order moments as [8]:

$$E_{ab}^{'kl} = \left\langle \hat{a}^{\dagger k} \hat{a}^{k} \right\rangle \left\langle \hat{b}^{\dagger l} \hat{b}^{l} \right\rangle - \left| \left\langle \hat{a}^{k} \hat{b}^{l} \right\rangle \right|^2 < 0 \qquad (24)$$

When one of these inequalities is fulfilled, the multimode system is entangled.
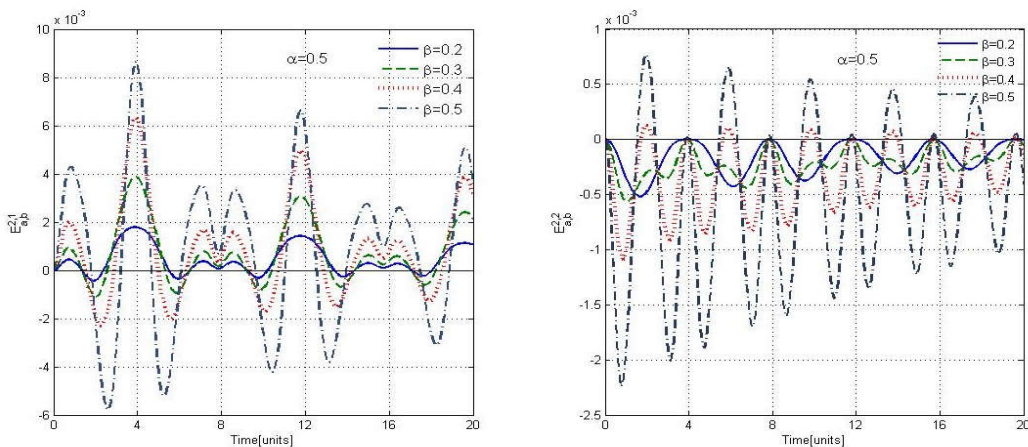

Figure 6. *The time evolution of $E_{ab}^{2,1}$ (a) and $E_{ab}^{2,2}$ (b) in the presence of damping effects. The parameters are $\chi_a/2 = \chi_b/2 = 1$; $\tilde{\chi} = 1.6$, $\varepsilon = 0.5$, $\gamma = 0.001$, $\bar{n}_a = \bar{n}_b = 0$. The initial coherent state is described by $\alpha = 0.5$, $\beta = 0.2$ (solid line), $\beta = 0.3$ (dashed line), $\beta = 0.4$ (dotted line), $\beta = 0.5$ (dash-dotted line)*
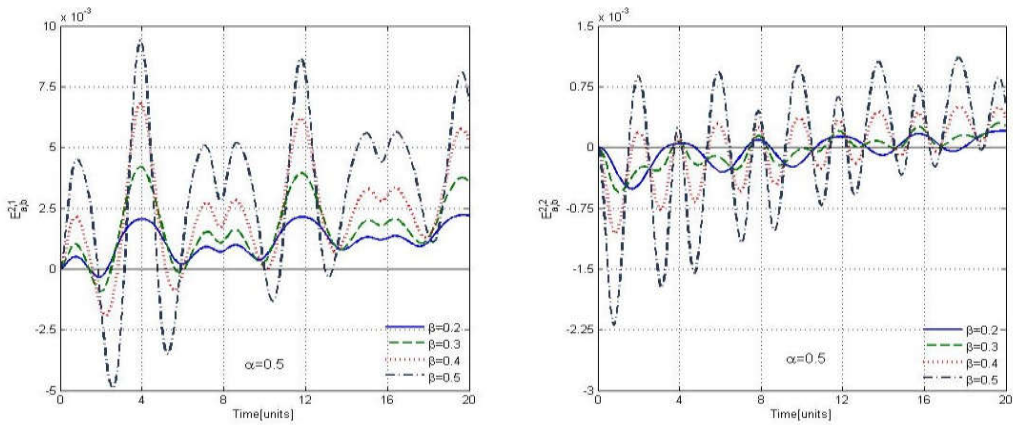
Figure 7. *The time evolution of $E_{ab}^{2,1}$ (a) and $E_{ab}^{2,2}$ (b) the same as Figure 6 but for $\bar{n}_a = \bar{n}_b = 0.1$*

The plots of factors showing the existence of intermodal entanglement in coupled-mode influenced by damping processes are shown in Figure 6 and Figure 7. The negative parts of the plots $E_{ab}^{2,1}$ and $E_{ab}^{2,2}$ show us that higher-order intermodal entanglement is present in our system. Also, we observe that the deeper minima appear for the greater values of the parameters α and β determining initial coherent states. For the case of the non-zero temperature bath, the deterioration of the entanglement is faster than of zero one. Furthermore, it is not possible to detect the signatures of lowest and higher intermodal entanglement by using (24) criterion. Therefore, one can say that our Kerr-like coupler system including nonlinear interaction term is sensitive for the interaction with environment, but still it can be seen as a source of intermodal entanglement and its higher orders.

4. Conclusions

Various types of nonclassical effects in the model of the nonlinear Kerr-coupler such as squeezing, antibunching, inter-mode entanglement and their higher order counterparts have been observed. Using unitary evolution operator formalism we simulated quantum dynamics of system and found numerically the "exact" solutions for these factors under damping effect. We showed that despite of interacting with environment, the parameters considered here can be an indicator of the generation such nonclassical effects and hence, quantumness of the system. Additionally, it was easy to recognize that under the effect of damping, those properties do not exist for some of parameters, but can be generated with small value of mean number of photons for the initial coherent states.

References

[1]   Bennett C H and Wiesner S J. (1992), *Phys. Rev.* Lett.69 2881-2884.

[2]   Duan L M, Giedke G, Cirac J I and Zoller P. (2000), *Phys. Rev.* Lett. 84 2722-2725.

[3]   Ekert A. (1991), *Phys. Rev.* Lett.67 661.

[4]   Gardiner C W, Zoller P. (2000), *Quantum Noise*. Springer-Verlag 3rd ed.

[5]   Hillery M. (1987), *Phys. Rev. A* 36 37968.

[6]   Hillery M. (2000), *Phys. Rev. A*61 022309.

[7]   Hillery M and Zubairy M S. (2006), *Phys. Rev. A* 74 032333.

[8]   Hillery M and Zubairy M S. (2006), *Phys. Rev. Lett.* 96 050503.

[9]   Karska M and Perina J. (1990), *J. Mod. Opt.* 37 195.

[10]   Kowalewska-Kudlaszyk A. (2013), Phys. Scr. T153 01403.

[11]   Korolkova N, Perina J. (1997), Opt. Commun. 136 135.

[12]   Kowalewska-Kudlaszyk A, Leonski W, Thi Nguyen D, Cao Long Van (2014), *Phys. Scr.* T160 014023.

[13]   Lee C T (1990), *Phys. Rev. A*. 41 1569; 1721.

[14]   Luks A, Perinova V and Perina J. (1988), *Opt. Commun.* 67 149-151.

[15]   Mandel L and Wolf E. (1995), *Optical Coherence and Quantum Optics*. Cambridge, New York.

[16]   Matlab documentation, available at: http://www.mathworks.com/help/matlab/index.html

[17]   Pathak A and Garcia M. (2006), *Applied Physics* B 84, 484.

[18]   Perinova V, Luks A, and Krapelka J. (2013), *J. Phys. B: At. Mol. Opt. Phys.*, 46 195301.

[19]   Stobinska M, Jeong H, and Ralph T C. (2007), *Phys. Rev. A*, 75 052105.

[20]   Stobinska M, Milburn G J, and Wodkiewicz K. (2008), *Phys. Rev. A*, 78 013810.

[21]   Stobinska M, Villar A S, and Leuchs G. (2011), *EPL (Europhysics Letters)*, 94(5) 54002.

[22]   Tanas R, Miranowicz A and Kielich S. (1991), *Phys. Rev. A* 43 4014.

[23]   Yuan Z, Kardynal B E, Stevenson R M, Shields A J, Lobo C J, Cooper K, Beattie N S, Ritchie D A and Pepper M. (2002), *Science* 295 102.

BISTABLE CHARACTERISTIC OF SIGNAL TRANSMITTED THROUGH THE SYMMETRIC NONLINEAR MICHELSON INTERFEROMETER

Nguyen Van Hoa

Abstract: *Symmetric Nonlinear Michelson Interferometer (SNMI) operating as optical bistable device has been theoretically investigated. The general output-input intensity relation is introduced for case the output signal transmitted through SNMI. The bistable characteristic (hysteresis) is calculated and presented for some cases the structural parameters were selected specifically.*

1. Introduction

Close Nonlinear Michelson Interferometer (CNMI) operating as optical bistable device has been studied in previous works [4, 6, 7]. In those works, we used CNMI as the splitter with transmission through coefficient T = 50%; 2 mirrors M_1, M_2 with reflection coefficient R_1 and R_2; Kerr nonlinear medium only half the space inside interferometer (limited by the splitter P, mirror M_4 and mirror M_2). The question is if nonlinear medium occupies the entire space inside CNMI (then CNMI becomes Symmetric Nonlinear Michelson Interferometer-SNMI) Does the signal transmitted by SNMI (go out from the mirror M_2) have bistable characteristic or not? This work will answer that question.
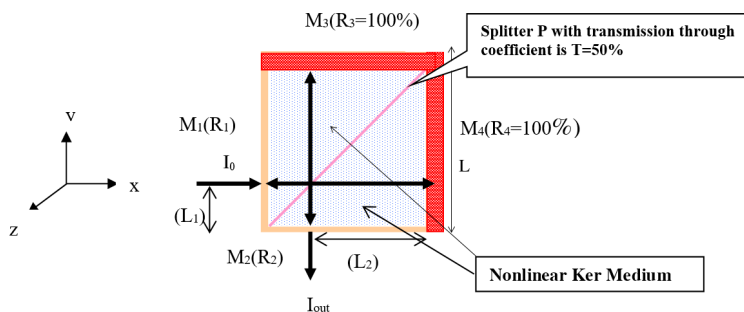

Figure 1. *Symmetric Nonlinear Michelson Interferometer*

Nguyen Van Hoa
Faculty of Engineering and Technology, Hong Duc University
Email: Nguyenvanhoa@hdu.edu.vn (✉)

2. Input-output equation of intensity

From the classical Michelson interferometer as in Fig.1 with two mirrors M_3, M_4 which have the reflection coefficient 100% and the splitter P with transmission coefficient ½ we added two mirrors M_1, M_2 to have the reflection coefficients, R_1, R_2 respectively; space between the four mirrors M_1, M_2, M_3 and M_4 is a nonlinear medium with absorption coefficient α and refractive index comply with Kerr optical effect $n = n_0 + n_2 I_{ctr}$, where n_0 is the linear refractivity index, n_2 is the nonlinear index coefficient, directly relating to third-order susceptibility $\chi^{(3)}$ (electrostatic unit) by the relation [2]: $n_2 = \dfrac{4\pi^2 R_e\left[\chi^{(3)}\right]}{cn_0}$ and $\mathbf{I_{ctr}}$ is the average intensity of light transmitted through nonlinear medium is called control intensity. Assume that light travels to mirror M_1 with equation $E_0 = A_0 e^{i(\omega t - \phi)}$ equivalent to the intensity of $I_0 = \dfrac{1}{2}\varepsilon_0 c E_0^2$, after passing through and go out SNMI from mirror M_2 the intensity will be:

$$I_{out} = \frac{\frac{1}{2}(1-R_1)(1-R_2)e^{-2\alpha L}I_0}{1-2^{\frac{1}{2}}\left(R_1^{\frac{1}{2}}+R_2^{\frac{1}{2}}\right)e^{-\alpha L}\cos\left\{\frac{4\pi n_2 L}{\lambda}\cdot\frac{(R_1+R_2)e^{-\frac{1}{2}\alpha L_1}}{\alpha L(1-R_2)}\left(1-e^{-\alpha L}\right)I_{out}+\delta_0\right\}+\frac{1}{2}\left[R_1^{\frac{1}{2}}+R_2^{\frac{1}{2}}\right]^2 e^{-2\alpha L}} \quad (1)$$

Here:

L_1 is the transmission distance of light in nonlinear medium from mirror M_1 to the split P.

L_2 is the transmission distance of light in nonlinear medium from the split P to mirror M_2.

$$L = L_1 + L_2$$

δ_0 is the phase shift of light caused by the mirror to be called the initial phase.

Easy to see that if $R_1=R_2=0$, $\alpha=0$ infer $\delta_0=0$, then $I_{out}=\dfrac{1}{2}I_0$ and SNMI becomes classical Michelson interferometer [1].

2.1. Influence of the reflection coefficient of the mirror M_1
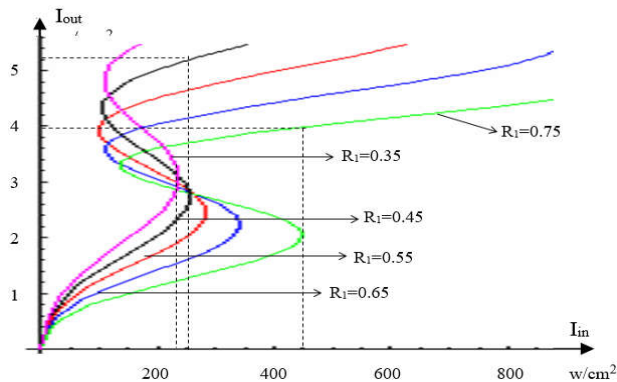

Figure 2. Out-input characteristics of SNMI with $\delta_0=-0.1\pi$; $L=1mm$; $\lambda=0.85\mu m$, $R_2=0.5$; $n_2=10^{-4}cm^2/w$ $L_1=L/3$; $\alpha=10^3$ and R_1 change with the values of $R_1 = 0.35, 0.45, 0.55, 0.65, 0.75$

By selecting the parameters:

L = 1mm; λ = 0.85μm, R_2 = 0.5; n_2 = 10^{-4} cm²/w; L_1 = L/3; α=10^3 and R_1 change with the values of R1 = 0.35, 0.45, 0.55, 0.65, 0.75 we obtain the graph of (1) shown in Figure 2. From the graph we see that the curves are S-shaped. This confirms SNMI operating as optical bistable device with control parameter I_{in} and separate parameter R_1. Input-output characteristic of SNMI reacts very sensitively to changes of R_1: with R_1 = 0.35, 0.45, 0.55, 0.65 and 0.75 have five "threshold jump" on the five curves respectively: 230, 250, 280, 340, 450 (w/cm²).

Thus, the value of "threshold jump" is proportional to the reflectivity R_1 of the mirror M_1. From the graph we also see, then the output intensity I_{out} decreases: if R_1=0.45, the "threshold jump" =250 w/cm² and I_{out}=5.2 w/cm² even if R_1=0.75, the "threshold jump" =450 w/cm² and $I_{out}{\approx}4$ w/cm². So the device to work effectively with the parameter δ_0=-0.1π; L=1mm; λ=0.85μm, R_2=0.45; n_2=10^{-4}cm²/w; L_1=L/3; α=10^3 is fixed we should choose the reflectivity of the mirror M_1 as small as possible. Thus reflectivity coefficients of the mirror M_1 has a strong influence to the bistable characteristic of input-output relations; in addition to generating feedback signal (one of two factors for bipolar stability) it was decided to set the value of "threshold jumps" and the height of the jump from that decision to the performance of the device. In addition to generating feedback signal (one of two factors for bipolar stability) it was decided to set the value of "threshold jumps" and the height of the jump from that decision to the performance of the device. With the parameters selected, the device working in optimal mode when R_1=0, then "jump threshold" is minimal and almost 220 w/cm², while the intensity of the signal reaches the maximum value I_{out} = 8.5w/cm² (Fig. 3) and performance of devices = 4%.
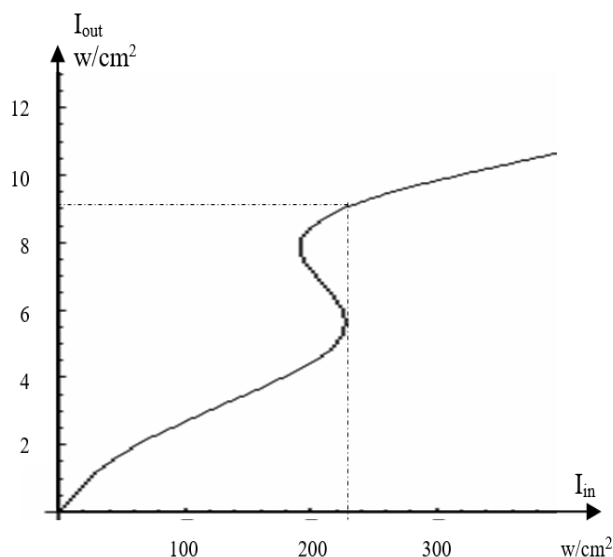

Figure 3. *Out-input characteristics of SNMI with δ_0 = -0.1π; L=1mm; λ = 0.85μm, R_2 = 0.5; n_2 = 10^{-4} cm²/w L_1=L/3; α=10^3 and R_1 = 0*

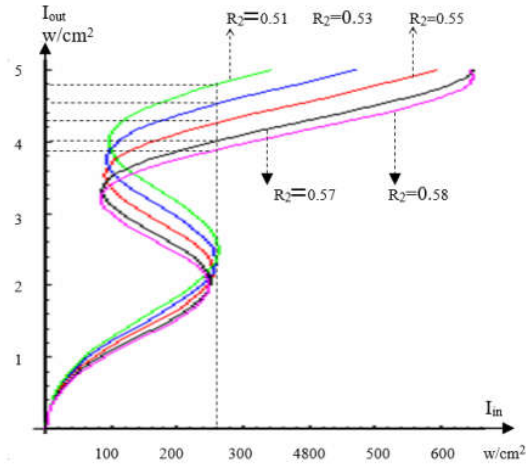## 2.2. Influence of the reflection coefficient of the mirror M_2

Figure 4. *Out-input characteristics of SNMI with δ_0=-0.1π; L=1mm; λ=0.85μm, R_1=0.5;*
n_2=$10^{-4}cm^2$/w; L_1=L/3; α=10^3 and R_2 change with the values of R_2 = 0.55, 0.53, 0.51, 0.57, 0.58

In the structure of SNMI, the role of mirror M_2 is generated feedback signal, so that the reflection coefficient of it has influence on bistable characteristics of SNMI. In Fig. 4 the bistable curves for the case of reflection coefficient of mirror M_2 changes, the parameters used in calculations are given in caption under the figure. We found that:

5 different values of R_2 which are very small (0.51, 0.53, 0.55, 0.57, 0.58) will have five bistable curve, but five "threshold jump" nearly equal ($I_{in} \approx 260w/cm^2$) corresponding to 5 different output values ($I_{out} \approx 4.8$, 4.6, 4.3, 4.0, 3.82 w/cm^2).

Thus, the influence of reflection coefficient of the mirror M_2 (R_2) to input-output relationship is not strong as reflection coefficient of mirror M_1 (R_1); It only works to adjust the output intensity. Output in tensity becomes stronger when the reflectivity of the mirror M_2 is smaller. As shown in Figure 5, when R_2=0 persists bistable effects but at the "threshold jumps" output intensity achieves a relatively large value I_{out}= 12.5w/cm^2.

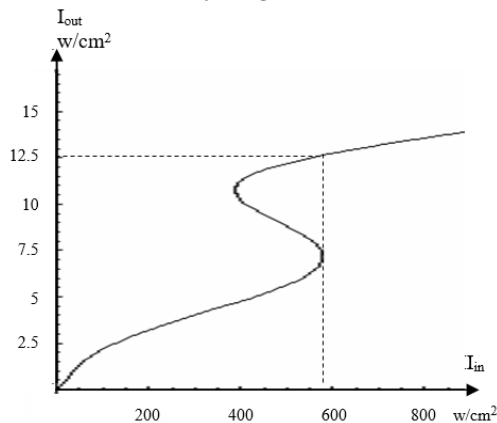**Figure 5.** *Out-input characteristics of SNMI with δ_0 = -0.1π; L=1mm; λ = 0.85μm; R_1 = 0.75;*
n_2 = $10^{-4}cm^2$/w; L_1 = L/3; α = 10^3 and R_2=0

2.3. Influence of the position of the light when it passes into SNMI

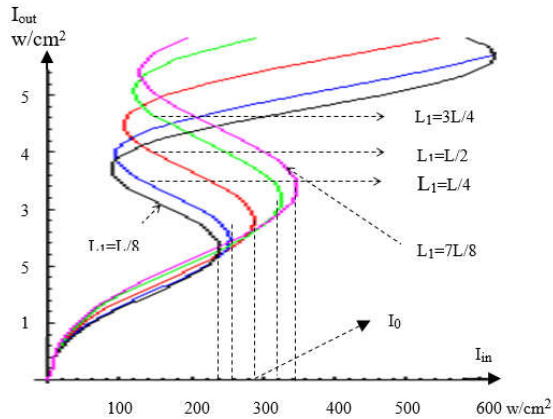**Figure 6.** *Out-input characteristics of SNMI with δ_0=-0.1π; L=1mm; λ=0.85μm, R_1=R_2=0.5; n_2=10^{-4}cm^2/w; α=10^3 and L_1 change with the values of L_1=L/8; L/4; L/2; 3L/4; 7L/8*

With its dependence on the reflectivity R_1 and R_2, the graph of input-output relationship depends very clearly on the position of light as it passes into SNMI. As shown in Fig. 6, when the light rays into SNMI at five different positions on mirror M_1: At the center (L_1=L/2), the four remaining positions symmetrical with each other through the center (each pair a - L_1 = L/8, 7L/8 and L_1 = L/4, 3L/4); we have 5 bistable curves with 5 different "threshold jumps". First beam going from the center of mirror M_1 has "threshold jump" I_0 = 290w/cm^2, beam 2 (position L_1 = L/4) for "jump threshold" is 260w/cm^2, beam 3 (positions symmetrical with positions of beam 2 through the center of mirror M_1, L_1 = 3L/4) to "jump threshold" is 320w/cm^2, beam 4 (position L_1 = L/8) for "jump threshold" is 240w/cm^2, beam 5 (positions symmetrical with positions of beam 4 through the center of mirror M_1, L_1 = 7L/8) to "jump threshold" is 340w/cm^2. Thus the beam located symmetrically with each other through the center of the mirror M_1 will value the "threshold jumps" symmetrical to each other through I_0. This result is because from the different positions, light passes through nonlinear medium (inside SNMI) with different distances so that there are different phase shifts and lead to the intensity of the light sum which will vary and then with the different output intensity for the different "threshold jumps".
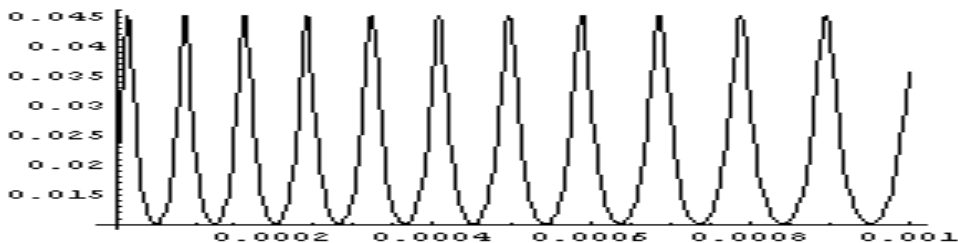

Figure 7. *The dependence of the "Transfer Function" (F = Iout / Iin) on the position of the input light (L1). With δ0=-0.1π; L=1mm; λ=0.85μm, R1=0.45; R2=0.5; n2=10-4cm^2/w; α=103 and Iout=100 w/cm^2*

When changing the position of the light rays in addition to changing "threshold jumps", it also changes the spatial distribution of the "Transfer Function" ($F = I_{out}/I_{in}$). Figure 7 shows the dependence of the "Transfer Function" ($F = I_{out}/I_{in}$) on the position of the input light(L_1) when L_1 changes from 0 to L. We see that Fisa "bell", one of the conditions to confirm SNMI to act as a device for optical bistability.

3. Conclusions

Starting from the classical Michelson interferometer, Symmetry Nonlinear Michelson Interferometer (SNMI) has been proposed and studied. Input-output relationship of the intensity of SNMI has been established on the basis of interference theory. From this relationship, the role of the reflectors and the input position of the light was discussed and simulated by numerical methods. Results showed that could change the design parameters which obtained SNMI with the bistable properties as desired.

References

[1]   Demtroder W (1982), *Laser Spectroscopy,* New York.
[2]   Sakata H. (2001), *Photonic analog-to digital conversion by use of nonlinear Fabry-Perot resonators*, Appl.Phys, 40, 240-248
[3]   N. V. Hoa, H. Q. Quy (2003), *Proc. of the GVS6*, Chemnitz, May 25-31.
[4]   H. Q. Quy, V. N. Sau, N. V. Hoa (2003), *Commun.in Phys.* Vol 13, No.3, pp. 157-164.
[5]   H. Q. Quy, N. V. Hoa (2004), *Proc. of The GVS7*, Ha Long, March 28-April 3.
[6]   N. V. Hoa, H. Q. Quy, V. N. Sau (2005), *Commun.in Phys.* Vol 15, No.1, pp. 6-12.

A RESEARCH FOR USING BAZAN SOIL AS FILLING MATERIALS OF HOMOGENEOUS EARTH DAMS IN TAY NGUYEN AREA

Mai Thi Hong

Abstract: *Using local soil as filling material for homogeneous earth dams could reduce remarkably construction cost. However, the Bazan soil in Tay Nguyen area has strong absorbability and quick disintegration with water. Those properties bring about the difficulty for construction process and could be the reason for the high number of the earth dam accidents in this area in the country. The paper investigates the physical characteristics and mechanical behaviors of Bazan soil. Based on that, proposes the approach for quality improvement and design criterion when using Bazan soil for homogeneous earth dams. The result of experiments reveals that Bazan soil has low dry density and high optimum moisture content, which is the cause of difficulty in the construction phase. Whereas, if suppling 10-12% of mixture weight by using grit, the mechanical properties of mixture is going to be improved significantly and can be used for filling the embankment dam.*

1. Introduction

There were numerous soil dam failures happened in Tay Nguyen area. Most of the earth dams in this location are made of the residual soil, which lies on Bazan basement rock. This local material has strong water absorbability and quick disintegration in water, which is more than what the soil has originated from granite. In 1960-1970's, both designers and builders were confused when they used Bazan soil for dam construction because of mentioned disadvantages. However, after research [1,2] has been conducted, it is more confident to use Bazan soil as filling material for dam construction. In fact, there are a lot of earth dams in Tay Nguyen and Dong Nam Bo region such as dams at Vinh Son hydropower station (at Binh Dinh province), Thac Mo hydropower station (at Binh Phuoc province), etc which have been constructed of Bazan soil, have been working well [3]. Even though, the research, which focused on using Bazan soil as filling material of dam has not been done comprehensively yet.

Mai Thi Hong
Faculty of Engineering and Technology, Hong Duc University
Email: Maithihong@hdu.edu.vn (✉)

The paper investigates the physical characteristics and mechanical behaviors of Bazan soil and proposes the solution, which gives condition for the Bazan soil as filling material for homogeneous earth dams. Besides that, the design criterion of mixture of Bazan soil in homogeneous earth dams is provided to guarantee the safety of the construction process.

2. Materials and methods of the experiment

2.1. Materials for the experiment

The collected material for research is Bazan soil, which is used as filling material at two dams: Tan Son Dam and EaĐrăng Dam, both are in Tay Nguyen area. In general, both of soil samples have a similar ingredient - clay loam without grit. The soil samples are collected, maintained and sent to the special lab for experiment in accordance with TCVN 2683-2012 [4].

2.2. Methods of the experiment

Physical characteristics of soil have been tested as: The particle - size analysis (according to TCVN 4198:2012 [5]), the moisture content of soil (according to TCVN 4196:2012 [6]), the liquid and the plastic limit of soil (according to TCVN 4197:2012 [7]).

Mechanical indicators of soil have been tested as: The optimum moisture content of soil (W_{op}) according to TCVN 4196 [6], the maximum dry density (γ_{cmax}) according to TCVN 4195 [8], the friction angles (φ) and the cohesion (C) according to TCVN 4199-2012 [9], the compressibility coefficient (a) and the deformation modulus (E_o) according to TCVN 4200-2012 [10], the coefficient of permeability (K) according to TCVN 8723-2012 [11], the volumetric shrinkage of soil (D_{cng}) and the shrinkage limit (W_{cng}) according to TCVN 8720-2012 [12], the disaggregation of soil according to 14TCN 132-2005 [13], the swelling of soil according to TCVN 8719-2012 [14].

3. The result of test for soil samples and discussion

3.1. Physical characteristics

The results of the test for the particle-size, the nature moisture content, the liquid and the plastic limit and the density of soil samples are provided in Table 1 and Table 2. According to the result of the grain-size composition of soil, both of two soil samples are clay loam in brown-red colors and do not consist of grit, the particle-size is as follow: $D_{60} = 0.03 \div 0,04$mm; $D_{30} = 0.005 \div 0.006$mm; $D_{10} = 0.0005 \div 0.001$mm. The uniformity coefficient is: Cu $= 6 \div 7$ and the coefficient of curvature is: Cc $= 0.5 \div 1.5$. Hence, the quality of soils is fairly good because its uniformity coefficient corresponds with design criterion, whereas the coefficient of curvature is not quite satisfied [15].

Table 1. *The distribution of particle-size in soil samples*

Particle groups (%) Location	Gravel / Grit	Sand	Silt	Clay
Tan Son Dam	0.33	36.0	39.32	24.34
EaĐrăng Dam	0.27	39.65	32.28	27.79

Table 2. *The parameters of soil samples*

Location	W_o (%)	Gs	W_L (%)	W_p (%)	I_P	LI
Tan Son Dam	34.69	2.71	46.59	32.15	14.44	0.18
EaĐrăng Dam	35.67	2.71	48.27	33.55	14.72	0.14

The calculated indicators in Table 2 show that both of soil samples are clay loam, medium plastic (the liquid limit, W_L=46.59% ÷ 48.27%), the quality of soil samples is reasonable and could be used as filling material. However, it is necessary to carry out further scientific investigations to provide comprehensive physical characteristics and other particular properties of this soil, which is the foundation for comprehensive quality evaluation.

3.2. Mechanical indicators

To evaluate the mechanical indicators, at first, it is necessary to determine the standard value of the maximum dry density and the optimum moisture content. Using those value to calculate the input parameter of prepared samples test. The prepared samples has compactness degree K_c=95 (It means the dry density of soil samples are 95% maximum dry density and the moisture content of soil samples are optimum moisture content). The particular values are in Table 3. After that, dipping the soil samples into Odometer box with water saturation condition in 2 days. In whole process, it requires to provide the pressure of 10 kPa to keep sample not to be expanded. The soil samples were tested to determine the shear resistance, compressibility and permeability of soil sample, when it has been water saturation.

Table 3. *The standard parameters for soil samples*

Location	The optimum moisture content, W_{op} (%)	Maximum dry density, γ_{cmax}(g/cm^3)
Tan Son Dam	30.34	1.42
EaĐrăng Dam	27.89	1.40

The results of the soilsamples for the optimum moisture content and the maximum dry density are shown in Table 3. As it can be seen, the results of tests reveal the particular characteristics of the weathered soil, which has origin from Bazan rock, are low dry density (1.40 ÷ 1.42 g/cm^3) and high optimum moisture content (27.89 ÷ 30.34%). Those features not only lead to the difficulty in construction phase but also cause of safety issue in operation phase.

The results of direct shear test (φ,C) and the other mechanical characteristics of samples as: The compressibility (a) and the deformation modulus (E_o); the permeability (K); the volumetric shrinkage (D_{cng}) and the shrinkage limit (W_{cng}); the swelling; the disaggregation are provided from Table 4 to Table 5 respectively.

Table 4. The results of test for determination of shear strength of soil sample

Location	Friction angle, φ (Degree)	Cohesion, C (kG/cm²)
Tan Son Dam	18°25'	0.278
EaĐrăng Dam	19°22'	0.284

Table 5. The results of test for determination of decay characteristics

Location	Degree of disintegration D_{tr} (%)	Time of disintegration t (s)
Tan Son Dam	13.33	86400
EaĐrăng Dam	29.41	86400

The results show that the shear strength of soil is medium (the friction angles, $\varphi=18°25'$ ÷ 19°22' and the cohesion, C= 0.278 ÷ 0.284 kg/cm²); the bearing capacity and deformation are medium (the deformation modulus, E=82.37 ÷ 97.32 kg/cm² and the compressibility coefficient, a=0.036 ÷ 0.037 cm²/kg); the permeability is low (K= 1.63x10⁻⁶ ÷ 2.21x10⁻⁶ cm/s); the volumetric shrinkage is medium (D_{cng}=9.86 ÷ 11.72%); the soil belongs to non-swelling material group (the volumetric shrinkage, Dtr.n=0.03 ÷ 0.06%) and the disaggregation is slow, therefore that soil could be used as filling material for the dams. However, the results in Table 3 show that: The maximum dry density is relatively small, γ_{cmax}= 1.40 ÷ 1.42T/m³ and the optimum moisture content of soil is high, W=27.89 ÷ 30.34%. For that reason, it is necessary to propose approaches to increase the maximum dry density and also natural density of soil, which will improve the stability of dams.

Table 6. The results of test for determination of compressibility of soil sample

Location	Compressibility coefficient, a (cm²/kg)	Deformation modulus, Eo (kG/cm²)
Tan Son Dam	0.036	82.37
EaĐrăng Dam	0.037	97.32

Table 7. The results of test for determination of permeability of soil sample

Location	Permeability coefficient, K (cm/s)
Tan Son Dam	1.63E-6
EaĐrăng Dam	2.21E-6

Table 8. *The results of test for determination of shrinkage characteristics of soil sample*

Location	The volumetric shrinkage, D_{cng} (%)	The shrinkage limit, W_{cng} (%)
Tan Son Dam	11.72	8.43
EaĐrăng Dam	9.86	8.18

Table 9. *The results of test for determination of expansion characteristics of soil sample*

Location	Volumteric expansion, $D_{tr.n}$ (%)	Expansion moisture, $W_{tr.n}$ (%)	Expansion pressure (Kpa)
Tan Son Dam	0.03	32.72	3
EaĐrăng Dam	0.06	31.96	4

4. Proposing the approaches to use Bazan soil for homogeneous earth dams

4.1. The approach to improve the quality of Bazan-soil mixture

Based on the analysis of test results, the author proposes to mix grit into the soil which increases both the maximum dry density and natural density of soil to improve the stability of dams with shear stress. The soil samples are collected in Tan Son dam to be used for mixing.

According to the methods for determination of compaction characteristics test, the size of grains has to be less than 5mm [16] while the samples have grains with the size distribution 2÷5mm. Therefore, to improve the quality of mixture with consideration of the permeability of filling soil, the author proposes supplementing grits, which has size 5÷10mm. Notice that mixing grits with soil is to reduce significantly the permeability, the shear strength and the deformation of the mixture. In respect to mentioned changes, the effect of mixed grits to the quality of mixture (the permeability, the shear strength, and the deformation) is going to be investigated in the following section.

The process of test for the mixture:

Firstly, the soil sample is dried naturally. After that, the soil sample is isolated to remain its moisture unchanged, we carry out the test to determine the moisture content of the sample. Based on that result, we calculate the dry density of the sample.

Using sieve for shaking soil sample. Bring the grits with size 5÷10mm to dry it up.

Mixing the dry grits with soil sample in the percentage of weight as in Table 10.

Table 10. *The interaction among the percentage of grit, the optimum moisture content and the maximum dry density of mixture*

%Grit	0	3	5	7	10	12	15	20
γ_{dmax}(g/cm^3)	1.42	1.44	1.45	1.47	1.49	1.50	1.53	1.57
W_{opt}(%)	30.34	29.43	28.82	28.21	27.3	26.69	25.78	24.27

To prepare the samples of the mixed-grit mixture with the compactness degree, $K_c = 95$ in correspondent with the maximum dry density and the optimum moisture content.

Dipping the sample into Oedometer box with the water saturation condition in 2 days. In the whole process, to provide the pressure of 10 kPa to keep the sample not to be expanded.

Performing the test to determine the shear resistance, the compressibility, and the permeability of soil sample, when it has saturated water.

The results of those three tests are provided in Tables 11, 12, and 13 respectively. It can be seen that the principle of changed characteristic of mixture is the increase of friction angles, the decrease of deformability and cohesion when the percentage of grits increases. Especially, the coefficient of permeability decreases quickly when the percentage of the grits is more than 12%.

Table 11. The result of test for determination of shear resistance of mixture

% Grit	0	3	5	7	10	12	15	20
φ (Degree)	18°25'	19°22'	20°18'	21°14'	22°9'	23°30'	24°23'	24°49'
C (kG/cm²)	0.278	0.271	0.265	0.259	0.259	0.247	0.228	0.222

Table 12. The result of test for determination of compressibility of mixture

% Grit	0	3	5	7	10	12	15	20
E_o (kG/cm²)	83.61	86,71	97.55	117.06	133.02	146.32	162.58	182.90

Table 13. The result of test for determination of permeability of mixture

% Grit	0	3	5	7	10	12	15	20
K (cm/s)	2.20E-06	2.43E-06	2.67E-06	4.54E-06	7.15E-06	1.43E-05	9.57E-05	2.06E-04

4.2. To propose the design criterion for filling material using Bazan soil

Based on the result of mentioned tests, the author proposes the design criterion for using safely and effectively the Bazan soil as filling material in homogeneous earth dams as in Table 14.

Table 14. The proposal design criterion for the mixture

Proposed criterion	Notation	Unit	Value
Percentage grit	X	%	≤ 30
Natural moisture content	W	%	30 ÷ 40
Liquid limit	W_L	%	≤ 50
Plasticity index	I_P	%	7 ÷ 17
Friction angle	φ	Degree	20 ÷ 24
Cohesion	C	kG/cm²	22 ÷ 26

Compressibility coefficient	a	cm^2/kG	≤ 0.025
Deformation modulus	Eo	kG/cm^2	$130 \div 160$
Permeability coefficient	K	cm/s	$1.10^{-5} \div 1.10^{-6}$
Optimum moisture content	W_{op}	%	$20 \div 26$
Maximum dry density	γ_{cmax}	(g/cm^3)	$1.50 \div 1.60$
Volumetric shrinkage	D_{cng}	%	≤ 12
Volumetric expansion	$D_{tr.n}$	%	≤ 4
Expansion pressure	P	kPa	≤ 10
Time of disintegration	t	Hours	≥ 10

5. Conclusion

The paper has investigated the physical characteristics and mechanical behaviors of Bazan soil. Based on that, the author proposes both the approach to enhance the quality of the mixture of Bazan soil and the design criterion of the mixture. It is to helps using safely and effectively Bazan soil for constructing of homogeneous earth dams. The main results of research are as follow:

The low dry density and high optimum moisture content are the cause of difficulty in execution phase of dam construction, which uses Bazan soil as filling material.

With 10-12% percentage of grits to mixing with Bazan soil, the physical characteristics and mechanical behavior of the mixture have been enhanced significantly. For that quality, the mixture can be used as filling material.

The design criterion, which has been proposed in this paper, aims to use the soil mixture safely and efficiency in the dam construction.

References

[1]   Nguyen Cong Man, *The origination of Bazan soil and its properties in construction*. Hydraulic Magazine, Nr.191, Sep.1978

[2]   Nguyen Van Tho, Pham Van Thin, *The abilities to use Bazan soil as filling material. Hydraulic Magazine*, Nr.191, Sep.1978

[3]   Nguyen Van Tho, Tran Thi Thanh (2001), *Using local soil for dam construction in Tay Nguyen, Nam Trung Bo, Dong Nam Bo.*

[4]   TCVN 2683-2012: Soils - Sampling, packing, transportation and curing of samples.

[5]   TCVN 4198:2012: Soils- Laboratory methods for particle - size analysis.

[6]   TCVN 4196:2012: Soils - Laboratory methods for determination of moisture and hydroscopic water amount.

[7]   TCVN 4197:2012: Soils - Laboratory methods for determination of plastic limit and liquid limit.

[8]   TCVN 4195:2012: Soils - Laboratory methods for determination of Density.

[9]   TCVN 4199-2012: Soil - Laboratory method of determination of shear resistance in a shear box apparatus.

[10]   TCVN 4200:2012: Soils - Laboratory methods for determination of compressibility.

[11]   TCVN 8723-2012: Soil for hydraulic engineering construction - Laboratory test method for determination of permeability coefficient of soil.

[12]   TCVN 8720-2012: Solis for hydraulic engineering construction - Laboratory test method for determination of shrinkage characteristics of soil.

[13]   14TCN 132-2005: Soils. Laboratory methods of determination of decay characteristics.

[14]   TCVN 8719-2012: Soils for hydraulic engineering construction - Laboratory test method for determination of expansion characteristics of soil.

[15]   TCVN 8217-2009: Soil classification for hydraulic engineering

[16]   TCVN 4201:2012: Soils - Laboratory methods for determination of compaction characteristics.

PROPERTIES OF THE WATERPROOFING MATERIAL MADE FROM RECYCLED POLYSTYRENE

Ngo Si Huy, Luu Dinh Thi, Le Van Truong

Abstract: *This paper studies the use of recycled polystyrene, an industrial and domestic waste, to produce the waterproofing material. The components of this material consist of recycled polystyrene, cement, sand, rice hush ash, and sodium silicate, which are popular materials in Vietnam. The properties of waterproofing material are investigated including surface drying time, completed drying time, adhesion, heat resistance and water permeability. Test results indicate that this material satisfies all requirements of waterproofing material stipulated by Vietnam standard.*

Keywords: *Waterproofing material, recycled polystyrene, drying time, adhesion, heat resistance, water permeability.*

1. Introduction

Along with the construction of the building, protecting them from the destruction by environmental factors such as rain water, moisture, sunlight, temperature, corrosive chemicals, etc is also very an important task. Especially in Vietnam, with high rainfall and high humidity, the quality and longevity of the building declined by water intrusion. Therefore, the waterproofing for buildings is very essential. However, most waterproofing materials in the market are imported from abroad, thus the waterproofing cost of buildings is high.

After ten research years, the Department of Chemical Technology, Hanoi University of Science and Technology, has successfully made the waterproofing material suitable for humid tropical climate condition in Vietnam [1]. Nguyen (2013) has studied the waterproofing paint,

Ngo Si Huy
Faculty of Engineering and Technology, Hong Duc University
Email: Ngosihuy@hdu.edu.vn (✉)

Luu Dinh Thi
Faculty of Engineering and Technology, Hong Duc University
Email: Luudinhthi@hdu.edu.vn (✉)

Le Van Truong
Student of Civil Engineering, Faculty of Engineering and Technology, Hong Duc University
Email: Letruong258@gmail.com (✉)

which has a high compressive strength, abrasion resistance, adhesion, and water resistance [2]. Pham et al. (2003) has selected suitable surface coating materials for chemical permeable resistance [3].

In Vietnam, the research on waterproofing materials is limited, while the publication of international research is also limited because researchers keep their work in secret for commercial exploitation. This paper studies the use of recycled polystyrene to produce a waterproofing material. The properties of this material as surface drying time, completed drying time, adhesion, heat resistance and water permeability are also investigated.

2. Experimental program

2.1. Materials

Ingredients to make the waterproofing material include polystyrene, cement, sand, rice hush ash and sodium silicate, which are popular materials in Vietnam. Especially, polystyrene and rice hush ash are domestic, industrial and agricultural wastes. Studying to use these materials contributes to protect the environment, reduce construction cost and use resources effectively.

Polystyrene is a light material with high chemical and water resistance. It was collected from industrial and domestic waste, then washed, dried and dissolved with a sufficient amount of gas to become the liquid gel. Cement used in this study is Nghi Son PC40 with specific gravity of 3.12. In Vietnam, rice hush is available as by-product of agriculture with a large amount of volume. Depending on the burning condition, rice hush ash powder consists of high amount of reactive silica. In this research, rice hush was burned in the furnace at a temperature of 850°C for 3 hours, then was sieved to get the particles with the size of less than 0.15 mm. The physical and chemical properties of cement and rice hush ash are given in Table 1. Natural sand was washed to remove dust, then dried at a temperature of 105-110°C for 6 hours. After that, it was sieved to get the particle with the size ranged from 0.15 mm to 0.25 mm. Sodium silicate was used to increase the workability and heat resistance of the waterproofing material.

Table 1. Physical and chemical analysis of cement and rice hush ash

Items		Cement	Rice hush ash
Physical properties	Specific gravity	3.12	2.16
Chemical compositions (%)	SiO_2	22.38	89.74
	Al_2O_3	5.31	0.96
	Fe_2O_3	4.03	0.52
	CaO	55.93	1.96
	MgO	2.80	1.41
	Loss on ignition	1.98	0.33

2.2. Mixtures

Many mixtures were produced with different mass ratios to find out the optimal ratios. This paper presents five successful mixtures as shown in Table 2. M1 is the basic mixture with the combination of cement, polystyrene and sodium silicate. Sand was added to mixtures M2 and M3. In mixtures M4 and M5, sand was replaced by rice hush ash. Note that the role of sand and rice hush ash are to take part in reaction with cement and are referred to as auxiliary materials. The mass ratio of the components was adjusted to get flexible paste for easy construction. The water resistance of these mixtures is provided by polystyrene, while adhesion strength of them is generated by cement reaction. High polystyrene content leads to low adhesion strength of waterproofing material. Thus, the ratio between cement and polystyrene is suggested not less than 1 and not greater than 5.

The process to make the waterproofing material is as follows: the dried ingredients as cement, sodium silicate, sand, and rice hush ash were mixed first by a glass rod. Then, the polystyrene gel was added and mixed until achieving a homogeneous paste as shown in Figure 1(a). In order to test the properties of the waterproofing material, which has just mixed above, concrete samples were also prepared. Concrete sample surface was covered by a thin waterproofing material layer of 1-2 mm as shown in Figure 1(b). The production and construction processes of this material are simple like cement paste.

Table 2. Mass ratio of mixtures

Mixture No.	Cement	Polystyrene	Sodium Silicate	Sand	Rice hush ash
M1	2	2	1	0	0
M2	2	6	1	4	0
M3	2	4	1	4	0
M4	2	10	1	0	4
M5	2	8	1	0	4

(a)   (b)

Figure 1. a) Waterproofing material; b) concrete sample

2.3. Test methods

All experiments were conducted at Construction Material Laboratory of Engineering and Technology Department, Hong Duc University. The characters of waterproofing material were tested including surface drying time, completed drying time, adhesion, heat resistance and water permeability, which have to satisfy the requirements stipulated by TCVN 6557-2000 [4]. The testes of surface drying time, completed drying time, heat resistance and water permeability were performed in accordance with TCVN 6557-2000 [4], while adhesion test was performed in accordance with TCVN 2097-1993 [5].

3. Test results and discussion

3.1. Surface drying time and completed drying time

Table 3 shows the surface drying time and completed drying time of all mixtures. Test results indicated that the highest drying time for surface and entire layer of the waterproofing material are 6 and 30 hours, respectively. These are much less than 24 and 72 hours as stipulated by TCVN 6557-2000 [4], respectively.

Table 3. *Surface drying time and completed drying time*

Mixture No.	Surface drying time (hours)	Completed drying time (hours)
M1	4	24
M2	6	30
M3	5	28
M4	4	24
M5	4	24

3.2. Adhesion

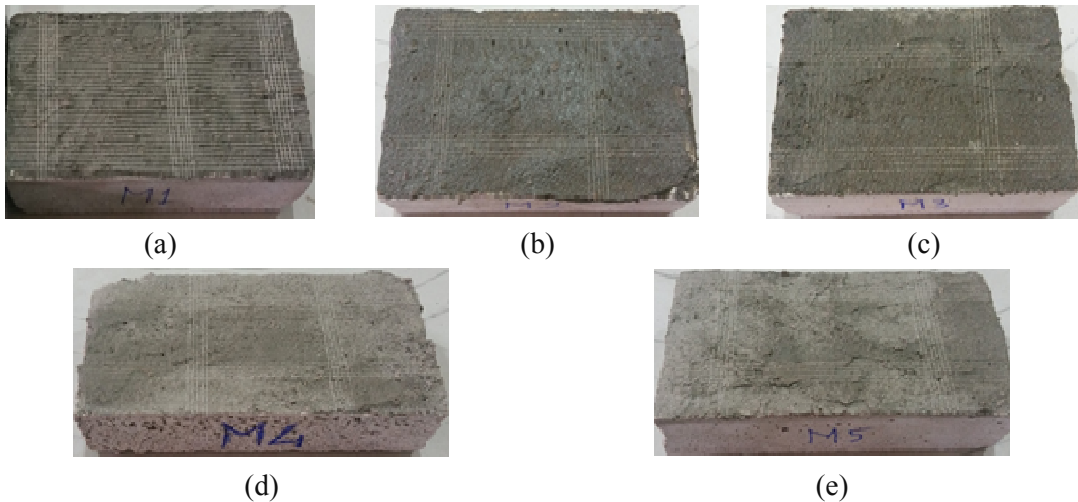(a)   (b)   (c)

(d)   (e)

Figure 2. *Adhesion test of mixtures: (a) M1; (b) M2; (c) M3; (d) M4; and (e) M5*

Figure 2 shows the adhesion test results of all mixtures on concrete surface. Note that, this test was conducted on concrete samples of 150 mm × 100 mm × 50 mm. The cuts by a sharp knife on the surface of the waterproofing material are almost smooth with no peeling membrane. The total area of peeling membrane is less than 5% for all mixtures, satisfying the requirement by TCVN 2097-1993 [5].

3.3. Heat resistance

Figure 3 illustrates the heat resistance test. The picture of all samples after 6 hours in dried oven at $100^{\circ}C \pm 1^{\circ}C$ is shown in Figure 3(b). It is clear that no blistering bubbles were observed in the surface of samples. In other words, the waterproofing material on the surface of concrete samples was not destructed, even harder than before. The same result was obtained since putting these samples into dried oven for additional 24 hours. This finding proves that all waterproofing mixtures can sustain a heat at $100^{\circ}C$ more than 6 hours, satisfying the requirement by TCVN 6557-2000 [4].

(a)   (b)

Figure 3. (a) Heat resistance test; (b) samples after heat resistance test

3.3. Water permeability

3.2.1. Observation

The waterproofing ability of material is characterized by the shape of a liquid on the material surface. For example, the shape of water on the lotus leaf, duck feather, etc is spherical, which is due to the surface tension phenomenon as shown in Figure 4.
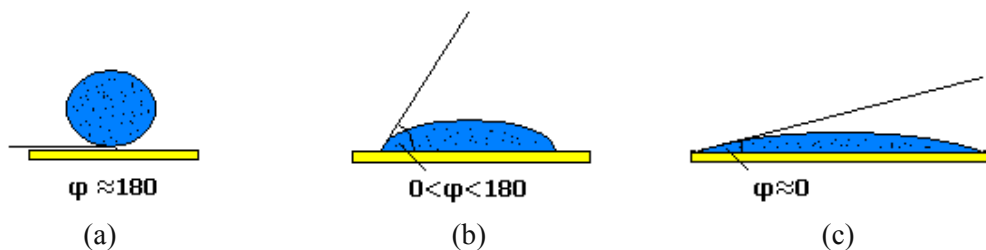

φ ≈180   0<φ<180   φ≈0

(a)   (b)   (c)

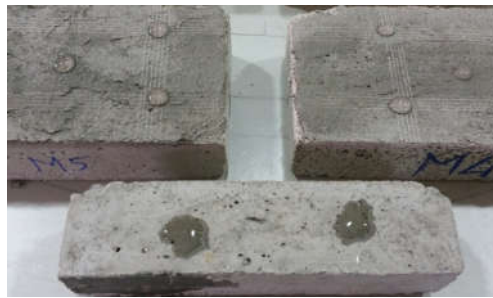*Figure 4. a) impermeability, b) permeability, c) full permeability [6]*

Figure 5. *Observation of a water on material surface*

Figure 5 shows the shape of water on the M4 and M5 mixture surfaces, and on the normal concrete surface without waterproofing material. The shape of water on M4 and M5 is spherical, similar to the shape of water on the lotus leaf, while on normal concrete surface it is irregular with permeable region in outer border of water. The result is similar to waterproofing mixtures M1, M2 and M3; the shape of a water is spherical. This finding proves that all mixtures are water impermeable materials as lotus leaves and duck feathers.

3.2.2. Water permeability

(a)   (b)

Figure 6. *Water permeability (a) after 7 days, (b) after 10 days*

Figure 6 shows the water permeability experiment. This experiment was conducted on carton covered by waterproofing materials. The pressure caused by a water column of 15 cm was put on a carton surface. Test results show that the cartons were still dry after 7 days as shown in Figure 6(a). It means that water can not permeate through the waterproofing material to the carton. After 10 days, the water permeated through the carton for samples covered with the layer of 1-1.5 mm waterproofing materials; however, for samples covered with thicker than 2 mm, waterproofing materials are still impermeable (Figure 6b). It means that the water resistance depends on the thickness layer of waterproofing materials. According to TCVN 6557-2000 [4], the water permeability index requirement is not less than 24 hours. Thus, all waterproofing mixtures in this study possess much greater waterproofing ability than this requirement.

4. Conclusions

This paper studies to make the waterproofing material using the recycled polystyrene. This material also exploited popular materials as cement, sand, rice hush ash and sodium silicate. The production and construction processes of this material are simple. Test results indicate that all waterproofing mixtures in this study satisfy the requirements stipulated by Vietnam Standard of surface drying time, completed drying time, adhesion, heat resistance, and water permeability. Especially, this material is impermeable under a water column of 15 centimeter during 7 days. If the layer thickness of the waterproofing material is greater than 2 mm, it is still impermeable after 10 days.

References

[1]   http://www.chongtham.org/tin-tuc/27-vat-lieu-chong-tham-phu-hop-voi-viet-nam.html (accessed in March 3rd, 2017).

[2]   Nguyễn Quang Phú (2013), *Nghiên cứu chế tạo sơn chống thấm thẩm thấu kết tinh gốc xi măng trong phòng thí nghiệm và ứng dụng trong công trình thủy lợi*, *Tạp chí Khoa học Công nghệ Xây dựng*, Số 1, 24-28 (in Vietnamese).

[3]   Phạm Thế Trình, Nguyễn Anh Dũng, Trần Đức Thắng (2003), *Nghiên cứu lựa chọn các lớp phủ để xây dựng bộ vật liệu chống thấm bền hóa.* (http://www.vinachem.com.vn/xuat-ban-pham/59-so-vnc/c762.html , accessed in March 3rd, 2017).

[4]   TCVN 6557-2000, *Waterproofing material- Rubber-bitumen paint* (in Vietnamese).

[5]   TCVN 2097-1993, *Paint- Cross cut test for determination of adhesion* (in Vietnamese).

[6]   https://vi.wikipedia.org/wiki/Sức_căng_bề_mặt (accessed in March 3rd, 2017).

INTEGRATING BIM EDUCATION INTO CIVIL ENGINEERING CURRICULUM

Nguyen Vu Linh

Abstract: *It is widely accepted that BIM (Building Information Modeling) is going to become an international standard in AEC (Architecture, Engineering, and Construction) industry in the near future. To cope with this, the coming civil engineers should be prepared to have appropriate BIM knowledge at University. Through literature review, the author draws out an overview of BIM technology and current status of its implementation, and the approaches to bring BIM education into the curriculum under expertise point of view. As a result, a list of subjects in Construction Engineering Curriculum at Hong Duc University, which should be tied with BIM knowledge, are proposed and some recommendations also are given.*
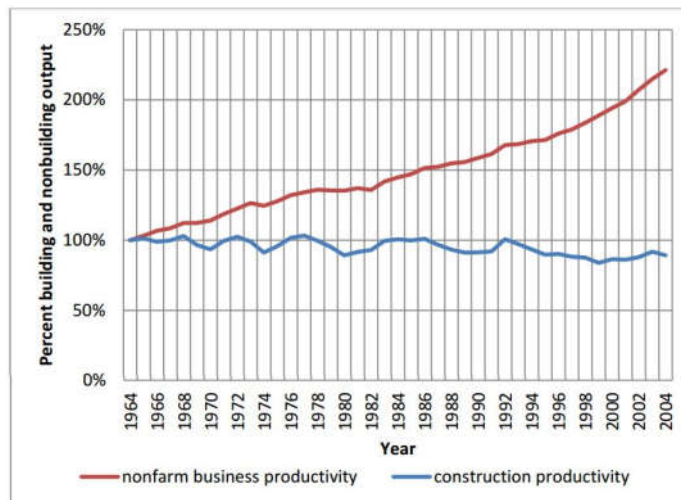
1. Introduction

Figure 1. *Labor Productivity index for the US Construction industry and all non-farm industries*

(Source: Teicholz, Paul. "Labor Productivity Declines in the Construction Industry: Causes and Remedies." AECbytes Viewpoint. Issue 4. April 14, 2004)

Nguyen Vu Linh
Faculty of Engineering and Technology, Hong Duc University
Email: Nguyenvulinh@hdu.edu.vn (✉)

To date, the construction industry is still taking huge proportion resources of every economy, especially in developing country. Therefore, enhancing the resources consumption in AEC projects is of remarkable value for each nation. In US construction market, in 2004 the Construction Industry Institute estimated that 57% of money spent on construction is nonvalue-added, which is waste [1]. Furthermore, there has been no productivity gain in the construction industry over the last 40 years (1964-2004). In fact, there has been a steady decline, whereas all other non-farming industries rose over 200% in productivity (Figure 1).

In addition, it is recognized that the bid process and resultant change orders have become the bane of many construction projects. Hence, the traditional style Design-Bid-Build should be replaced by IDP (Integrated Delivery Project). Additionally, construction projects are becoming more complex and huge with longer time. To deal with that issue, there have been many attempts to solve problems. One of the most promising solutions is BIM technology.

Despites the fact that benefits of BIM have been well known, the implementation level of this concept is various among countries. Besides the developed countries with highly level BIM used, most of developing countries are in early stages of BIM implementation. One of the cause for this pattern is the lack of engineers with adequate BIM training and education, which is costly for small or medium construction company in a developing country. To fill this gap, the universities which are having AEC programs should take responsibility to provide appropriate BIM knowledge for their students, who are going to become the civil engineers. In respect to that concern, this paper aims to provide an initial point of view about the role of BIM with civil engineering students generally and then propose some adoption to bring BIM into the construction engineering curriculum at Hong Duc University particularly.

2. BIM - An overview and current status

The purpose of this section is to provide a better understanding of BIM concept and its benefits for next generation of civil engineers. Additionally, through literature to define BIM characteristics, which will be used to propose the approaches for BIM teaching in the following section.

2.1. BIM technology in brief

The concept of BIM has existed since the 1970s [2]. However, thanks to the development of IT technology (especially 3D-Graphic aid design software), BIM has become a popular concept since early the 2000s, then it has already been mandatory practical level in many developed countries by now, and is going to be an international standard for AEC industry in near future.

There are many definitions of BIM concept. In which, two of those are frequently mentioned. At first, Chuck Eastman et al. (2011) states that "BIM is a fundamentally different way of creating, using, and sharing building lifecycle data". It emphasizes that the object of BIM technology is all relevant data of projects. The second common definition comes from

National Building Information Modeling Standard (NBIMS) of the United States, in which BIM is categorized in three ways:

BIM as a product; which is the building being presented through an intelligent digital model.

BIM as a collaborative process; which is consistent relationships between standardized parametric data, business drivers and all relevant participants.

BIM as a facility; which presents the procedure, workflow, and information exchange during the lifecycle of the project.
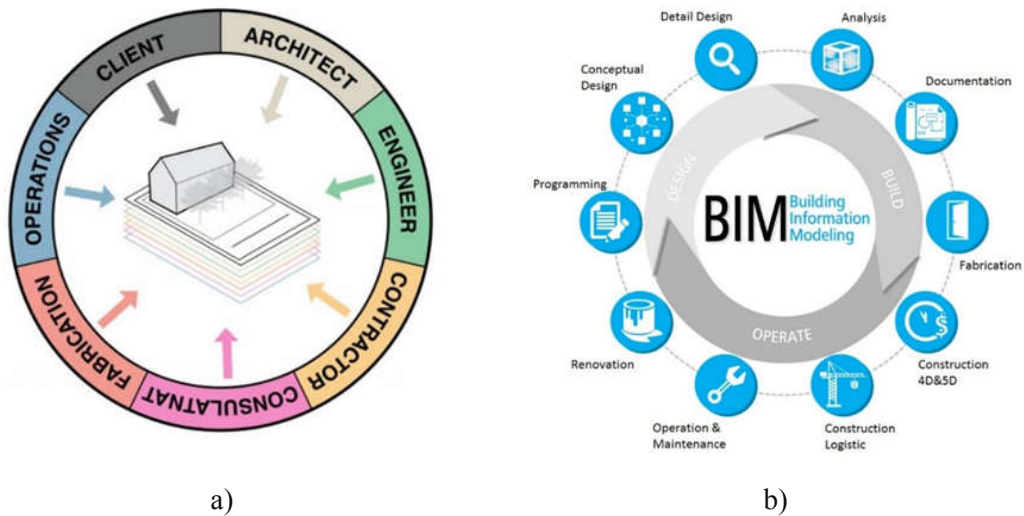

a)   b)

Figure 2. *(a) BIM as a facility; (b) BIM as a collaborative process*

Figure 2 presents two main characteristics of BIM. Figure 2a presents a point of view about BIM models, where all stakeholders participate in the project through a unique BIM model (in their own vision). In another point of view, Figure 2b, the BIM software can be used as a facility for all phase and activities in a construction project: Design-Build-Operate. The main difference between conventional software and BIM is that instead of creating "a product" for every stage (or for some similar tasks), BIM model is unique in every project (or at least with its perspective) will be built up through the wholelife cycle of project and the final model contains all relevant information, which was created in its lifecycle, about the project. In brief, BIM concept is not a new professional knowledge of construction engineering or technology, whereas it is an IT-based model (product, process) to deliver construction project efficiently.

According to Salman [3], the key benefit of a building information model is its accurate geometrical representation of the parts of a building in an integrated data environment. Other related benefits are as follows:

Faster and more effective processes: Information is more easily shared and can be value-added and reused.

Better design: Building proposals can be rigorously analyzed, simulations performed quickly, and performance benchmarked, enabling improved and innovative solutions.

Controlled whole-life costs and environmental data: Environmental performance is more predictable, and lifecycle costs are better understood.

Better production quality: Documentation output is flexible and high automation.

Automated assembly: Digital product data can be exploited in downstream processes and used for manufacturing and assembly of structural systems.

Better customer service: Proposals are better understood through accurate visualization.

Lifecycle data: Requirements, design, construction, and operational information can be used in facilities management.

In brief, BIM concept is an approach to create and manage all data of construction projects in a unique model, which is changing both the efficiency and delivery method of construction project performance. Along with the development of IT technology, BIM concept has already been a technology in construction industry.

2.2. BIM implementation level and current status

As a developing technology, many researchers, organizations and nations have given the guidance and standards for evaluating the implementation of BIM. The section introduces two popular diagrams which describe the level of BIM implementation in construction projects.

Firstly, the level of how far has BIM technology been applied is evaluated through concept "BIM Dimension". It starts with 3D BIM, which provides a3D geometric model. 4D-BIM model includes the scheduling function (time). 5D BIM with the cost to be modeled. 6D-BIM model allows performing energy analysis and 7D-BIM supports facility management. By now the BIM software, which provides BIM services for 4D and 5D dimensions, is using popularly. The latest version of Revit (2017) allows user to perform energy analysis automatically on the model (Figure 3).
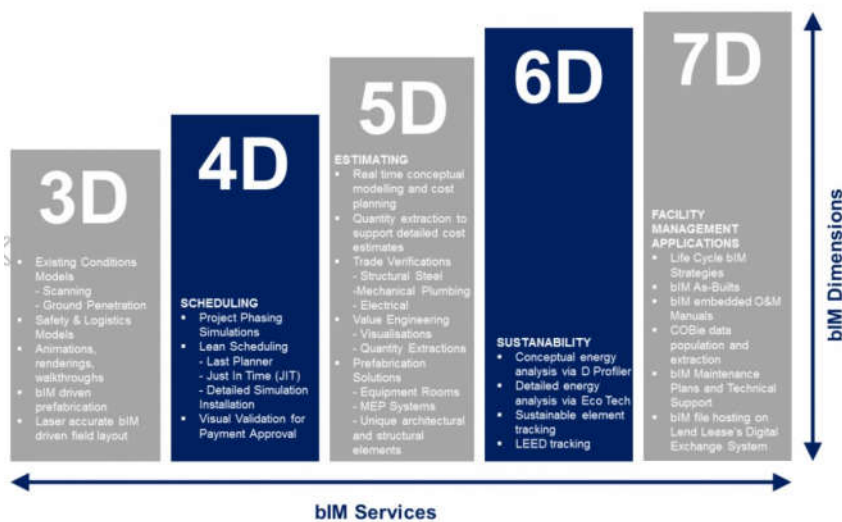

Figure 3. BIM functionality in implementation level

The second approach to assess BIM implementation is considering the level of collaboration and technological sophistication throughout the building process. Eve S. Lin et al. (2015) [4] proposes a diagram of BIM maturity level, which was also adapted from some previous diagrams as show in Figure 4. As can be seen clearly, the trend of development and implementation of BIM is able to perform automatically more services (D-Dimension) with more comprehensive of format (Tools-Platform-Environment).
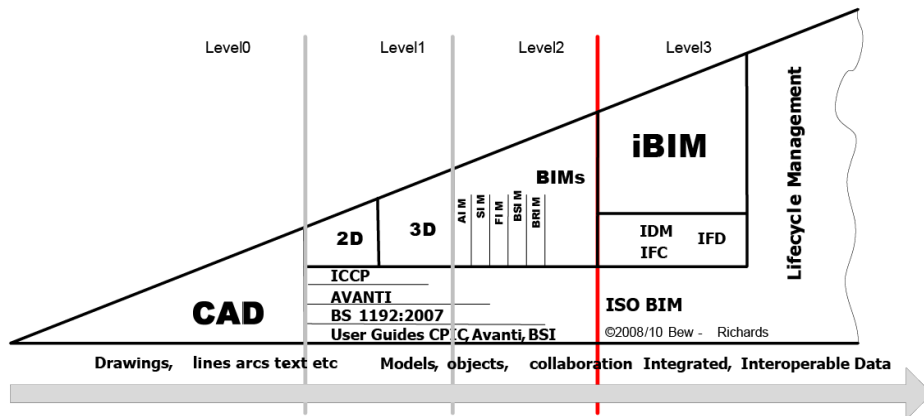

Figure 4. *Illustration of BIM maturity levels*

To address BIM implementation status, plenty of surveys have been conducted. McGraw-Hill Construction(2014) has made an extensive global survey for tracking evolution and implementation of BIM since 2007 to that time. The report reveals that whilst BIM implementation has been led by countries such as US, UK, Germany, Canada, France, and it also has been adopted in countries such as Australia, Brazil, Japan, North Korea and New Zealand. "BIM usage is accelerating powerfully, driven by major private and government owners who want to institutionalize its benefits of faster, more certain project delivery and more reliable quantity and cost" [5]. They also have found significant change over that period and impressive implementation increases over the past few years in particular. For example, in North America, BIM adoption by contractors escalated from 28% in 2007 to 71% in 2012. On the higher implementation level, many national governments have already made BIM as a mandatory requirement such as US, UK, Norway, Denmark, Finland, Netherlands, South Korea, Singapore, Hong Kong [6].

The picture of implementation BIM in two biggest economies of developing countries, China and India, also are promising. In China, a BIM Union was formed in 2013 and "Unified Standard for BIM Application" has been completed and issued for comment [7]. McGraw-Hill Construction(2014) found that BIM implementation in India is in the early stages. However, with the fact that construction market is predicted grown to $620 billion by 2020, many international companies are moving into this market and BIM will come along with them [7].

In Vietnam, there was a research which was conducted by Construction Economics Institute- Construction Ministry of Vietnam to plan for adoption BIM process in the particular

condition of Vietnam. Based on that, BIM will be deployed from 2018 with the certain huge projects [8]. In the meantime, there are several projects, which have mentioned as BIM project with international consultants such as Tran Thi Ly Bridge (Da Nang), Rao Bridge - Binh Bridge (Hai Phong) [9].

In conclusion, BIM has been an actual standard in the construction industry to ensure the success of projects. Using BIM is going to play avital role to enhance competitive capacity of every construction company in globalization era. In consequence, the coming civil engineers should master of BIM technology as such a pillar for their career and the universities have to take their responsibility to bring BIM into the curriculum.

3. The approaches to integrate BIM into civil engineering education

Since BIM has widely been accepted that it should be avital part of civil engineering education, many academic programs are struggling to meet industry and student expectations. BIM education, according to [10], is a process of learning the sum conceptual and practical knowledge relating to BIM technologies, workflows and protocols. Underlying BIM educations are many technical (e.g. data management), procedural (e.g. team collaboration) and regulatory topics (e.g. risk management)". With respect to the given point of view, BIM could be taught in two frameworks: BIM concept is provided throughout related professional subjects or BIM is provided as an individual course. The detail of both ways will be discussed in the following section.

3.2. Teaching BIM as a part of existing subjects

With this approach, the specific BIM course will not be created. Instead of that, BIM content and tools are taught throughout of conventional subjects in the curricula. Obviously, it is understandable when the lecturers bring the up-to-date concept and technology in their lectures. Hence, there have been plenty of attempts in this direction [12,11,13,14]. This list is still growing because, as of today, AEC programs exist that have yet to embark on the BIM journey [15]. Once the important of using BIM tools and concept in the traditional course is emphasized as: "*Since the basics of BIM are about using technology to more effectively collaborate and hand off data sets to alternate use groups, how can that be taught without the integration of multiple educational silos."* [16].

The question comes up with this approach is to define the related areas and subject which should be encouraged to tie up with BIM. In a survey of the implementation of building information modeling (BIM) into existing architecture and construction curriculum in Construction and Architecture schools of United States, Maya M. Joannides (2011) [17] has defined 9 related professional knowledge areas which introduce BIM in their content: Civil, Design, Electrical, Estimating, Mechanical, Project Management, Scheduling, Structural, Technology. The survey reveals the percentage of the class format (lab, lecture, or both) of

courses implementing BIM in the undergraduate curriculum (Figure 5). And it can be seen clearly that the combination of both theory (lectures) and practice (lab) is preferable choices.
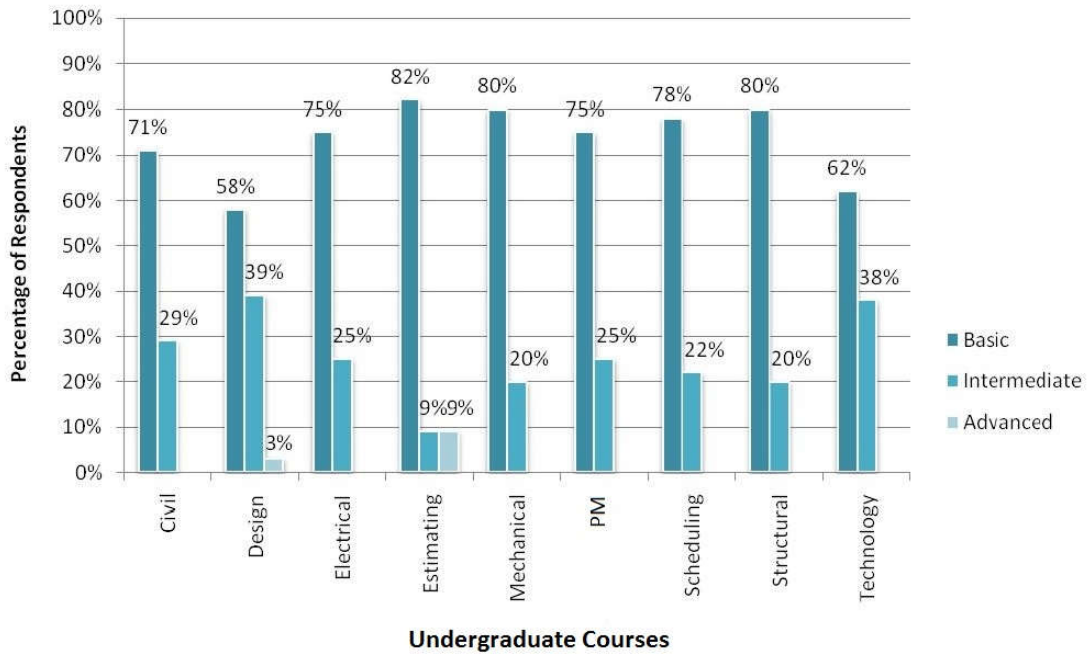

Figure 5. *Class format of Undergraduate Courses Implementing BIM*

Additionally, Willem (2008) [18] stated that "The use of BIM in education can serve to help in design, fabrication, or management related training". It means BIM tools can use to produce *production models (architecture, structural, site plan)* and also *process models (scheduling, cost estimation, planning)*. Based on the above suggestion, the author proposes a list of subjects which could use BIM as effective tools to help students not only achieving professional knowledge but also gain BIM concept/ technology in the Curriculum of Civil Engineering program at Engineering & Technology Department - Hong Duc university as described in Table 1.

Table 1. *List of suggested subjects in civil engineering programs should use BIM as teaching tools in Hong Duc university (Adapted from the official curriculum - version 12.2016)*

Nr	Name of exist subjects	Pts	Type of BIM models	
			Product model	**Process model**
1	Technical Drawing and Visualization	4	x	
2	Descriptive Geometry - Technical drawing	4	x	
3	Applied Informatics for Structural Analysis	2	x	
4	Reinforced Concrete Structure	3	x	

5	Steel Structure	2	x	
6	Civil Engineering Drawing	2	x	
7	Soil and Stone Engineering	2	x	x
8	Design of Reinforced Rock-Brick Structure	2	x	
9	Concrete Construction Engineering	2	x	x
10	Advanced Steel Structure Design	2	x	
11	Construction Project Management	2	x	x
12	Construction Safety	2	x	
13	Construction Planning and Organization	3	x	x
14	Cost Estimating	2	x	
15	Building Architecture	4	x	
16	Reinforced Concrete Bridge Design	4	x	
17	Steel Bridge Design	4	x	
18	Road Design	4	x	
19	Highway Design	4	x	
20	Bridge Construction Technology	4		x
21	Road Construction Technology	4		x
22	High-rise Building Design	4	x	
23	Steel Building Design	4	x	
24	High-rise building technology	4		x
25	Fabricated Engineering	4	x	x
26	Engineering Practice	4	x	x
27	Graduation Thesis	8	x	x

To perform this approach, the lecturers and supporting facilities play an important role. It is obvious that the structure and the number of subjects in the curricula will not change, the difference is that the lecturers will use appropriate BIM concepts, software to provide the current status of BIM application for their lectures. However, lack of experienced educators is a challenge for adopting BIM in AEC education [19]. Therefore, the university has to provide enough needed facilities (Computers, software, books, etc.) for learning BIM and encourage their lecturers to be acquainted with BIM technology.

As discussed above, the approach to integrate BIM knowledge into existed courses in the curriculum could be most applicable at the first phase of implementing BIM into existing curriculum. By introducing BIM along with professional education, it will help new generation of civil engineers start their career with better quality in international construction companies.

3.2. Teaching BIM as a single subject

In this approach, a single BIM course is developed with specific goals of BIM skills and knowledge. In purpose of developing a course "BIM in Construction Management", Ahn et. al. (2013) listed 9 BIM-Related Courses offered by University Construction Programs in the United States. The purpose of courses can be categorized in 2 areas as follows:

Covers visualization, 3D clash detection, fabrication automation, digital site layout, 4D modeling, as-built model generation, and digital information management using BIM.

Introduces a new way of thinking about deliverable documents and the collaborative framework that a parametrically virtual model can provide.

To gain scientific fundamental for developing a content of BIM course, an intensive survey has been made with construction companies and experts [20]. The important areas of BIM-related tasks in participating construction companies and BIM knowledge and skills required for civil engineering students are described in Table 2.

Table 2. BIM tasks in construction company and BIM knowledge and skills required

BIM - Related tasks in a construction company	BIM knowledge and skills required for civil engineering students
1. Spatial trade coordination- MEP coordination	1. General introduction and knowledge of BIM
2. Visualization	2. Areas of implementation in the construction process, including visualization, communication,MEP coordination, and so on
3.Communication	
4. BIM in field management	3. Relationship between general contractor/ construction management and other stakeholders
5. Marketing	
6. Site logistics	
7. Constructability	5. BIM implementation plan
8. Shop drawing and materials procurement	6. Software compatibility
9. Scheduling and sequence planning	7. BIM software skills
10. Safety-related applications	8. BIM and sustainability integration
11. Facility management	9. BIM and integrated project delivery
12. Integrated project delivery system	10. BIM for property and facility management
13. Laser scanning	
14. Simulation of operation - Dynamic animation	
15. Model-based estimating	
16. Energy simulation	

It is clear that making a new BIM course requires cooperation at a higher level (between Faculty and University). The resources (trained people, IT facilities) and time which are needed for establishing this course are also a barrier for the universities. Because of that reason, this approach should be applied after the previously mentioned approach has been used. However, since it is completed technology and is playing a more and more important role in the practice of construction industry, the future civil engineers should be acquainted

deeply with theoretical knowledge of BIM concept/ technology. Therefore, BIM courses should be a vital part of undergraduate civil engineering as soon as possible.

4. Conclusion

By drawing out an overview of BIM technology, its current status, and future, the paper emphasizes the need to bring BIM into Civil engineering education to help the students have a good preparation for their career. The paper also proposed two approaches to integrate BIM into the curriculum: teaching BIM as a part of existing courses and create a new BIM course in the curriculum. Considering all aspects, those two ways should be established respectively, in such a way that both of two approaches will be performed simultaneously.

References

[1] Douglas E. Chelson (2010), *The Effects of Building Information Modeling on Construction Site Productivity*. Doctor of Philosophy. The university of Maryland.

[2] Chuck Eastman, Paul Teicholz, Rafael Sacks & Kathleen Liston (2011), *BIM Handbook: A Guide to Building Information Modeling for Owners, Managers, Designers, Engineers, and Contractors*. 2nd: John Wiley & Sons, Inc.

[3] Azhar, Salman (2011), *Building Information Modeling (BIM): Trends, Benefits, Risks, and Challenges for the AEC Industry*. In Leadership and Management in Engineering 11 (3).

[4] Eve S. Lin; Robert Roithmayr; Simon K. Chiu (Eds.) (2015), *A Review of BIM Maturity for Tensile Membrane Architecture*. Proceedings of the International Association for Shell and Spatial Structures (IASS).

[5] McGraw-Hill Construction (2014), *The Business Value Of BIM for Construction in Major Global Markets*. How contractors Around the World Are Driving Innovation With Building Information Modeling.

[6] Zeiss, G. (2013), *Widespread adoption of BIM by national governments*. Available online at http://geospatial.blogs.com/geospatial/2013/07/widespread-adoption-of-bim-by-national-governments.html, checked on 12. Jan.2017.

[7] Smith, Peter (Ed.) (2014), *BIM Implementation- Global Strategies* (85).

[8] http://kinhtexaydung.gov.vn/tin-tuc/nghiem-thu-de-tai-khoa-hoc-nghien-cuu-xay-dung-lo-trinh-ap-dung.htm

[9] http://per8.com/thong-tin/b-i-m-cong-nghe-cua-tuong-lai.d631/

[10] Succar, Bilal (2012), *BIM Education*. BIM in Practice. Version 1. Edited by Succar Bilal.

[11] Bradley A. Hyatt (Ed.) (2011), *A Case Study in Integrating Lean, BIM, Green, into an Undergraduate Construction Management Scheduling Course*. 47th ASC Annual International Conference Proceedings.

[12] Peterson, Forest; Hartmann, Timo; Fruchter, Renate; Fischer, Martin (2011), *Teaching construction project management with BIM support*. Experience and lessons learned. In Automation in Construction 20 (2), pp. 115 -125.

[13] Sacks, R., Barak, R. (2010), *Teaching Building Information Modeling as an Integral Part of Freshman Year Civil Engineering Education*. In J. Prof. Issues Eng. Educ. Pract. 136 (1), pp. 30 -38.

[14] Wasim Barham, Pavan Meadati, Javier Irizarry (2011), *Enhancing Student Learning in Structures Courses with Building Information Modeling*. In Computing in Civil Engineering.

[15] Wu, Wei; Issa, Raja R. A. (2014), *BIM Education and Recruiting*. Survey-Based Comparative Analysis of Issues, Perceptions, and Collaboration Opportunities. In J. Prof. Issues Eng. Educ. Pract. 140 (2).

[16] Kriengsak Panuwatwanich, Mei Liang Wong, Jeung-Hwan Doh, Rodney A. Stewart and Timothy J. McCathy (Eds.) (2013), *Integrating building information modeling (BIM) into Engineering education: an exploratory study of industry perceptions using social network data*. AAEE2013. Gold Coast, Queensland, Australia. Griffith School of Engineering, Griffith.

[17] Maya M. Joannides (2011), *Implementation Building Information Modeling (BIM) Into Exist Architecture and Construction Curriculum*. Master thesis. The university of Florida.

[18] Willem, Kymell (2008), *Building Information Modeling: Planning and managing construction projects with 4D CAD and Simulation: McGraw-Hill*.

[19] Carol K.H. Hon, EreziUtime, Robin Drogemuller, Robert Bob Owen, Scott Beazley, Madhav Nepal et. al. (Eds.) (2016), *An Evaluation of Learning and Teaching Initiatives for BIM Education at Queensland University of Technology (QTU)*. CIB W78 Conference. Queensland University.

[20] Ahn, Yong Han; Cho, Chung-Suk; Lee, Namhun (2013), *Building Information Modeling*. Systematic Course Development for Undergraduate Construction Students. In J. Prof. Issues Eng. Educ. Pract. 139 (4), pp. 290 -300.

APPLICATION OF FRP COMPOSITES IN STRENGTHENING REINFORCED CONCRETE STRUCTURES - AN INTRODUCTION

Le Duy Tan

Abstract: *This paper reviews the use of fibre reinforced polymer materials in strengthening and retrofitting reinforced concrete structures. There is an increasing need around the world to strengthen concrete structures which are caused by many reasons in the service loads, deterioration of structures with time, fatigue of structures due to repeated loads, especially for bridge structures. FRP composites have been used as a promising solution in replacement of traditional strengthening methods to repair, strengthen and retrofit concrete structures for the last three decades thanks to its advanced properties. Methods of using externally bonded FRP laminates in strengthening concrete structures are presented herein.*

1. Introduction

1.1. FRP materials

The use of fibre reinforced polymer (FRP) materials for strengthening existing reinforced concrete (RC) members has been widely recognized as a highly promising technique with many evident advantages including high strength-to-weight ratio, high corrosion and heat resistance, ease and speed of application, and practically unlimited availability in FRP sizes, geometries and dimensions [1, 2]. The types of FRP available for strengthening are carbon, glass and aramid in the shapes of plates, sheets, strips, rebars and rods. The most commonly used FRP strengthening methods are: the use of externally bonded FRP plates, sheets or strips on the surface of a concrete member or the use of near surface mounted FRP bars, which are embedded in concrete block via grooves, and the use of FRP rods as prestressing tendons. The application of FRPs to existing RC structures can be grouped into axial, shear, and flexural strengthening. External wrapping with FRP sheets for flexural, shear and axial strengthening of RC members is of the interest of this paper.

Le Duy Tan

Faculty of Engineering and Technology, Hong Duc University

Email: Leduytan@hdu.edu.vn (✉)

1.2. Needs to strengthening

There are many reasons that a structure need to be strengthened including the increase in the service loads, deterioration of structures with time, or fatigue of structures when subjected to repeated loads, especially for bridge structures or errors during construction. In fact, deficiencies related to aging bridges or increase in the loading standards, have become a major concern in many countries in the last three decades.

In the United States, more than 70% of the bridges were built before 1935 [3], and a large proportion of the United Kingdom's current bridge stock was built between the late 1950s and early 1970s [4]. Due to various types of deterioration and partly because loading standards have increased over the years, many of these bridges are now defined as deficient bridges.

American Society of Civil Engineers [5]reported that in 2012, one in nine, or just below 11%, of the nation's bridges were classified as structurally deficient, in which 22 states have a higher percentage of structurally deficient bridges than the national average, while five states have more than 20% of their bridges defined as structurally deficient. 24.9% of the nation's bridges were defined in either deficiency category. In the United Kingdom, it was estimated that 20% of the 155,000 road bridges had some sort of strength deficiency [6].

In New South Wales, Australia, around 70% of bridges were built before 1985, with a significant percentage in the mid 1930's, and the peak in the 70's [7]. Australia's infrastructure condition was assessed to be in urgent need of rehabilitation especially for the highway bridges [8].

In Vietnam, most of bridges were built before 1954, in which 1,672 bridges were classified as structurally deficient bridges reported by Directorate for Roads of Vietnam (DRVN). In 2012, it was stated that there are 566 deficient bridges which need to be strengthened, wherein 148 bridges have been projected to repair, 111 bridges are in urgent need of repair and retrofitting using investment construction capital, while 45 bridges and 262 bridges call for retrofitting and upgrading in the periods of 2012-2015 and 2015-2020, respectively.

Strengthening RC structures using FRPs composites has been done and applied in many countries including Japan, United States, Canada, and United Kingdom since 1990s. It, however, is still a new material to Vietnam. As the author is aware, there was only a group of researchers at University of Transportation and Communication, Hanoi are involving in this field of research and application. This paper aims at giving a general view on the application of FRPs on strengthening RC structures.

2. Mechanical properties of FRPs

Three types of FRP laminates namely Glass fibre reinforced polymer (GFRP) laminates, Carbon fibre reinforced polymer (CFRP) laminates, and Aramid fibre reinforced polymer (AFRP) laminates have been used for strengthening RC structures both in practical

and research. The details of mechanical properties of FRPs and their forming process can be found elsewhere [2, 9].

Figure 1 shows an example of a roll of CFRP laminate.

It is worthy to note that despite steel material, which show an elasto-plastic behavior after yielding, all three types of FRP laminates behave linearly elastically up to failure, which is brittle rupture in nature when subjected to tension (Fig.2)
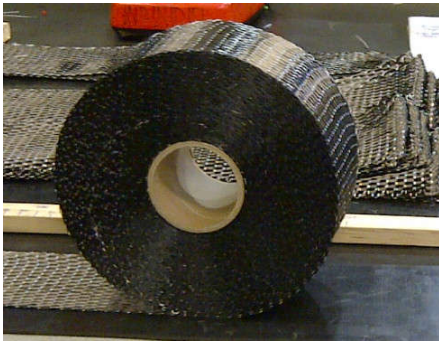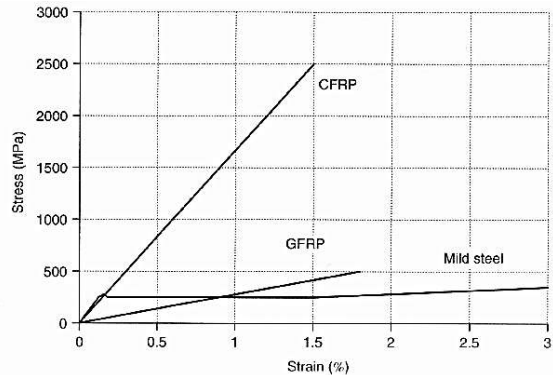

Figure 1. *A roll of CFRP laminates*

Figure 2. *Typical FRP and mild steel stress-strain curves*

3. Externally bonded FRP laminates

Externally bonded FRP systems can be used for flexural, shear strengthening, and axial strengthening of members subjected to axial forces or combined axial and bending forces. There are a number of guidelines and standards on the design and construction of externally bonded-FRP systems for strengthening RC structures [2, 10-12].

3.1. Flexural strengthening

Bonding FRP laminates to the tension face of a concrete flexural member with fibres oriented along the length of the member shows an increase in both flexural strength and ductility of RC beams (Fig. 3). The increase in the ultimate streng this found to be ranging from 28% to 97% of that of unstrengthened beams depending on different types of laminates used [13-15]. Faza and GangaRao [16] reported an increase of 200% in strength when CFRPC laminates are wrapped around beams.
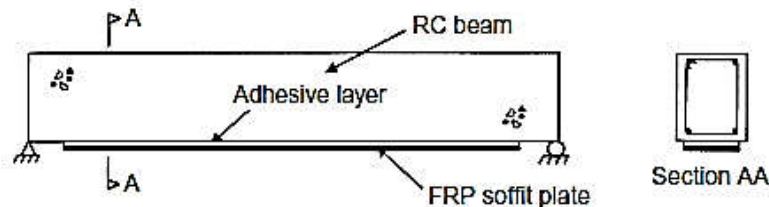

Figure 3. *Bonding FRPs to the soffit of a beam*

A key issue in the design of an effective retrofitting solution using externally bonded plates is the end anchorage strength [17]. The end anchorage strength greatly affects the failure modes of the strengthened system, which in turn affects the ultimate strength capacity of the strengthened beams and the selection of calculation models. If the ends of the plate are properly anchored, then failure occurs when the ultimate flexural capacity of the beam is reached, by either tensile rupture of the FRP plate or crushing of concrete in the compression fibre depend on the amount of strengthening (Fig. 4a, b).
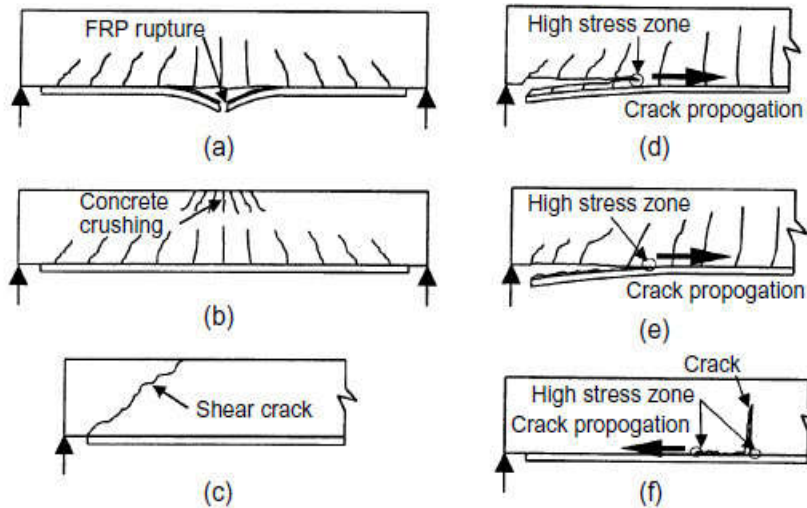

Figure 4. *Failure modes of strengthened beams*

Whereas, incorrect anchorage system or beams without anchors at the plate ends may resulted in premature debonding failures characterized by plate end debonding and concrete cover separation due to the high interfacial shear and normal stresses at the laminate end (Fig. 4d, e, f). These interfacial shear and normal stresses can be reduced by extending the bonded length of the FRPs. There, however, exists a certain bonded length, over which no increases in the end anchorage strength are shown [17, 18]. As such, other methods in order to increase the end anchorage strength are developed. A review of anchorage systems for externally bonded FRP laminate systems was conducted by [19]. Examples of common anchorage systems are shown in Figures 5-8.
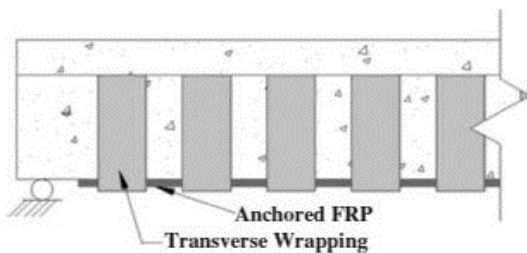

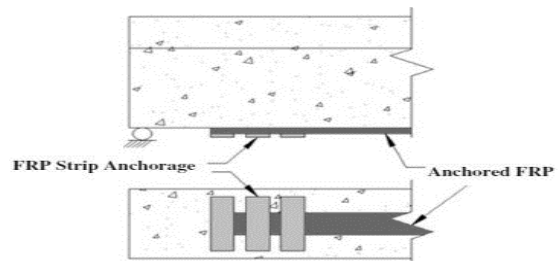**Figure 5.** *Transverse wrapping anchorage on T-beam*

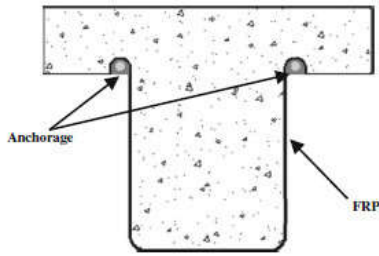

Figure 6. *FRP strip anchorage*

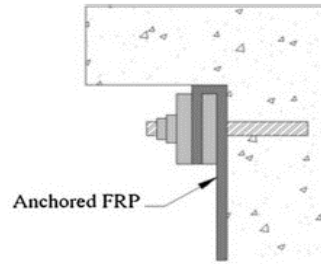**Figure 7.** *Schematic of typical U-Anchor*

Figure 8. *Plated anchorage types*

3.2. Shear strengthening

Three types of wrapping schemes are often used to strengthen RC beams in shear, including side bonding, U-jacket and completely wrapping FRP around the section of the beams. FRP can be aligned vertically, horizontally or diagonally at an angle to the beam's longitudinal axis. An angle of 45° is normally used in the case of diagonally wrapping the FRP at an angle (Fig. 9).
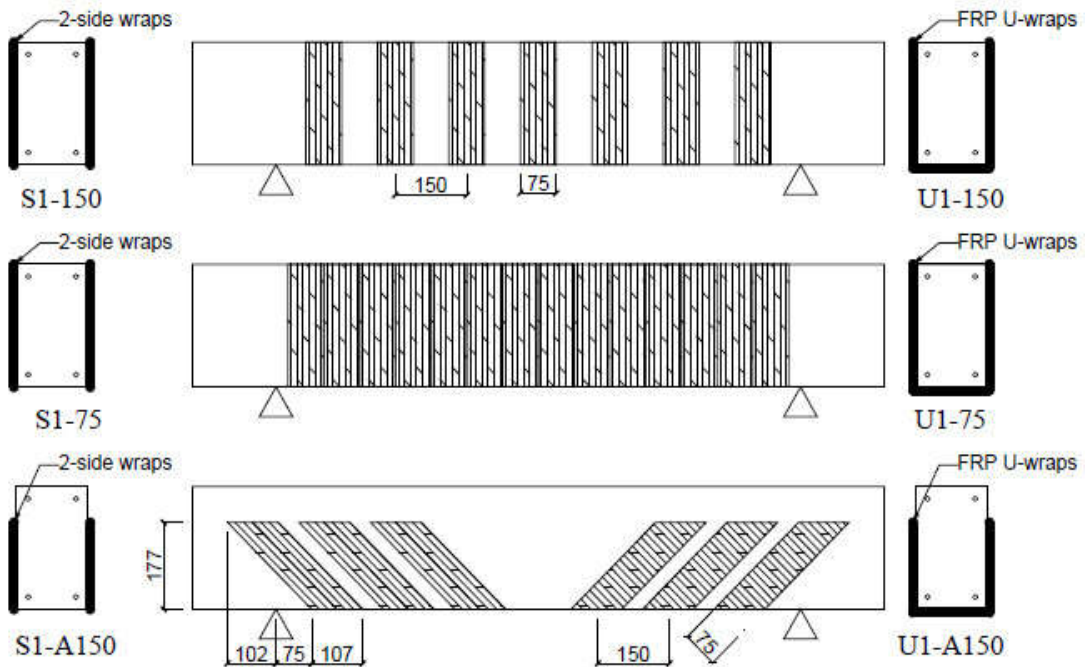

Figure 9. *Strengthening beams in shear*

Literature reveals that the fibre orientation of the FRP strongly affects the effectiveness of the FRP system in terms of shear enhancement and the propagation of inclined cracks of a FRP-strengthened beam in shear.

Vertical and diagonal FRP wraps were used by several researchers [20, 21]. The test results showed both vertical and diagonal strips contributed to the increase of the ultimate force of the beam, in which the diagonal strips outperformed the vertical strips.

117

Horizontal, vertical CFRP sheets and their combinations were used in the study of Adhikary and Mutsuyoshi [22] to strengthen RC beams in shear. The tests revealed that the specimen strengthened with vertical FRP sheets displayed a greater ultimate strength as compared to the specimen strengthened with horizontal FRP sheets. The beam with both horizontally and vertically aligned FRP sheets showed slightly higher diagonal crack strength than the beam with only horizontally aligned FRP sheets.

3.2. Axial strengthening

FRP systems can be used to increase the axial compressive strength of a concrete column by providing confinement with a FRP jacket [2]. By orienting the FRP layers transverse to the longitudinal axis of a member, the transverse or hoop fibres are similar to conventional spiral or tie reinforcing steel (Figs. 10-11). Due to its high modulus of tensile elasticity in the fibre direction, FRP layers can provide a considerable confinement pressure to the concrete core of the member under axial compressive loads. This confinement action delays the crushing of concrete, thereby increasing the compressive strength and deformation capacity of the column.

Figure 10. *Strengthening rectangular columns with hoop FRP sheets*

Figure 11. *Strengthening circular columns with (a) hoop FRP sheets, (b) steel strips*

The improvement of the axial behavior of FRP confined concrete has been verified by a number of studies [23, 24]. Most of these studies were carried out on plain concrete cylinders, having typical dimensions of 150 mm in diameter and 300 mm in height. The specimens were wrapped with FRP layers in the hoop direction. All these studies have indicated that FRP jackets enhance the compressive strength and ductility of confined concrete. These increases substantially depend on: the properties of FRP jackets such as strain capacity and stiffness; thickness of FRP jackets such as the number of FRP plies; and types of FRP jackets such as CFRP, GFRP, and AFRP.

The effectiveness of FRP is also strongly influenced by the cross-section geometry. FRP jackets are most effective in confining members with circular cross-sections in terms of both strength and ductility. For noncircular cross-sections i.e. square and rectangular sections, the increase in the maximum axial compressive strength is marginal [25, 26]. This is due to the stress concentration at the corners of the section resulting in non-uniform distributed stress surrounding the member's cross-section.

These enhancements, however, are achieved only when a column is tested concentrically or when the eccentricity of the load is small. In fact, Bank [9] has shown that the strength enhancement is only of significance for members in which compression failure is the controlling mode. When the eccentricity is large, the effectiveness of hoop FRP layers is significantly reduced because both axial action and bending action are induced. This reduction due to the effect of eccentricity is true for both circular and non-circular cross-section columns [27, 28].

In the case, when the eccentricity of the load is large, the use of vertical and inclined oriented FRP layers significantly contributes to the gain in the strength and ductility of the strengthened columns [29, 30]. In their study, Hadi and Widiarsa [29] used square, reinforced concrete columns confined with CFRP. The influence of the presence of vertical FRP straps was investigated. The specimens were tested under eccentricities of 0, 25, 50 mm and pure bending loading. The results of the study showed that the application of the vertical CFRP straps significantly improved the performance of the columns with large eccentricity. In the case of concentric loading, the specimens with vertical FRP straps showed an 8.4% increase in the maximum strength relative to the unwrapped specimen. Meanwhile, increases of 17.8% and 14.8% were achieved when testing specimens under eccentricities of 25 and 50 mm.

4. Conclusion and recommendation

The use of externally bonded FRP laminates for flexural, shear and axial strengthening of concrete structures has been reviewed in this paper. Several conclusions can be made as follows:

FRPs can effectively be used as an alternative solution replacing traditional strengthening methods such as constructing an additional reinforced concrete cage or installing grout-injected steel jackets. Literature review shows that FRPs can ensure both structural, aesthetical and economical aspects in strengthening and retrofitting concrete structures.

Externally bonded FRPs can greatly enhance the strength and ductility of the concrete structures. FRPs can be used for strengthening concrete structures in flexure, shear and axial loads. The enhancement in the behavior of a FRP-strengthened beam is influenced by many factors including,1) FRP system,i.e. FRP properties, FRP thickness, wrapping schemes, fibre orientations; 2) Conditions of existing structures such as beam's geometry, concrete strength, steel reinforcement ratios (transverse and longitudinal steel reinforcement); 3) Loading schemes and loading types such as concentric or eccentric loads, static, or dynamic loads.

FRPs have been used for strengthening concrete structures since 1990s, however, it is still a new material to Vietnam both practical and research community. Therefore, it is highly recommended to study the application of this material in reply to the current need of repair, retrofit and strengthening structures in Vietnam. In which, factors affecting the actual working conditions of the structures such as traffic loading conditions, climate conditions on the long-term behavior of FRP system are focused on.

References

[1]   Sheikh, S.A., S.A.D. Jaffry, and C. Cui (2007), *Investigation of Glass-Fibre-Reinforced Polymer Shells as Formwork and Reinforcement for Concrete Columns.* Canadian Journal of Civil Engineering. 34(3): p. 389-402.

[2]   ACI 440.2R (2008), *Guide for the Design and Construction of Externally Bonded FRP Systems for Strengthening Concrete Structures.* American Concrete Institute, Farmington Hills, USA.

[3]   Golabi, K., P. Thompson, and W. Hyman (1993), *Points: a network optimization system for bridge improvements and maintenance Technical manual.* Publication number FHWA-SA_94-031: US Department of Transportation, Federal Highway Administration.

[4]   Flaig, K.D. and R.J. Lark (2000), *The development of UK bridge management systems.* Proc. Instn Civ. Engrs Transp 2000. 141(May): p. 99-106.

[5]   American Society of Civil Engineers (2013), *Report Card for America's Infrastructure: Bridges.*

[6]   William, T.K. (1997), *Bridge management problems and options Safe of Bridges,* Thomas Telford, London, pp. 131-137.

[7]   Ariyaratne et al. (2009), *Development of a model for assessment of future condition of bridges. University of Technology Sydney, Centre for built infrastructure research.*

[8]   Engineers Australia (1999), *A report card on the nation's infrastructure: investigating the health of Australia's water systems, roads, railways and bridges.* Barton, ACT.

[9]   Bank, L.C. (2006), *Composites for Construction: Structural Design with FRP Materials.* John Wiley & Sons, Hoboken, NJ, 560.

[10]   Canadian Standard Association (2012), *Design and construction of building components with fibre-reinforced polymers CAN/CSA S806.* Rexdale (ON), pp. 55.

[11]   CEB-FIP (2001), *Externally bonded FRP reinforcement for RC structures.Comité Euro-International du Beton/Fed́eration International Précontrainle*, Bulletin 14, Paris.

[12]   Concrete Society (2004), *Design guidance for strengthening concrete structures using fibre composite material.* Technical Rep. No. 55, Crowthorne, UK.

[13]   Chajes, M.J., et al. (1994), *Flexural strengthening of concrete beams using externally bonded composite materials.* Construction and Building Materials. 8(3): pp. 191-201.

[14]   Ramana, V., et al. (2000), *Behavior of CFRPC strengthened reinforced concrete beams with varying degrees of strengthening.* Composites Part B: Engineering. 31(6): pp. 461-470.

[15] Takeda, K., et al. (1996), *Flexural behaviour of reinforced concrete beams strengthened with carbon fibre sheets*. composites Part A: applied science and manufacturing. 27(10): p. 981-987.

[16] Faza, S.S. and H.V. GangaRao (1994), *Fiber Composite Warp for Rehabilitation of Concrete Structures. in Infrastructure: New Materials and Methods of Repair*. ASCE.

[17] Chen, J. and J. Teng (2003), *Shear capacity of FRP-strengthened RC beams: FRP debonding. Construction and Building Materials*. 17(1): p. 27-41.

[18] Teng, J.G., et al. (2002), *FRP-strengthened RC structures*. John Wiley & Sons Ltd., West Sussex, England.

[19] Grelle, S.V. and L.H. Sneed (2013), *Review of anchorage systems for externally bonded FRP laminates.* International Journal of Concrete Structures and Materials. 7(1): p. 17-33.

[20] Chaallal, O., M.J. Nollet, and D. Perraton (1998), *Shear strengthening of RC beams by externally bonded side CFRP strips*. Journal of Composites for Construction. 2(2): p. 111-114.

[21] Jayaprakash, J., A.A.A. Samad, and A.A. Abbasvoch (2010), *Investigation on effects of variables on shear capacity of precracked RC T-beams with externally bonded bi-directional CFRP discrete strips*. Journal of Composite Materials. 44(2): p. 241-261.

[22] Adhikary, B.B. and H. Mutsuyoshi (2004), *Behavior of concrete beams strengthened in shear with carbon-fiber sheets. Journal of Composites for Construction*. 8(3): p. 258-264.

[23] Nanni, A. and N.M. Bradford (1995), *FRP jacketed concrete under uniaxial compression. Construction and Building Materials*. 9(2): p. 115-124.

[24] Toutanji, H.A. (1999), *Stress-strain characteristics of concrete columns externally confined with advanced fiber composite sheets*. ACI Materials Journal. 96(3): p. 397-404.

[25] Harries, K.A. and S.A. Carey (2003), *Shape and "gap" effects on the behavior of variably confined concrete*. Cement and Concrete Research. 33(6): p. 881-890.

[26] Rocca, S., N. Galati, and A. Nanni (2008), *Review of design guidelines for FRP confinement of reinforced concrete columns of noncircular cross sections. Journal of Composites for Construction*. 12(1): p. 80-92.

[27] Hadi, M.N., T.M. Pham, and X. Lei (2012), *New method of strengthening reinforced concrete square columns by circularizing and wrapping with fiber-reinforced polymer or steel straps*. Journal of Composites for Construction. 17(2): p. 229-238.

[28] Pham, T.M., X. Lei, and M.N. Hadi (2013), *Effect of eccentric load on retrofitted reinforced concrete columns confined with FRP*.

[29] Hadi, M.N.S. and I.B.R. Widiarsa (2012), *Axial and Flexural Performance of Square RC Columns Wrapped with CFRP under Eccentric Loading*, Journal of Composites for Construction. 16(6): p. 640-649.

[30] Hadi, M.N.S. and T.D. Le (2014), *Behaviour of hollow core square reinforced concrete columns wrapped with CFRP with different fibre orientations*. Construction and Building Materials. 50: p. 62-73.

ARTIFICIAL LIGHTWEIGHT AGGREGATE MADE WITH NGHI SON FLY ASH

Le Phuong Thanh

Abstract: *The study focuses on the production of fly ash lightweight aggregate. The basic physical properties and mechanical characteristics of lightweight aggregate produced are analyzed systematically. Factors affecting the efficiency of pelletization process such as type of binder, moisture content, process duration and alkali content are evaluated. Further, characterization of aggregates was evaluated based on the specific gravity, gradation, density and aggregate crushing strength. It is observed from the test results that different aggregates were found to be maximum when the angle of pelletizer is set to 36^0 with a speed of 55 rpm.*

Keywords: *Geopolymer aggregate, fly ash, lightweight aggregate, Nghi Son fly ash.*

1. Introduction

Fly ash from thermal power plant is being beneficially utilized for various engineering purpose including the production of pozzoland cement, fly ash bricks, lightweight blocks as well as producing artificial lightweight aggregates [1]. The production of artificial fly ash lightweight aggregate is effectively carried out by two techniques namely granulation and compaction. The processing of agglomeration theory was developed in 1940's [2]; Granulation technique involves in the formation of solid pellets by addition of moisture and further with the application of rotating force. Whereas, the compaction techniques involve the formation of pellet and well compacted by using briquettes apparatus for hard pressing. Fly ash aggregates produced can be used either as such as produced in cold-bonding method or by further strengthening using sintering at high temperature beyond 900ºC. The sintering process envisages the particles to fuse together at higher temperature range of 900^0C to 1200ºC. Most disc or pan type pelletizer machines were easy to operate and produce different gradation of aggregates as compared to other type of pelletizer machines. The fabricated disc pelletizer machine adopted in different research studies showed that the angle can be adjusted between 36º to 45º, speed of 45 to 55 rpm, diameter of 0.5m and side depth of 0.25m. Cold-bonded, autoclaving and sintering process were the three different methods adopted for further hardening of a pellet. Normally class F fly ash is always preferred for sintering process and

Le Phuong Thanh
Faculty of Engineering and Technology, Hong Duc University
Email: Lephuongthanh@hdu.edu.vn (✉)

class-C fly ash for cold-bonding process [3]. Efficiency of pellet depended on the fineness value of fly ash [4]. Also, the previous study showed that the effects of binder material did not result in the change in chemical composition but enhanced the microstructure of the aggregate thereby improving the mechanical properties of aggregates. [5]. The cold-bonded fly ash aggregate was studied on the partial replacement of cement as fly ash and replacement of sand with fly ash to study the properties of concrete [6]. The water absorption of lightweight aggregate concrete reported to be substantial and thus affects the strength of concrete [7]. The increase in speed of pelletizer resulted in less water absorption of the artificial aggregate [8]. The reduction of porosity of lightweight aggregate was not fully followed by the crushing strength of aggregate and its additional influencing mineral changes and internal thermal stress [9]. The effects of curing in cold-bonded fly ash aggregate were examined in normal water and auto clave curing and showed a reasonable improvement in strength [10]. The crushing strength of hardened pellet was higher for smaller sized aggregates compared to larger size. Moisture content of fly ash aggregate varies from 15% to 35% (high); however, with increased moisture muddy balls are formed instead of smaller pellets. The porosity of fly ash lightweight aggregate was found to be reduced with curing and resulted in gradual reduction in the water absorption [11]. The strength of lightweight aggregate concrete depended on the strength of fly ash aggregate and improved bonding effect on aggregate/cement matrix in the transition zone [12]. The motivation of the present study is on the production of different type of geo-polymer based aggregate and to identify the factors influencing the efficiency of production such as duration, strength of NaOH added in fly ash and type of binder used. Also, the relative assessment of the fly ash aggregates was made from specific gravity, water absorption, bulk density, gradation and individual crushing strength properties.

2. Experimental procedure

2.1. Materials

Fly ash obtained from Nghi Son thermal power plant was used as raw material for aggregate production. The efficiency and strength properties of aggregate were evaluated with the addition of binders such as cement and metakaolin and alkali activator. The physical and chemical properties of various raw materials used in aggregate production are provided in Table 1.

Table1. Physical and chemical properties of various binder materials used

Observation	fly ash	Cement	Meta kaolin
Specific gravity	2.1	3.13	2.52
Blaine's fineness: m^2/kg	400	325	800
Chemical properties (%)			
SiO_2	46.64	18.5	41.4
Al_2O_3	26.13	5.24	30.5
Fe_2O_3	6.22	5.9	1.0

CaO	1.96	60.9	0.3
MgO	1.91	1.1	1.8
SO_3	1.01	1.5	0.9
Na_2O	0.13	-	0.9
K_2O	4.33	-	-
Loss on ignition	10.41	0.8	18.16

The water content for pelletization was optimized at 25% of total binder and alkali activator (sodium hydroxide) of molarity 8M, 10M and 12M was used. The mixed combination for various types of aggregates produced with different fly ash - binder proportions are given in Table 2.

Table 2. *Mix combination for various types of fly ash lightweight aggregate*

Mix type	Fly ash (%)	Cement (%)	Meta Kaolin (%)	Water content (%)	Molarity of NaOH	Note
F1	100	-	-	25	8M	Hot air oven at 100^0C
F2	100	-	-	25	10M	
F3	100	-	-	25	12M	
NC1	80	20	-	25	8M	
NC2	80	20	-	25	10M	
NC3	80	20	-	25	12M	
NK1	80	-	20	25	8M	
NK2	80	-	20	25	10M	
NK3	80	-	20	25	12M	
C1	80	10	-	25	-	Nomal water curing
C2	80	20	-	25	-	
C3	80	30	-	25	-	

2.2. Agglomeration process

The manufacturing of fly ash lightweight aggregate was carried out using Nghi Son fly ash with the addition of cement and metakaolin and alkali activator. A specially fabricated disc pelletizer as shown in Figure1 was used in this study which has a disc diameter of 500 mm and depth 250 mm. The angle of the disc can be adjusted between 35° to 50° and speed of 55 rpm.

Figure1. *Fabricated disc pelletizer machine*

2.3. Curing process

Alkali based fly ash aggregates show accelerated strength improvement at higher temperature due to effective polymerization. In the study, effective curing was also carried out in hot air oven at 100ºC for a period of 7 days as shown in Figure 2.

Figure 2. *Hot air oven machine*

2.4. Crushing strength test

The crushing strength of individual fly ash aggregate was determined by loading the aggregates in diametral direction using a CBR testing machine (shown in Figure 3). A total of 30 samples of the same aggregate size were tested for crushing strength in each type of aggregates. The size of the aggregate used for testing consists of 18 mm and 20 mm diameter. The crushing strength of the pellet was determined using the formula given below:

$$\sigma = \frac{2.8 * P}{\pi * X^2}$$

Where X is the distance between the two plates, P is the fracture load (N) and σ is the crushing strength (MPa) [13].
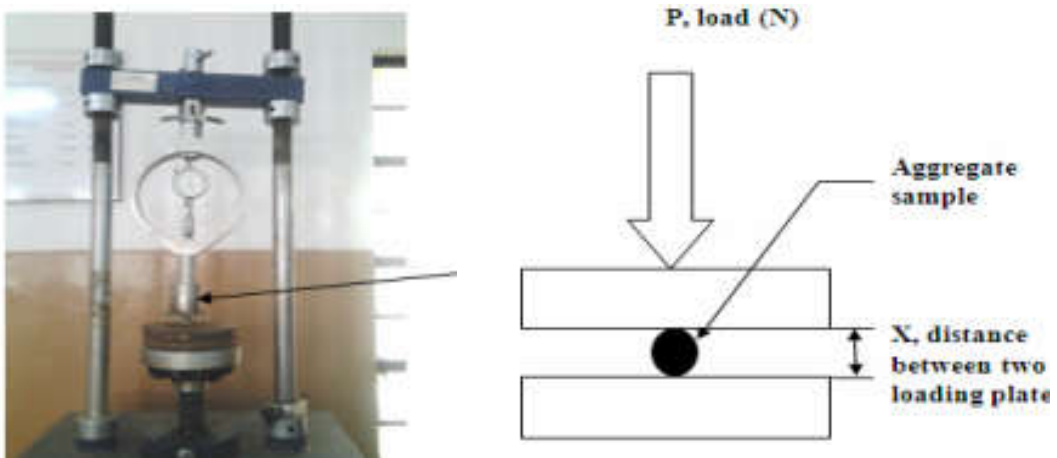

Figure 3. *Crushing test machine*

3. Result and discussions

3.1. Efficiency of pelletization

Efficiency of aggregate production depends on the amount of raw fly ash converted to fly ash balls during agglomeration of moist fly ash particles in a pelletization process.

The test results on the specific gravity, density and water absorption of different fly ash aggregates in the study are given in Table 3. It is noted that the specific gravity of NC3 was observed to be higher (2.10) than other types of aggregates. The lowest specific gravity (1.67) was observed for fly ash aggregates without binder (F1). Furthermore, the test results on the water absorption of fly ash aggregate without alkali (C3) showed the least value (14%) and were higher (38%) for fly ash aggregate with alkaki (F1).

Table 3. Physical properties of various fly ash aggregates produced (ASTM C127-73)

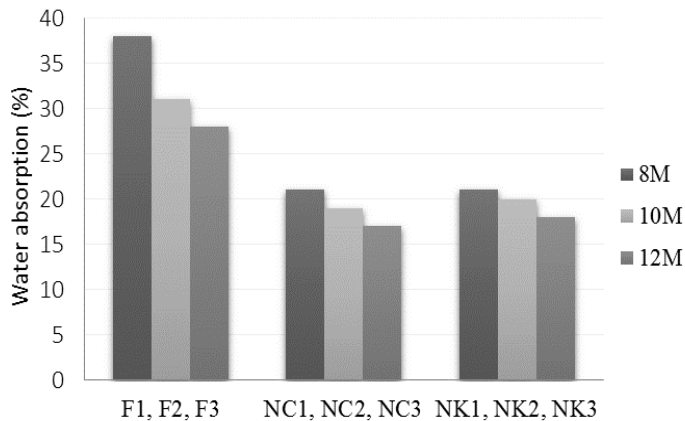| Aggregate mix	Specific gravity	Loose bulk density (Kg/m³)	24h Water absorption (%)
F1	1.67	705.35	38
F2	1.85	821.84	31
F3	1.94	867.71	28
NC1	1.97	795.36	21
NC2	2.06	890.68	19
NC3	2.10	910.65	17
NK1	1.87	949.68	21
NK2	1.85	907.65	20
NK3	1.82	860.11	18
C1	1.75	730.35	36
C2	1.78	715.44	32
C3	1.82	832.75	14

Figure 4. Water absorption of various types of fly ash aggregate containing binder

3.2. Strength properties of fly ash aggregate

The test results on the crushing strength of individual fly ash aggregate are given in Table 4. It was also observed from the results that the strength of fly ash aggregate increased with higher alkali concentration. The highest crushing strength of 13.42MPa was recorded for fly ash - Metakaolin (NK3) at 28 days curing (100^0C hot air oven curing) compared to other aggregate (Table 4).

Table 4. *Individual crushing strength of various types of fly ash aggregates at 7 days and 28 days curing*

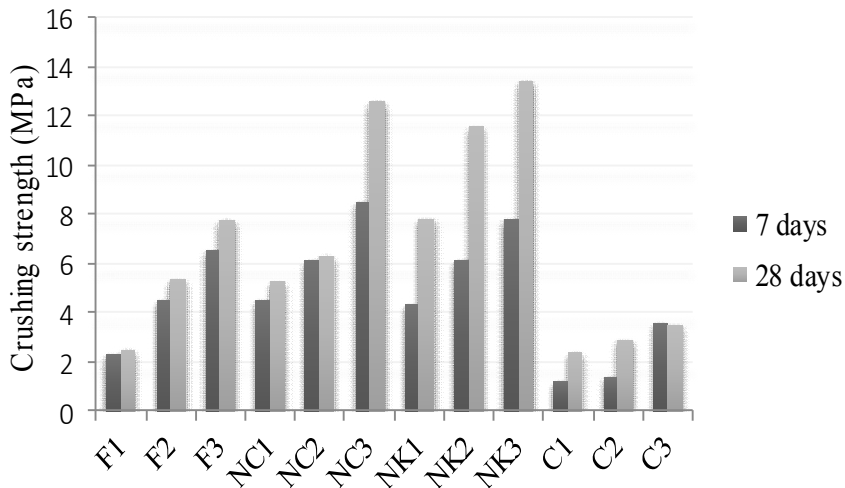| Aggregate mix	Maximum crushing strength (MPa)	
	7 day	28 day
F1	2.31	2.44
F2	4.53	5.32
F3	6.57	7.76
NC1	4.47	5.23
NC2	6.10	6.25
NC3	8.50	12.56
NK1	4.32	7.85
NK2	6.15	11.56
NK3	7.81	13.42
C1	1.20	2.40
C2	1.37	2.87
C3	3.56	3.50

Figure 5. *Crushing strength of various types of fly ash aggregate containing binder*

4. Conclusions

The following conclusions are made from the experimental study on the different types of fly ash aggregate:

a) Compared to Nghi Son fly ash aggregates with cement binder, the ternary blends of fly ash - cement - Metakaolin exhibited higher production efficiency as well as higher strength.

b) The addition of NaOH in fly ash aggregates provided higher strength at shorter curing time with reduced water absorption.

c) The crushing strength of Nghi Son fly ash aggregates (NK3) at 12M of NaOH recorded a maximum strength of 13.42 MPa at 28 days oven curing with water absorption of 18%.

d) It can be concluded that for all fly ash aggregates with binder, the addition of NaOH at higher concentration (12M) exhibited higher strength gain due to geopolymerisation reaction and the rate of hardening was effective when the specimens were cured at higher temperature (hot air oven at 100^0C).

References

[1] Ahmaruzzaman M. (2010), *A review on the utilization of fly ash*. Progress in Energy and Combustion science. (36): 327-363.

[2] Baykal G. and Doven A.G. (2000), *Utilization of Fly Ash by Pelletization Process Theory Application Areas and Research results*. Resources, Conservation and Recycling. 30, 59-77.

[3] Bijen J.M.JM. (1986), *Manufacturing processes of artificial lightweight aggregates from fly ash*. International Journal of Cement Composites and Lightweight concrete. 8(3): 191-199.

[4] Manikandan R. and Ramamurthy K. (2007), *Influence of fineness of fly ash on the aggregate pelletization process*. Cement and Concrete Composites. 29: 456-464.

[5] Ramamurthy K. and Harikrishnan K.I. (2006), *Influence of binders on properties of sintered fly ash aggregate*. Cement and Concrete Composites. 28: 33-38.

[6] Glory J. and Ramamurthy K. (2009), *Influence of fly ash on strength and sorption characteristics of coldbonded fly ash aggregate concrete*. Construction and Building Materials. 23: 1862-1870.

[7] Tommy Y. Lo., Cui H.Z., Tang W.C. and Leung W.M. (2008), *The effect of aggregate absorption of pore area at interfacial zone of lightweight concrete*. Construction and Building Materials. 22: 623-628.

[8] Harikrishnan K.I. and Ramamurthy K. (2006), *Influence of Pelletization Process on the Properties of Fly Ash Aggregates*. Waste Management. 26: 846-852.

[9] Wasserman R. and Bentur A. (1997), *Effect of Lightweight fly ash aggregate microstructure on the strength of concretes*. Cement and Concrete Research. 27(4): 525-537.

[10]   Manikandan R. and Ramamurthy K.(2008), *Effect of curing method on characteristics of cold bonded fly ash aggregates*. Cement and Concrete Composite. 30: 848-853.

[11]   Swamy R.N. and Lambert G.H. (1981), *The microstructure of lytag aggregate*. International Journal of Cement Composite and Lightweight Concrete. 3(4): 273-282.

[12]   Tommy Y. Lo., Tang W.C and Cui H.Z. (2007), *The effects of aggregate properties on lightweight concrete*. Building and Environment. 42: 3025-3029.

[13]   Yongdan L., Dongfang W., Jianpo Zhang L.C., Dihua W., Zhiping F. and Yahua S. (2000), *Measurement and statistics of single pellet mechanical strength of differently shaped catalysts*. Powder Technology. 113: 176-184.

ASSESSING THE GROUNDWATER SALINITY IN HAU LOC DISTRICT, THANH HOA PROVINCE FOR PROPER MITIGATION MEASURES

Le Thi Thuong, Nguyen Thi Mui

Abstract: *Water is a vital resource for the survival and development of humanity. However, this resource is not endless. Today, water demand for domestic use and production is increasing in the context of climate change, natural disasters and pollution, significantly causing the depletion of water resources both in terms of quantity and quality. This research has analyzed, evaluated ground water salinity in Hau Loc district, Thanh Hoa province by determining the concentration Chloride-Silver nitrate titration with Chromate indicator (MO Method) and establishing a zoning map of salinity. The results showed the groundwater at researched areas was being saline over the allowable standards many times. The highest salinity concentration of Cl⁻ exceeded 15 times the allowable standards. This study consequently proposed some solutions for efficient using of water and reducing the groundwater salinity level in the region.*

1. Introduction

1.1. Geographical location

Hau Loc district is a coastal plain located in the northeast of Thanh Hoa province, 25kmaway from Thanh Hoa city. Located in the coordinates from 19° North latitude, 105° East longitude.

It is bordered with Ha Trung and Nga Son district by the North respectively.

It is bordered with Hoang Hoa district by the West and South through Son Trang mountain.

East-side is adjacent to the sea.

With a total area of natural land is 141.5 km, Hau Loc is divided into 27 administrative units including 1 town (Hau Loc), 26 communes: Dong Loc, Dai Loc, Trieu Loc, Chau Loc, Tien Loc, Loc Son, Cau Loc, Thanh Loc, Tuy Loc, Phong Loc, My Loc, Van Loc, Thuan Loc,

Le Thi Thuong
Faculty of Engineering and Technology, Hong Duc University
Email: Lethithuong@hdu.edu.vn (✉)

Nguyen Thi Mui
Faculty of Engineering and Technology, Hong Duc University
Email: Nguyenthimui@hdu.edu.vn (✉)

Loc Tan, Xuan Loc, Thinh Loc, Hoa Loc, Lien Loc, Quang Loc, Phu Loc, Hoa Loc, Minh Loc, Hung Loc, Hai Loc, Da Loc, Ngu Loc.

Figure 1. *Administrative map at Hau Loc district*

1.2. Groundwater characteristics

According to data from Thanh Hoa Centre for Hydro-Meteorological Forecasting in February 1998, the coastal land in Hau Loc includes two 2 layers of groundwater. Upper layer (superficial) with a depth of 10 - 15 meters contains relatively abundant water; well-water flow rate reaches 0.7 - 1.7 l/s; and the mineralization below 1g/ l. At the deeper layers (deep vessels) with weak pressure, well-water flow rate reaches 15-17 l/s (Figure 2) [3].

Groundwater salinity occurred in the region, causing water salinity at many wells to exceed permissible standards for drinking [3]. This water source is mainly used for daily activities of residents, therefore, it is crucial to assess the quality of the groundwater in this area.
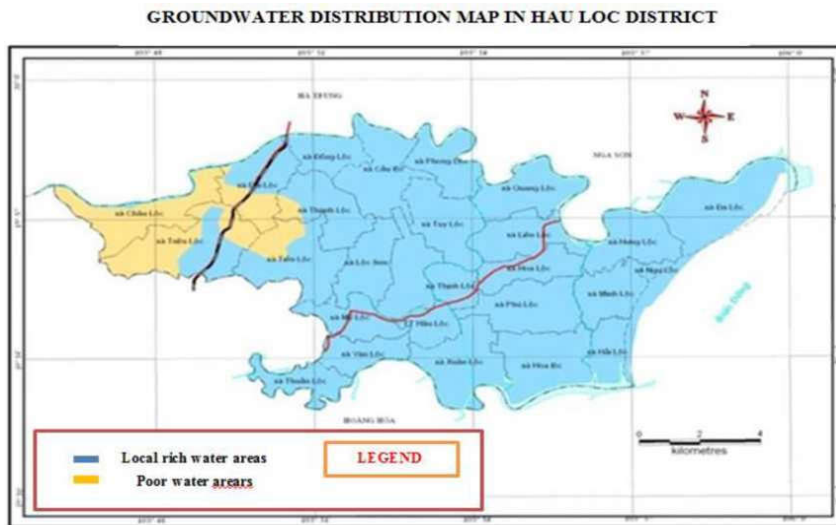

Figure 2. *Groundwater Distribution in Hau Loc district [3]*

2. Methodology

a) Inheritance method

Collect, review documents and inherit the scientific research results, especially the results of the current state of economic, social, environmental and groundwater at Hau Loc district.

b) Analysis, synthesis and data processing methods

The collected data of natural conditions, economic - social condition and environment will be selected, analyzed, synthesized and processed in line with the research objectives.

c) Groundwater sampling method

General regulations:

Groundwater sampling method is based on the following regulations:

TCVN 6663-1:2011 (ISO 5667-1:2006) - Water quality- Part 1: Guidance on the sampling program and sampling techniques.

VN standard 6663-3:2008 (ISO 5667-3:2003) - Water quality - Sampling. Guide to storage and handling of samples.

VN standard 6663:2011 (ISO 5667-11:2009) - Water quality - Sampling. Part 11: Guidance on sampling of groundwater.

Water sample analysis was carried out in 3 days from 7/5 to 9/5/2012 at the laboratory of Department of Environmental Engineering Environmental Sciences University of Natural Sciences, National University of Hanoi.

Sampling Method: Sampling by pump and sampling in depth

Analysis Method: According to ISO 6194-1996, Water quality - Determination of chloride - Silver nitrate titration with chromate indicator (Mohr's method)

Method of evaluating results: Based on VN National Standard 09:2008/ MONRE on National technical regulation on underground water quality, which stipulates the chloride limit value is 250 mg/l (Cl$^-$ standard is not changed compared to VN National Standard 09: 2015/ MONRE).

Method of mapping by interpolation: Based on chlorine concentration results in the area and Arc GIS software for establishing the zoning map of salinity

3. Results and discussion

3.1. Results

The analytical results of chloride concentrations in water samples are presented in Table 1.

Table 1. The concentration of Cl$^-$ in the groundwater

No	Sampling locations		Wells	Depth (m)	Concentration of Cl$^-$ (mg/l)
	Latitude	Longitude			
1	19.9117	105.86208	Drilling machine	40	158.12
2	19.908336	105.87723	Drilling machine	30	1074.935

3	19.906951	105.88565	Manual drill	8	1639.347
4	19.915657	105.89049	Drilling machine	32	1134.496
5	19.919812	105.89512	Drilling machine	30	1758.469
6	19.929705	105.89028	Drilling machine	28	783.52
7	19.926737	105.8505	Manual drill	7	38.998
8	19.939598	105.84124	Manual drill	6	146.066
9	19.921988	105.88607	Drilling machine	45	53.18
10	19.920405	105.87555	Deep-well	10	198.537
11	19.938213	105.88144	Drilling machine	20	316.95
12	19.940983	105.87113	Manual drill	8	301.351
13	19.92555	105.86545	Manual drill	9	768.621
14	19.902598	105.89618	Manual drill	6	737.422
15	19.916844	105.90501	Manual drill	7	1352.886
16	19.889342	105.90102	Manual drill	5	2188.632
17	19.930298	10.91385	Manual drill	7	54.598
18	19.932673	105.92817	Drilling machine	20	248.171
19	19.922384	105.92396	Manual drill	8	150.321
20	19.912689	105.9248	Drilling machine	18	42.544
21	19.904775	105.92522	Drilling machine	15	195.701
22	19.904775	105.92375	Manual drill	10	3935.283
23	19.947908	105.95784	Drilling machine	30	524.704
24	19.935443	105.94711	Drilling machine	25	124.086
25	19.942566	105.97152	Manual drill	7	51.052
26	19.95879	105.98604	Manual drill	8	36.871
27	19.927528	105.93995	Drilling machine	7	131.176
28	19.91724	105.95153	Manual drill	5	211.3
29	19.91724	105.93785	Drilling machine	12	160.957
30	19.93109	105.96352	Manual drill	6.5	250.302
31	19.926143	105.95826	Manual drill	5	243.208
32	19.893892	105.94627	Drilling machine	70	1396.848
33	19.908732	105.94753	Drilling machine	68	1045.812
34	19.942763	105.92396	Drilling machine	15	561.576
35	19.944148	105.90796	Drilling machine	20	155.993
36	19.945533	105.89302	Drilling machine	43	972.638
37	19.956416	105.91722	Drilling machine	50	791.569
38	19.891914	105.85156	Drilling machine	25	439.617
39	19.890529	105.83914	Drilling machine	38	150.321
40	19.902994	105.86019	Drilling machine	25	269.443
41	19.897454	105.86797	Drilling machine	20	1437.974
42	19.902994	105.89554	Drilling machine	45	379.612

The chloride concentration in the region generally fluctuates in a wide range. There are many high values of chloride concentration. Based on location of sampling sites and the chloride concentration it shows the dependence of salinity level on the sampling locations adjacent to the coastline and salinity river shoreline.

Many places located close to each other in the same area, but the Cl⁻ concentration showed a large difference. For example, the sample 1 taken in Tran Phu, My Loc showed the Cl- concentration of 158.120 mg/l, while the sample 2 is taken in Dai Huu, My Loc showed Cl- concentration of up to 1074.935 mg/ l.

Some water samples were taken in shallow layer, from 7m to 9m, especially in coastal areas such as the Ngu Loc, Xuan Loc, Minh Loc, Da Loc, etc. Because of the characteristic of sandy soil, water was found even in a very shallow layer. However, at this depth, the groundwater was influenced by a lot of surface water causing seasonal and unstable salinity variation.

According to Vietnam National Standard 09:2008/MONRE, the allowable concentration of Cl⁻ is 250mg/l. The analytical results showed a lot of water samples beyond the standard. For example: the sample 16 (Huu Nghia, Xuan Loc) is 2188.632 mg/l (more than 8.7 times the regulations) and the sample 32 (Truong Nam, Hai Loc) is 1396.848 mg/l (more than 5.5 times the regulations), the sample 41 (My Dien, Van Loc) is 1437.974 mg/l (6 times regulation), the sample 22 (Hoa Ngu, Hoa Loc) showed the largest concentration of chloride of 3935.283 mg/l (more than 15 times the regulations).

The analytical results of the concentration Cl⁻ were mapped on the Figure 3 below:
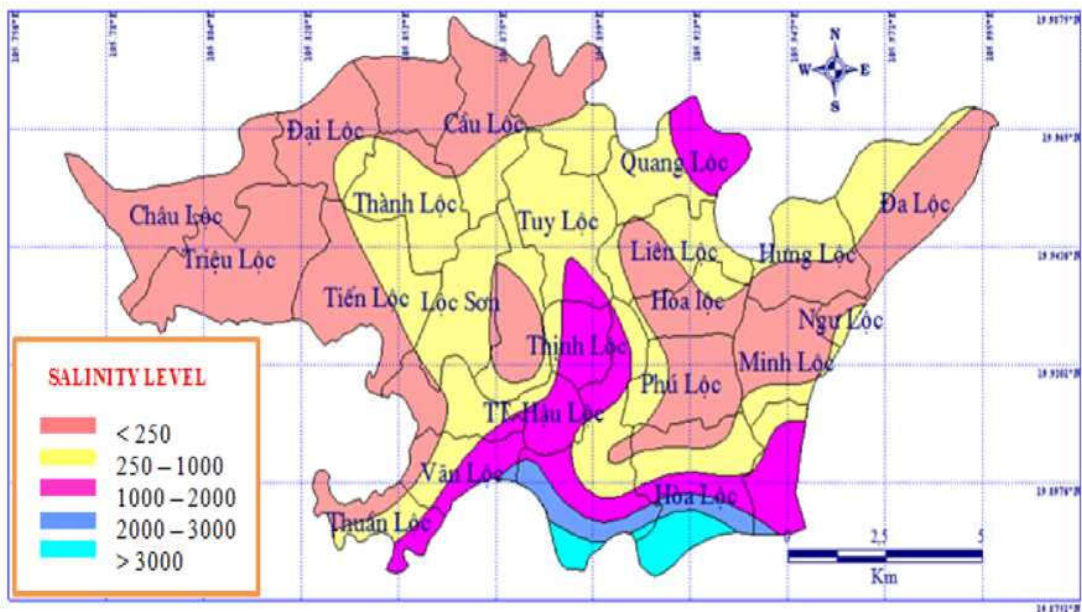

Figure 3. *Groundwater Salinity Partition in Hau Loc district*

3.2. Assessing groundwater situation in Hau Loc district

3.2.1. Causes of groundwater salinity

Due to the seawater intrusion when the hydraulic pressure of the ground water is below sea level. This phenomenon occurs when there is a change in equilibrium conditions of natural groundwater or overexploitation of this water source caused lower groundwater level, leading to the displacement of saline toward land. Specifically, Hau Loc district with 12 km of sea dikes along the diverse hydrological system including four rivers: Len river, Kenh De, Lach Truong, Tra Giang and two large estuaries Lach Sung, Lach Truong, which has a big impact on the groundwater. In the dry season the rivers often have low flow water level, usually lower than sea level. The tide therefore can cause salt water intrusion into the river and saline groundwater at many areas, for example at the coastal communes: Ngu Loc, Hoa Loc and estuaries: Xuan Loc, My Dien - Van Loc, with very high level of salinity. However, salinity at Da Loc - a commune located in the coastal region was under 250mg/l, which is explained by the circulation and abundant flow of the Len river restricting the saltwater intrusion from the sea.

Discrete stratum structure is also a cause of groundwater salinization. In coastal areas, the discrete structure makes evaporation phenomenon occur strongly and saltwater easily penetrate into the soil, rivers, groundwater.

The production activities of people are also a cause of increased water salinity. For example, salt production or the sea water using for aquaculture (shrimp farms) at Hai Loc and Hoa Loc.

3.2.2. The ability of the water supply and salinity tendency at Hau Loc district

The increasing groundwater exploitation for living and production activities would decline groundwater reserves.

Groundwater reserves in Hau Loc district was abundant in the past [1]. However, because of growing population and economic development, the demand for water (surface and groundwater) is gradually increasing, leading to groundwater shortage recently. This increases the potential for saltwater intrusion into the groundwater.

Impact of climate change and sea level rise on the groundwater source.

Under the influence of climate change, sea level rise and increasing temperature in the region. The change of these factors have reduced the additional surface water into groundwater especially in the dry season leading to an increase in the penetration of saltwater into groundwater both in terms of scale and concentration.

For the wells in the coastal region, water quality will be affected by saltwater intrusion, causing salinity to increase and decrease of groundwater reserves.

4. Mitigation measures for groundwater salinity

4.1. Saving water

In the area where water is used mostly in agriculture, it should be focused on securing water resources for crops in conditions of climate change by specific measures:

Complete irrigation systems to reduce water losses and leaks by concrete solutions and solidifying canals. These measures are priorities in the strategic management and use of water for agricultural production, in order to reduce the pressure of local groundwater resources.

Look at the scientific irrigation technology applied to save water while improving crop yields: drip irrigation on crop farming area in the water scarcity, or saline areas, etc. in order to save irrigation water and adapt to harsh climate change.

Dig ponds to store water during the rainy season in order to irrigate crop areas at the high hills. Develop and apply agriculture combine aquaculture models: dig a pond to store water, use waterproof materials, combine fishing with farming.

4.2. Construction of the station, centralized water supply plant

With the increasing groundwater salinity and the demand for sanitary water, it's necessary to construct water stations/plants for residential and other welfare needs; especially under the impact of climate change today. The specific directions are as follows:

Construction of water stations/plants to provide water for expected focus areas/industrial complex and large population centers from the Ma river surface water source. For example, the clean water plant construction at Chau Loc commune to provide clean water for the Chau Loc industrial parks and towns from Van Loc to Thinh Loc.

Construction of water mining station to exploit clean water with no salinity to provide for coastal areas such as Da Loc, Ngu Loc, Xuan Loc...

4.3. Protection and management of water resources

The management of groundwater resources now requires the participation of all levels in a systematic manner.

Problem of management, protection of natural resources is now being concerned by the Government. Therefore, management and protection of water resources must comply with the document No.22-LCT/HDNN dated August 7, 1989 on natural resources, minerals and other by laws.

Continue to implement the projects of planning, exploitation, using and protecting underground water resources. Besides, define restricted areas, the limited groundwater extraction and cataloging, the partition map.

Promotes helping people deal with the saltwater intrusion, be active in production and life activities consistent with the characteristics of each ecological region. Research, provide salinity water treatment methods for people or promote the planning and construction of clean water plants to provide drinking water for the population in areas severely affected by salinity.

5. Conclusion

Results of water sample analysis and the partition mapping of groundwater salinity level at Hau Loc district has shown the current status and forecast salinity tendency of each

area in the district. Salinity level at many areas in the district still meets allowable standards, such as at Tan Loc and Loc Son, Tien Loc, Hoa Loc, Phu Loc, etc. However, 50% water-well samples have high level of salinity, which exceeded 15 times the standards. The highest salinity is determined in the coastal communities and the estuary areas such as Ngu Loc, Hai Loc, Hoa Loc, Xuan Loc and Phu Loc, Van Loc, Tuy Loc, Quang Loc. The salinity is caused by seawater intrusion into the aquifer.

Salt water intrusion is an important issue and has a great influence on the production and daily activities of local people at Hau Loc district. The groundwater salinity situation is increasing both in terms of scale and concentration and need to be addressed to ensure sustainable development of Hau Loc district.

References

[1]   Nguyen Van Dan, Vo Cong Nghiep, Dang Huu On (1996), *The groundwater of the North Central Coast of Vietnam*, Department of Geology published and copyrighted.

[2]   Le Duc, Tran Khac Hiep, Nguyen Xuan Cu, Pham Van Khang, Nguyen Ngoc Minh City (2004), *Some methods of environmental analysis*, of Hanoi National University Publishing House.

[3]   Luu Duc Hai and his team (2007), *Research on environmental planning at district level, applications for specific districts (Thuong Xuan, Tho Xuan, Hau Loc) in Thanh Hoa Province*, Report synthetic VNUlevel key themes - QGTD.06- 10.

[4]   Hau Loc District People's Committee, *The Economic and Social report 2006, 2007, 2008, 2009, 2010, 2011.*

IOT APPLICATION IN CONTROL SYSTEM USING WIRELESS SENSOR FUSION

Pham Van Trung

Abstract: *A wireless controller based on data fusion algorithm and IoT technology is designed and applied for an active QZS isolator. Firstly, an IoT sensor modular using wireless instead of wired connection is proposed. The wireless sensors of acceleration, velocity and distance are used in the active QZS isolator in order to eliminate unpredictable disturbance causing by wire of sensors. Secondly, the data fusion algorithm embedded in wireless sensor module is described to show how to combine acceleration, velocity and distance data into one kind of information. The fuser with advanced fusion technique will protect control system from a suddenly disabled sensor. Lastly, the system controller uses data fusion to compute control signal for producing a governing force of the isolator. The experiment result shows out 60% better eliminating vibration of the proposed controller.*

1. Introduction

Today, smart grid, smart homes, smart water networks, intelligent transportation are infrastructure systems that connect our world more than we ever thought possible. The common vision of such systems is usually associated with single concept, the internet of things (IoT), where through the use of sensors, the entire physical infrastructure is closely coupled with information and communication technologies; where intelligent monitoring and management can be achieved via the usage of networked embedded devices.

A wireless sensor network (WSN) is a network formed by a large number of sensor nodes where each node is equipped with a sensor to detect physical phenomena such as light, heat, pressure, speed, etc. The sensors collecting data which are combined in one kind of information is called sensor fusion. The control systems using wireless sensors fusion have been found many benefits of not only reducing the monetary and time expenses associated with the installation of wire-based systems but also guarantee for some missing sensors. The use of wireless communications within a structural health monitoring data acquisition system was illustrated by Straser and Kiremidjian [1]. In addition, multi-sensor data fusion is the process of combining observations from a number of different sensors to provide a robust and

Pham Van Trung

Faculty of Engineering and Technology, Hong Duc University

Email: Phamtrung85@gmail.com (✉)

complete description of an environment or system states which is used in many areas of robotics such as such as object recognition, environment mapping, and localization [2].

In this paper, a wireless sensor fusion module is designed and applied for an active QZS isolator for some purposes: Firstly, using wireless sensor in the active QZS isolator is to eliminate unpredictable disturbance causing by connecting wires of the wired sensors for the isolator system with almost zero stiffness is easily effected by sensitive noise [3]. Secondly, the data fusion technique embedded in wireless sensor module is to protect control system from a suddenly disabled sensor while the system is running. Lastly, the system controller uses data fusion to compute control rule for producing a governing force of the isolator.

2. Wireless sensor fusion module

2.1. Hardware configuration of wireless sensor module

The wireless sensor model includes two parts: Sensing and control interfaces as shown in Figure 1. The sensing interface is the Texas Instruments ADS834 AD converter which offers a 16-bit conversion resolution and 4 sensing channels which is capable of digitizing any analog signal in the 0- 5 V range at sample rates as high as 100 kHz. The control interface is designed with a 16-bit digital - to - analog converter (Analog Devices AD5542) which receives binary number from the microcontroller and converts them to analog voltage signals. Both use the Atmel ATmega128 microcontroller for computational core where embedded software is stored to execute data acquisition and transition. Two WiFi/DSL routers, ENC28J60 Ethernet controllers are selected for wireless communication channel in both interfaces.
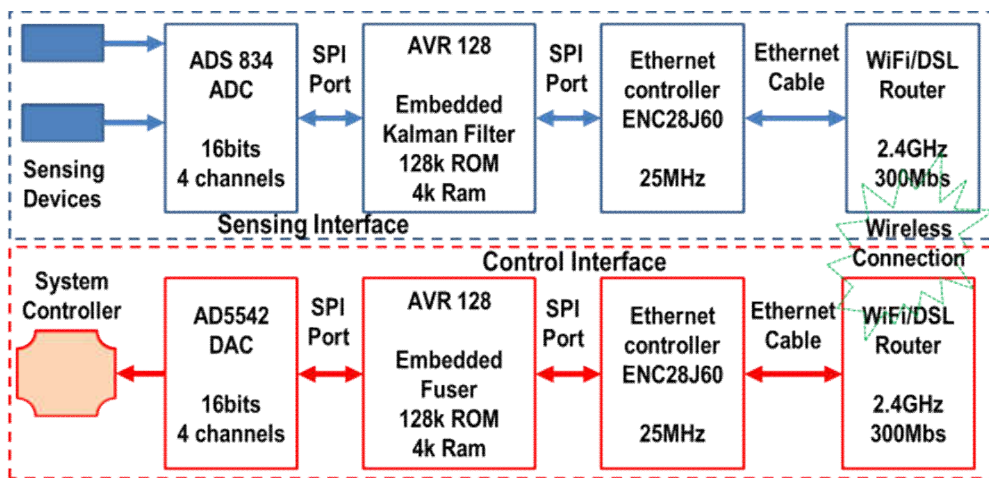

Figure 1. *Architecture of a wireless sensor interfaces*

2.2. Multi-sensor fusion based on Kalman filter

In discrete-time controlled process, a Kalman filter is governed by the linear stochastic difference equations (1) and (2) which is described by an ongoing cycle as shown in Figure 2:

$$x_k = Ax_{k-1} + Bu_{k-1} + w_{k-1} \qquad (1)$$

$$z_k = Cx_k + v_k \qquad (2)$$

where A, B, and C are coefficient matrices; k is the time index; x is system states; u is control signal; z is measured states; w and v represent the process and measurement noise.

Figure 2. *Continuous cycle of Kalman filter*

A fusion technique is studied and embedded into the control interfaces of the wireless sensor module. In detail, displacement and velocity measurement signals are used for estimating acceleration, velocity and displacement signals based on Kalman filter algorithm. The outputs of the Kalman filters are data sources for a data fuser which will compute fused data providing for a system controller. The schematic model of sensor fusion is shown in the Figure 3 and the fusion algorithm is sketched in the Figure 4.
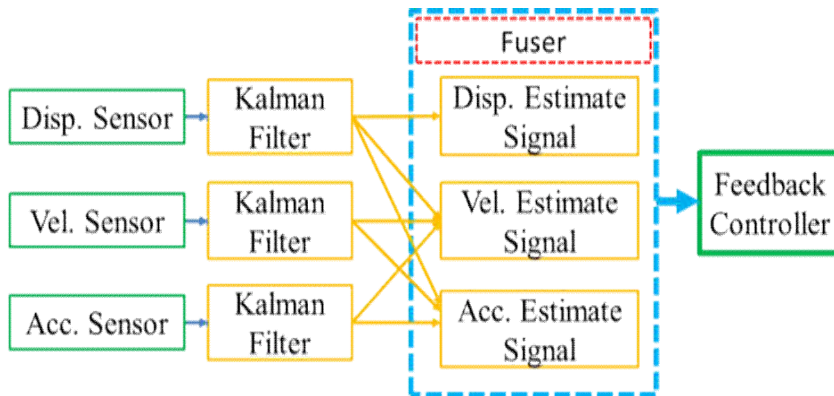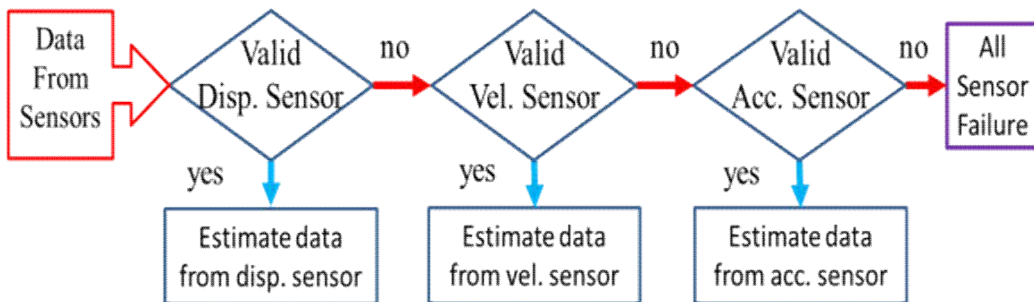

Figure 3. *Sensor fusion model*

Figure 4. *Algorithm of data fusion*

3. Active control model of QZS isolator

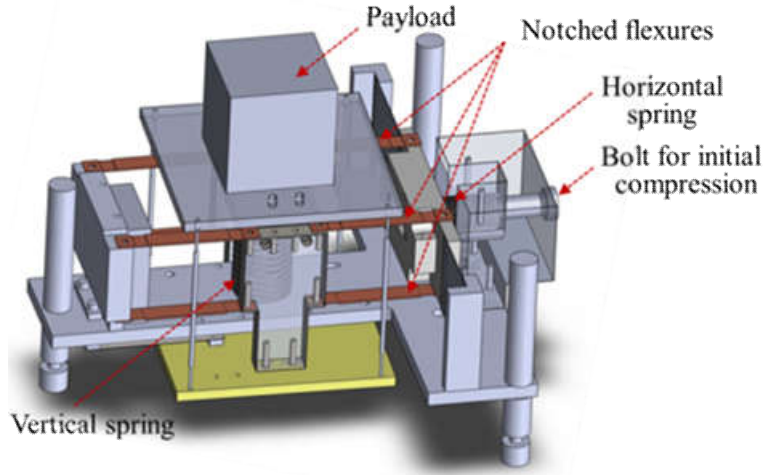### 3.1. The QZS isolator using flexure

Figure 5. *QZS isolator using flexure [3]*

A mechanism of QZS isolator using flexure studied in this research is shown in the Fig. 5. The mechanism consists of three main parts: the horizontal coil spring, vertical coil spring and notched flexures. While the vertical coil spring produces positive stiffness, the notched flexure under compressive force of initially deformed horizontal spring generates a negative stiffness which allows obtaining quasi-zero stiffness (QZS) characteristics.

3.2. The motion equation of the isolator model

Based on the dynamic analysis of this isolator model that is presented in the reference [3], the motion equation of dynamic model is derived as Eq. (3):

$$m\ddot{y} + c\dot{y} + k_l y + k_n y^3 = f_c A_2 y + w(t) \tag{3}$$

where y is vertical displacement; m is mass; c is system damping; k_l and k_n are linear and nonlinear stiffness respectively; f_c is control force.

3.3. Active control rule

In studying the case of the horizontal actuation, the actuator force is derived based on the dynamic equation (3). The control law is derived and converted to the horizontal actuator force as shown in Eq. (4).

$$f_{nl} = a_1 \frac{y}{\max(y, y_0)} + a_2 \frac{\dot{y}}{\max(y, y_0)} - a_3 \frac{y^3}{\max(y, y_0)} \tag{4}$$

where a_1, a_2, a_3 are Lyapunov control tuning gains. The a_3 is gained for nonlinear feedback to cancel out the system nonlinear characteristic. The actuator force near equilibrium point ($y=0$) is considered to avoid saturation.

141

4. Experiment configuration setup

The experiment configuration consists of passive QZS isolator, digital controller, sensors, actuator, and wireless sensor interface module as shown in Figure 6. Vertical passive isolator specification is summarized in the Table 1.

Table 1. *Isolator specifications*

Parameter	Value	Parameter	Value
m	25 - 40(Kg)	Stroke	±0.005(m)
k_{hs}	3.626×10^5(N/m)	k_{vs}	1.02×10^4(N/m)
c	2.87(Ns/m)	f_n	1 (Hz)

Several analog sensors are used for sensing system state data such as velocity sensor, acceleration sensor, and displacement sensor. The dSPACE controller computes and generates control signal from data provided by wireless sensor module. The control signal regulates the actuator through amplifier to stop vibration of the mass.
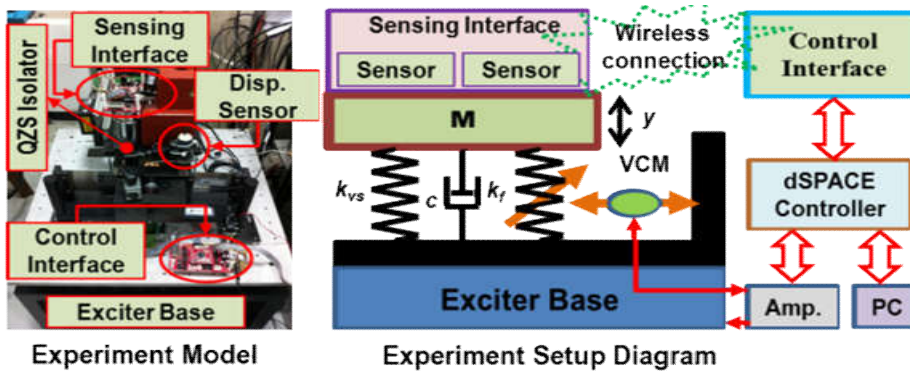

Figure 6. *Experimental setup*

5. Experiment result

The experiment of the active QSZ isolator using wireless sensor fusion module is implemented to investigate the performance of wireless sensor fusion module and control response. The wireless fusion signal is verified by wired sensor signal and examined under suddenly disabled sensors as shown in Figure 7 and Figure 8. Control performance is obtained with two vibration isolation testing standards: impulse disturbance rejection and vibration transmissibility. The result of impulse disturbance rejection is shown in Figure 9 and the result of the vibration transmissibility is shown in Figure 10. Both results show that the active QSZ isolator using wireless sensor fusion data has a good performance of vibration isolation. In the time domain, settling time is reduced 75 percent by active control system comparing to the passive isolator. In the frequency domain, the resonance magnitude is degraded about 60 percent.
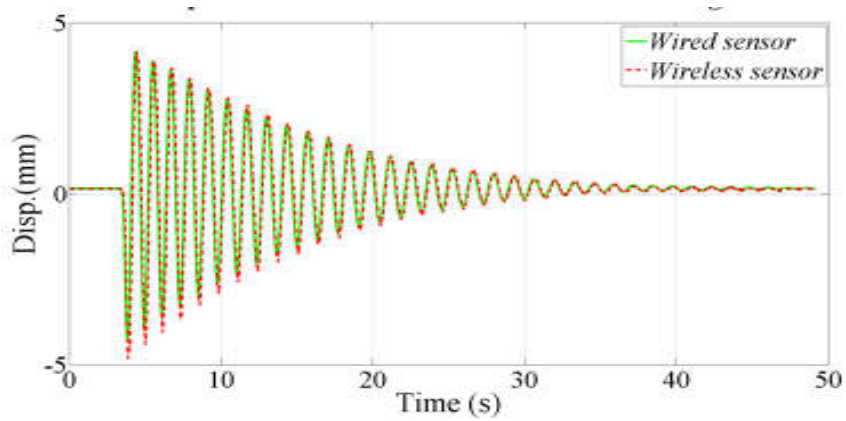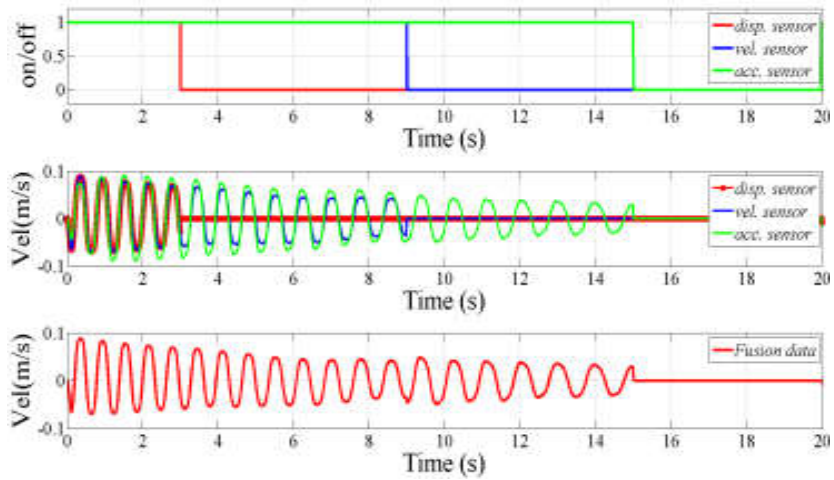
Figure 7. Signals verification

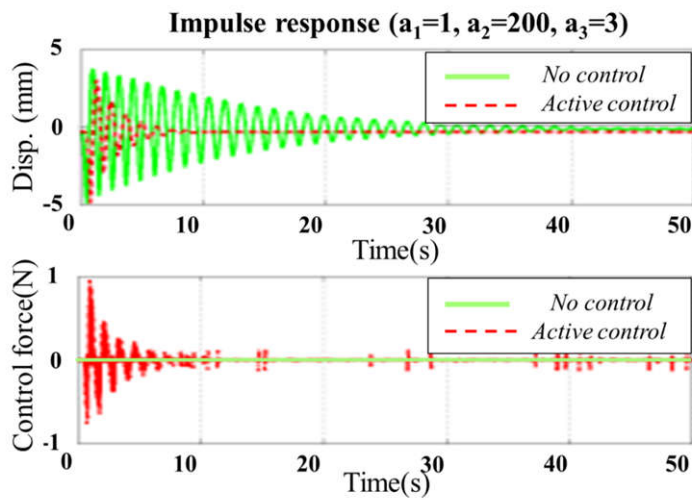*Figure 8.* Fusion signals under missing sensors

Figure 9. Disturbance rejection [3]

Frequency response(a$_1$=1, a$_2$=200, a$_3$=3)

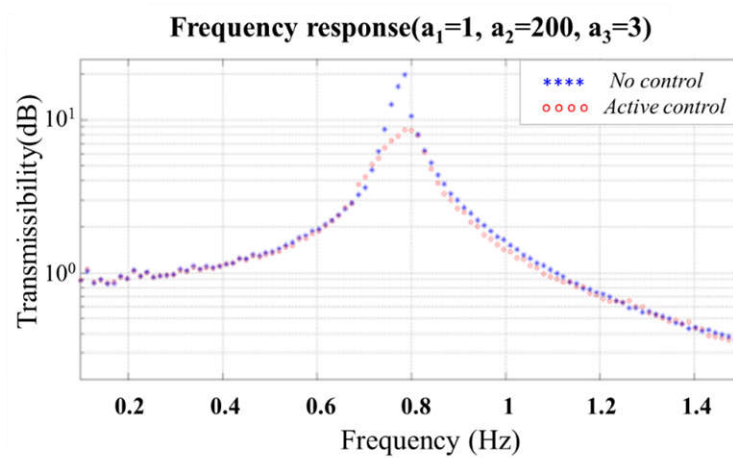***Figure 10.*** *Transmissibility [3]*

6. Conclusion

The active QZS isolator based on sensor fusion using IoT technology is proposed and investigated through the experiment. The proposed wireless sensor fusion module works well with data acquisition and system monitoring. The experiment results of active system responses show a good performance to vibration isolation in both time domain and frequency domain of the active QZS isolator by using fused data.

References

[1]   E. G. Straser, A. S. Kiremidjian (1998), *A modular, wireless damage monitoring system for structures*, ReportNo.129, JohnA.Blume Earthquake Engineering Research Center, Department of Civil & Environmental Engineering, Stanford University, CA 1998.

[2]   M. Kam, X. Zhu, P. Kalata (1997), *Sensor fusion for mobile robot navigation*, IEEE Journals & Magazines, Vol. 85, pp. 108-119, Japan.

[3]   P. V. Trung, K. R. Kim, H. J. Ahn (2013), *Nonlinear control of active QZS isolator based on lyapunov function*, Korean Society for Precision Engineering and Springer-Verlag Berlin Heidelberg, Volume 14, Issue 6, pp 919 -924, June 2013.